

Computational methods for quantifying surface
structure and dynamics with Low-Energy Electron
Microscopy

Cardiff University



Matyo Ivanov

29 September 2023

Acknowledgements

This work reflects all my notable strokes of luck during my PhD - a time with a few fair shares of highs and lows. For amplifying the joyous moments and for helping me get through the tough ones, I would like to thank all the people, who were around me at the best of times and at the worst of times.

First and foremost, I would like to thank my supervisor Dr Juan Pereiro Viterbo. I immensely appreciate your guidance during my PhD, from which I have learned and developed beyond what I thought I was capable of. But even more than that, I sincerely thank you for being a great mentor, a great friend, and for giving me more support than I could have asked for throughout the years. Thank you for bearing with me!

I would like to thank Prof David Jesson, who guided me in my baby steps in research prior to embarking on my PhD and demonstrated great faith in my abilities to welcome me into his group.

A big thank you to my second supervisor, Dr Nicolas Abadia Calvo, for the fruitful discussions to help wrap up my research.

A big thank you everyone who has been part of my group throughout my PhD - Debobrata, Kennet, Yuran and Dani. A special thank you, Yuran, for the numerous helping hands with the microscope, even after parting with the group. And a special thank you to Dani, with whom I spent countless hours in the lab, who guided me with uncanny patience, and remained my close friend, always ready for a beer with me long after parting with the group.

I would also like to thank Hugh, our group's lab technician, for being such an inspiration in your energy, attitude and passion in the lab. Thank you for the unceasing responsiveness, no matter the circumstances.

To all my friends, both in Cardiff, and away, thank you for all the good memories

and for the strength in our friendships, which only grew throughout this time. It would take another thesis to do justice to how much I appreciate every one of you! Cheers to the good moments made better and the bad moments made bearable.

And, finally, to my family, and especially my parents and my sister, whom I love immensely and who have been the constant source of support and motivation throughout the years. Hopefully, with this, I give you something to brag about at home!

None of this work would have been possible, and more importantly, none of this work would have been worth it, if it wasn't for everyone around me throughout it!

Thank you all!

Благодаря!

Summary

This thesis focuses on the development of computational approaches to quantify the observations of semiconductor surfaces with Low-Energy Electron Microscopy (LEEM). The real-time surface imaging with LEEM gives us dynamical observations with a suitable temporal and spacial resolution that is difficult to achieve with other microscopy techniques. It allows us to track surface structural dynamics on a nanoscopic scale and characterise them using Computer Vision methods.

We monitor the surface of GaAs (001), where we observe a stable coexistence between the (6×6) and $c(8 \times 2)$ surface phases, as well as a metastable coexistence of those phases during growth. Using the LEEM imaging of the surface dynamics, we are then able to extract previously inaccessible parameters for the two phases. Through Computer Vision methods and computational algorithms, we develop data pipelines that enable the required accuracy and throughput in the analysis of our imaging data. With that, we extract fundamental surface parameters, such as the entropy and stress difference, as well as the step edge energy between the (6×6) and $c(8 \times 2)$ phases. We use these insights to clarify the long-standing stability question of the (6×6) phase and to explain the observed behaviour of the two phases.

Furthermore, we use Machine Learning and Deep Learning techniques to develop an approach that streamlines the analysis of the complex and abstract imaging data from the Convergent Beam Low-Energy Electron Diffraction (CBLEED) technique. We show the high accuracy and performance of the developed models in finding surface structural parameters with sub-angstrom accuracy based on CBLEED images.

Contents

1	Introduction	10
2	Background and fundamentals	14
2.1	Surface Phases	14
2.1.1	Phase Coexistence	17
2.1.2	Coexistence in Growth	23
2.2	Low-energy electron microscopy (LEEM)	26
2.2.1	Low energy electrons	27
2.2.2	The LEEM imaging system	30
2.2.3	LEEM Techniques	32
2.2.4	Resolution Limits	34
2.2.5	Advantages of LEEM	35
2.3	Computer Vision for microscopy imaging data	36
2.3.1	The use cases of traditional Computer Vision	37
2.3.2	Machine Learning and Deep Learning	43
3	Measuring entropy difference through phase coexistence monitoring with LEEM	54
3.1	Introduction	54
3.2	The stability of the (6×6)	55
3.3	Experimental details	57
3.3.1	Experimental setup	57
3.3.2	Experimental design	57
3.4	Results	62
3.4.1	Phase Coverage	62

3.4.2	Boundary fluctuations	64
3.5	Conclusion	67
3.6	Data analysis	69
3.6.1	Previous approaches	69
3.6.2	Boundary Detection	71
3.6.3	Data transformation	77
4	Growth monitoring near a Ga droplet on GaAs (001)	81
4.1	Introduction	81
4.2	Experimental details	82
4.2.1	Experimental setup	82
4.2.2	Experimental design	82
4.3	Analysis	84
4.4	Results	86
4.5	Conclusion	91
4.6	Detection Methods	92
4.6.1	Preprocessing	92
4.6.2	Detection	92
4.6.3	Object Tracking	93
4.6.4	Filtering	94
5	Real-time interpretation of CBLEED patterns with Autoencoders	96
5.1	Introduction	96
5.2	Overview	98
5.3	Methods	100
5.3.1	Dataset	100
5.3.2	Model Training	100
5.4	Analysis	102
5.4.1	Latent space size	103
5.4.2	Latent space structure	104
5.4.3	Latent Space Parameter Extraction	106
5.4.4	Performance	107
5.5	Conclusion	107

5.6 Future Work	108
6 Conclusion	109

Acronyms

μ LEED micro-LEED. [33](#), [96](#), [97](#)

AE Autoencoder. [51](#), [52](#), [98](#), [100](#), [103](#), [104](#), [107](#), [108](#)

BCE Binary Crossentropy. [101](#)

BF Bright Field. [33](#), [35](#), [61](#), [82](#)

CBED Convergent Beam Electron Diffraction. [97](#), [100](#)

CBLEED Convergent Beam Low-Energy Electron Diffraction. [97–100](#), [102](#), [104](#),
[106–108](#), [110](#)

CLAHE Contrast Limited Adaptive Histogram Equalization. [39–41](#), [60](#), [76](#), [77](#)

CNN Convolutional Neural Network. [50–52](#), [100](#)

CV Computer Vision. [12](#), [13](#), [36](#), [37](#), [43](#), [44](#), [46](#), [47](#), [49](#), [50](#), [109](#)

DCAE Deep Convolutional Autoencoder. [101](#), [102](#), [107](#)

DF Dark Field. [33](#), [35](#), [61](#)

DFT Density Functional Theory. [15](#), [16](#)

DL Deep Learning. [12](#), [36](#), [37](#), [43–46](#), [50](#), [109](#), [110](#)

FC Fully Connected. [48](#)

FOV Field Of View. [39](#)

GaAs Gallium Arsenide. [10](#), [11](#), [14–17](#)

LEED Low-Energy Electron Diffraction. [28](#), [33](#), [59](#), [96–98](#)

LEEM Low-Energy Electron Microscopy. [11–13](#), [26](#), [27](#), [29](#), [31–42](#), [54–57](#), [59–61](#),
[65](#), [68–71](#), [73](#), [77](#), [81](#), [96](#), [99](#)

LTl Linear Translation-Invariant. [40](#), [41](#), [73](#)

MAE Mean Absolute Error. [101](#), [106](#)

MBE Molecular Beam Epitaxy. [10](#), [11](#), [36](#), [81](#), [82](#)

MEM Mirror Electron Microscopy. [32](#)

ML Machine Learning. [12](#), [13](#), [36](#), [37](#), [43–45](#), [98](#), [99](#), [106](#), [107](#), [110](#)

MSE Mean Squared Error. [101](#)

NLM Non-Local Means. [40](#), [41](#), [73](#)

NN Neural Network. [46–48](#)

PEEM Photoemission Electron Microscopy. [32](#)

ResNet Residual Neural Network. [51](#), [52](#)

SEDFLEEM Selected Energy Dark Field Low-Energy Electron Microscopy. [33](#),
[57](#)

SOTA State-Of-The-Art. [36](#)

TEM Transmission Electron Microscopy. [31](#), [97](#)

UHV Ultra-High Vacuum. [10](#), [31](#), [57](#)

Chapter 1

Introduction

The quality and precision of semiconductor fabrication with fine-tunable properties is crucial to the innovation-driven technological industry, with III-V semiconductors, in particular, attracting a lot of attention in the past decades. From that, Gallium Arsenide (GaAs)-based semiconductors have emerged as some of the most widely used in the industry, due to the material's wide and direct band gap and high electron mobility. These properties allow applications which range from high-power optical devices such as diodes, lasers, and solar cells to noise-free signal amplification devices and fast electronics. An important role of GaAs in this domain is its use as a substrate for the growth of more complex III-As materials, such as GaAlAs, InGaAs, InGaNAs, as well as nanostructures, such as quantum dots, quantum wells and nanowires. One of the most widely used techniques for the fabrication of these structures is Molecular Beam Epitaxy (MBE), which allows for the required control and purity of growth.

In MBE, the substrate is held at Ultra-High Vacuum (UHV) conditions at background pressures below 10^{-9} Torr at all times. The growth commences as materials are evaporated at high temperatures from sources to produce particle beams towards the substrate surface. The particles reach the substrate and interact to form a thin film epitaxial layer, bonded in a crystalline lattice. This growth process can be precisely controlled by adjusting the beam flux and substrate temperature and achieves significant purity in the grown material. These experimental conditions have an impact not only directly on the newly grown structures, but also on the substrate surface, which, in turn, has influence on the growth dynamics (Krzyzewski

& Jones, 2008; Ohtake et al., 2013; Ohtake et al., 2014). With that in mind, knowledge of the surface behaviour at practical growth conditions and during growth is important towards the quality and properties of newly formed structures.

Cardiff University hosts one of the most suitable instruments to allow tracking of the surface behaviour during such epitaxial growth - the LEEM-MBE system. It combines the surface sensitive and non-destructive Low-Energy Electron Microscopy (LEEM) with an MBE chamber, allowing the real time in-situ non-scanning imaging of a semiconductor surface in growth conditions and during growth. The system focuses on III-As semiconductors, as the MBE chamber is equipped with Gallium, Indium and Arsenic sources. Its use of LEEM is very suitable for monitoring crystalline surfaces, such as the GaAs surface, and capturing the MBE growth process on them. LEEM provides means of real time *in-situ* monitoring of semiconductor surfaces with high spacial and temporal resolution. The low energy electrons provide a structural sensitivity that returns detailed information on the surface reconstruction, allowing high contrast between the surface phases. With an atomic resolution perpendicular to the surface plane and a resolution down to 5 nm in the surface plane, LEEM also provides detailed information on surface morphological structures, such as atomic steps and defects, and is ultimately able to capture the small-scale surface dynamics during growth.

To build on the knowledge of the GaAs surface behaviour during growth, this thesis focuses on monitoring and analysing the high-temperature GaAs(001) surface both at growth conditions and during growth using Cardiff's LEEM-MBE system. Recent observations by Zheng et al., 2019 with the LEEM-MBE system have already provided significant insights on the surface phases on GaAs. At high temperatures in the range of 530 – 580 °C, the predominantly observed surface phases are the Ga-rich (6×6) and $c(8 \times 2)$ phases, which create high contrast in LEEM imaging and enable a detailed view on the surface dynamics.

The main topic in the thesis is the outstanding uncertainty concerning the stability of the (6×6) and its role in surface dynamics at these high temperature conditions (Ohtake, 2007), which is still not well understood despite the GaAs(001) surface phases being generally well researched (Ohtake, 2008). To shed light on these uncertainties, we monitor, describe and quantify the interactions between the

(6×6) and $c(8 \times 2)$ phases. We build on the insights on their dynamics during evaporation processes, recently observed through the LEEM-MBE system and detailed by Hannikainen et al., 2019. We introduce Computer Vision (CV) methods to enable a quick and automated analysis of the substantial amount of gathered microscopy images, which push the precision of measurements to their limit and showcase the capabilities of the LEEM technique. The applied approaches allow the direct quantification of surface properties and fundamental parameters. In addition, we introduce a Deep Learning (DL) approach to enable the practical application of an emerging LEEM diffraction technique.

This thesis presents these contributions in the following structure.

In Chapter 2, the background information underpinning the research carried out in the thesis is outlined. Section 2.1 gives the theoretical basics for the GaAs surface. It provides the fundamentals of phase coexistence, which is needed for the work presented in the rest of the thesis. Stable phase coexistence is covered in subsection 2.1.1 and coexistence during growth is covered in subsection 2.1.2. In Section 2.2, the LEEM microscope is described and the important interactions behind LEEM imaging are outlined. Section 2.3 introduces the basics of Machine Learning and Deep Learning needed for their application in microscopy imaging.

In Chapter 3, we show one of the main results in the thesis - the observation of phase coexistence and the resulting fundamental parameters that can be extracted from these measurements. We use the analytical approach developed by Hannon and Tromp, 2003 and create a processing pipeline of CV and computational methods to extract the needed information from the raw microscopy images with optimal precision, to feed to the analysis and extract fundamental surface parameters.

In Chapter 4, we detail the measurements of growth near a Gallium droplet. We image growth on a flat trail over time, giving us a spectrum of conditions along the trail over time. We apply CV methods to automate the data gathering from the images and use it to extract surface parameters.

In Chapter 5, we develop an Machine Learning (ML) method for the automated analysis of abstract and convoluted diffraction patterns, associated with a novel convergent beam diffraction technique in LEEM. The aim of the method is to streamline the adoption of the technique by enabling a quick analysis, which reduces overall

computational costs and can be applied in real-time during experiments.

Chapter 6 rounds up this thesis by outlining the conclusions from the presented work.

The author of the thesis has contributed to these results by gathering a significant portion of the used LEEM imaging data and has some contributions toward the formulation of the analysis for it. However, the author's main effort was aimed towards developing the CV, ML and other computational techniques and processing pipelines for the analysis of the imaging data.

Chapter 2

Background and fundamentals

2.1 Surface Phases

As in all crystals, the atoms in the bulk of the Gallium Arsenide (GaAs) (001) semiconductor form a well-defined lattice structure and their positions are periodic and predictable. They are arranged in the common zinc-blend structure, as shown in Figure 2.1. However, going out of the bulk of a finite crystal, the surface atoms

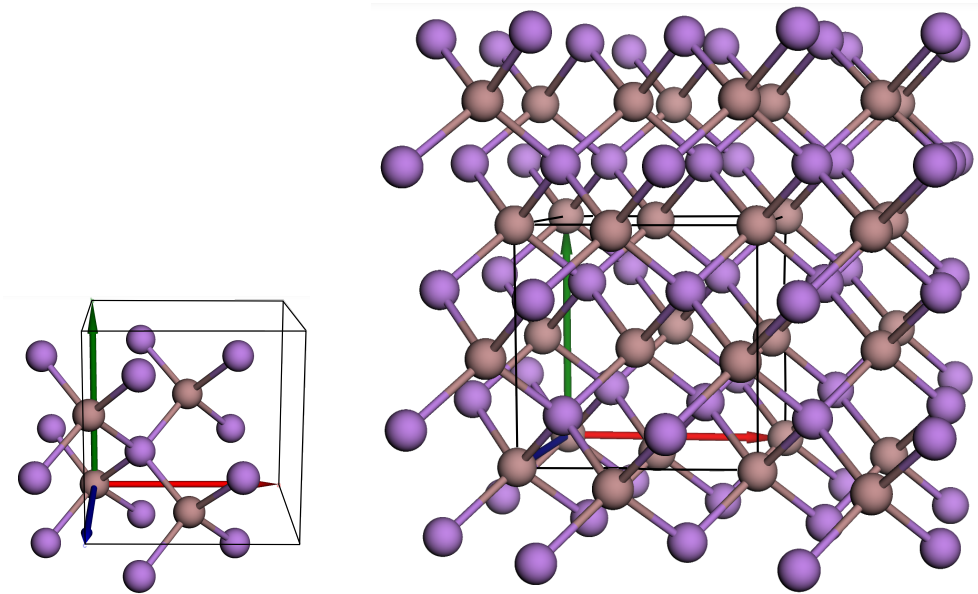


Figure 2.1: The bulk structure in GaAs (001). The GaAs unit cell (left) and the forming of a Zinc-Blende structure (right).

cannot stay in their bulk configuration, as they will not be able to fully saturate their bonds, leaving energetically unfavourable "dangling bonds". In response to this, the surface atoms rearrange in complex reconstructions to lower their energy.

These reconstructions, or phases, vary with the applied external conditions in a well-known and controllable manner to achieve the lowest accessible *surface energy*. This is determined by the formation energy of a phase - the excess energy of the surface atoms compared to the bulk atoms in the crystal. The surface phases can vary with conditions, as supplying extra energy to the surface atoms through pressure or temperature increases their mobility and gives them access to more configurational possibilities, which might result in a lower formation energy and thus - in a more stable and favourable surface phase. The surface stability is explored through theoretical Density Functional Theory (DFT) calculations to find the most favourable reconstructions, in which the surface is expected to be found at certain sets of conditions (Ohtake, 2008).

The surface reconstructions consist of repeated structures of atomic arrangements - unit cells. The unit cells are usually identified through Wood's notation, with respect to the lattice vectors a and b of the bulk unit cell. In that notation, a reconstruction will be denoted by $(m \times n)$, indicating its size through multiples of the lattice vectors m and n . For example, a (2×1) reconstruction would imply that the surface unit cell is twice as long as the (1×1) bulk unit cell in one dimension but the same in the other. Additionally, surface structures with unit cells of the same size can have additional atoms in their centres, which alters their unit cell. For example, a surface structure which is the same as a (2×2) cell, but with an extra atom in its centre will have a 45 degree rotated symmetry with respect to the bulk and be denoted as a $(\sqrt{2} \times \sqrt{2})R45$. To save the complexity of describing such cells, they are instead denoted as *centered*, so the $(\sqrt{2} \times \sqrt{2})R45$ simply becomes a $c(2 \times 2)$. Similarly, to describe arbitrary variations of the structure of the same unit cell, they are denoted by appending symbols $\alpha, \beta, \gamma, \dots$, indicating specific rotations or arrangements of that unit cell.

A common way to describe the surface phases and illustrate the most stable configurations is to use the formation energies of the phases to construct *phase diagrams* against the chemical potential of the surface. In GaAs (001), this is the relative Gallium chemical potential of the surface with respect to the bulk Ga phase at 0 K - $\Delta\mu_{Ga}$. A more negative $\Delta\mu_{Ga}$ corresponds to an As-rich surface, while $\Delta\mu_{Ga}$ getting closer to 0 means a Ga-rich surface. The phase diagram for the

GaAs(001) surface is shown in Figure 2.2. In practice, the change in the chemical potential is achieved with changes in experimental conditions such as an external material flux or temperature change. The diagram points towards the accepted $c(4 \times 4)\beta \leftrightarrow \beta 2(2 \times 4) \leftrightarrow c(8 \times 2)$ phase transition, as calculated with DFT.

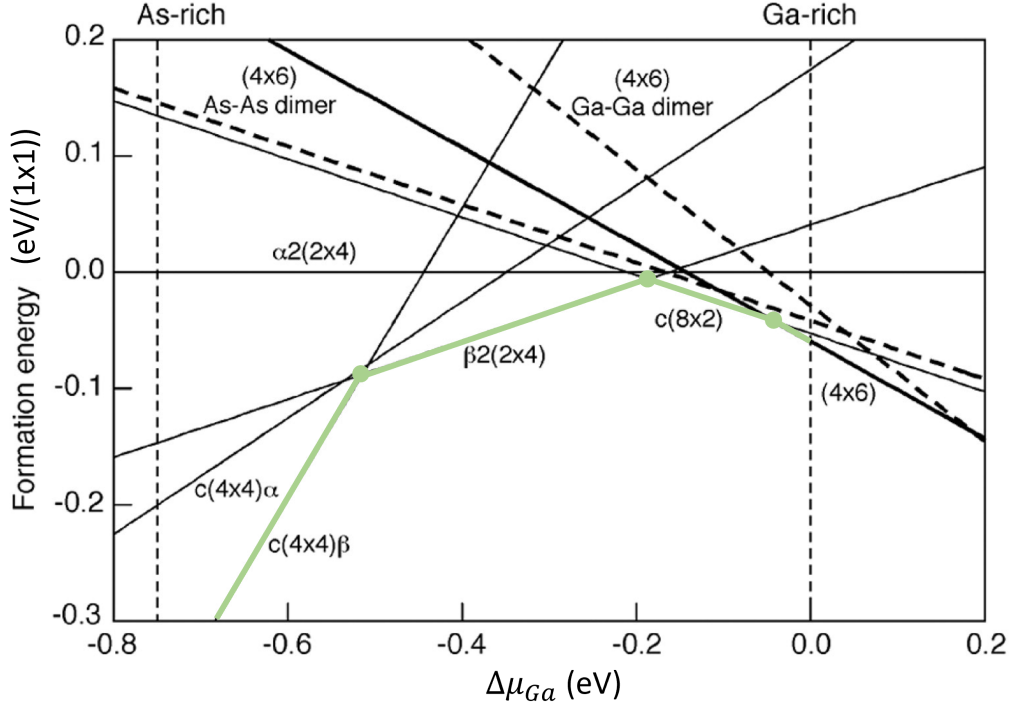


Figure 2.2: Phase diagram of the GaAs(001) surface phases, adapted from Ohtake, 2008. The phase transition is formed by the accessible phases - the ones with the lowest energy at a certain chemical potential, as marked in green.

Even though considerable research effort has been invested in deriving this phase transition (Ohtake, 2007, 2008; Pristovsek et al., 2003), a long standing question is still left open (H. Xu et al., 2002). There has been experimental evidence of the (6×6) phase occurring on the GaAs (001) surface, even though it has been theoretically shown to be unstable in all its possible atomic configurations (Ohtake, 2007). This suggests a discrepancy between the calculated and the observed phase transition on the GaAs (001) surface. Recently, *in-situ* observations with the LEEM-MBE system showed decisive evidence that the (6×6) phase is a prominent part of the phase transition path in GaAs (001) (Niu et al., 2019; Zheng, Tersoff, et al., 2016). Figure 2.3 shows the theoretical atomic configurations along the phase transition path, as observed experimentally. Observations at different experimental

conditions show the various ways the unexpected (6×6) manifests on the surface - in a large temperature range, the (6×6) *coexists* with the $c(8 \times 2)$ in a stable manner, going into a metastable coexistence at higher temperatures (Hannikainen et al., 2019), as well as during epitaxial growth. To describe this behaviour and fill the gap between theory and experimental observations, we first introduce the basics of these phase coexistence behaviours, which serve as the foundation for the detailed investigations of the stable coexistence in Chapter 3 and the metastable coexistence during growth in Chapter 4 between the (6×6) and $c(8 \times 2)$ phases.

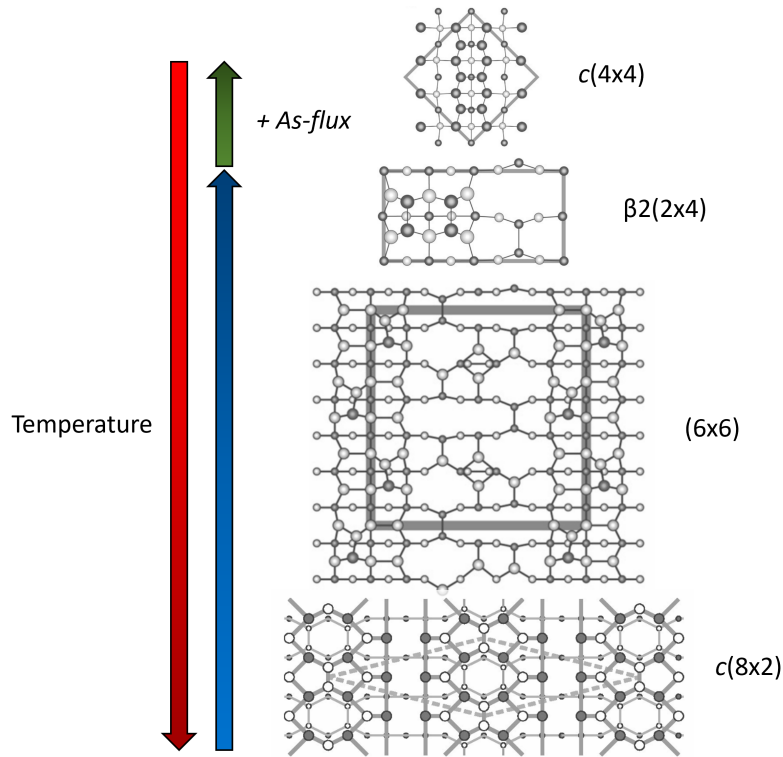


Figure 2.3: The atomic configuration of the observed phases on the GaAs (001) surface. They can be trivially reached experimentally, mostly with variations in the temperature. Adapted from Ohtake, 2008.

2.1.1 Phase Coexistence

The phase coexistence phenomenon was first suggested in an article by Marchenko, 1981, where it was considered that for two different crystal surface phases that do not have the same surface stress it is possible to have coexistence - the two phases are simultaneously present on the crystal surface with a sharp boundary between

them. This represents a first-order phase transition. Since then, some examples of such behaviour during phase transitions have been shown on Si by applying external stress (Men et al., 1988), controlling temperature (Hannon et al., 2002; Hibino et al., 2004; Swiech et al., 2002), on GaAs(001) by controlling the pressure (Galitsyn et al., 2007) and during epitaxial growth (Takagaki et al., 2006), as well as on other materials (Kern et al., 1991; Zandvliet et al., 2004).

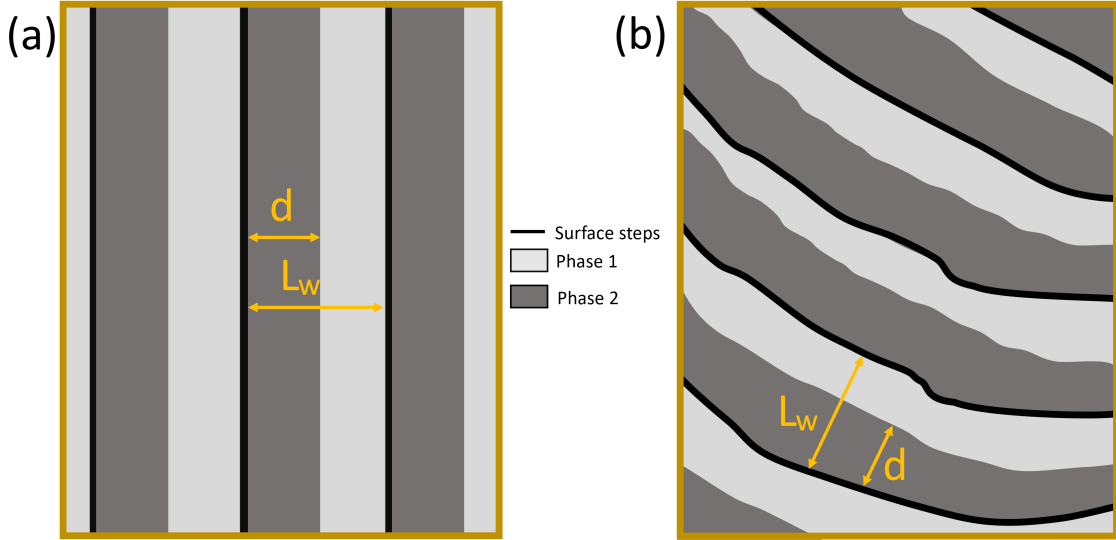


Figure 2.4: A diagram of the striped domains during a first-order phase coexistence on straight and curved steps. (a) represents the model system, with straight steps and boundaries in the same direction. It is the ideal case, for which the analysis is developed. (b) represents a more natural and more variable curved step arrangement. Although it introduces some complexity, this system is governed by the same surface effects.

Here, we utilise temperature as the main driving force behind the surface transitions, where coexistence may be observed in a temperature range around the transition temperature T_0 between two phases. The transition between the two phases is gradual within a temperature range, due to the coexistence effect being beneficial towards lowering the overall energy on the surface. To investigate the reason that can happen, we explore the main contributors towards the surface energy during that coexistence - the **boundary creation** $E_{boundary}$, **free energy difference** E_{free} and **elastic and electrostatic interactions** E_{relax} .

$$E_{total} = E_{boundary} + E_{free} + E_{relax} \quad (2.1)$$

Let us consider a surface with a terrace size of L_w , where the phases appear in

striped pattern, as illustrated in Figure 2.4, with one domain having a width of d , the other domain - $L_w - d$. The boundary creation cost is an effect of dangling bonds, local deformations and other factors along the boundaries between the two phases (Alerhand et al., 1988). Denoting the cost per unit length as C_b and the length of a boundary as L_b , the added boundary creation energy per unit area is simply:

$$E_{boundary} = \frac{C_b}{L_b} \quad (2.2)$$

The second term is a result of the free energy difference between the two phases $\Delta\gamma$. It has a temperature dependence on the entropy difference ΔS between the phases - $\Delta\gamma = \Delta S(T - T_0)$, where T is the current temperature and T_0 is the temperature of equal coverage between the two phases. The energy contribution from the free energy difference between the phases is then:

$$E_{free} = p \frac{\Delta S(T - T_0)}{2} \quad (2.3)$$

Here, p is the coverage parameter, defined as the fraction between the area of the unfavourable phase A_{unf} and the total area A_{total} :

$$p = \left(2 \frac{A_{unf}}{A_{total}} - 1\right) \quad (2.4)$$

The elastic and electrostatic energy is a product of the stress difference and the electrostatic fields at the phase boundaries, which cause local relaxation of the atoms around the boundaries.

The stress difference at a non-relaxed phase boundary can be expressed as a localised force $\Delta\lambda$, equal to that difference.

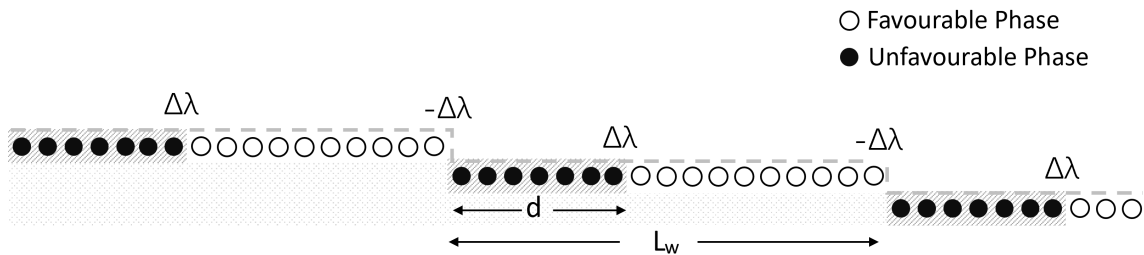


Figure 2.5: A diagram of phase coexistence on a stepped surface.

In response to $\Delta\lambda$, the atoms around the phase boundary relax. **Phase coexistence is a direct consequence of elastic relaxation at phase boundaries.**

The total force distribution, in the plane of the surface, is expressed as (Müller & Saúl, 2004):

$$\vec{F}(\vec{x}) = \Delta\lambda \sum_n \left(\delta\left(x - \left(nL_w + \frac{d}{2}\right)\right) - \delta\left(x - \left(nL_w - \frac{d}{2}\right)\right) \right) \quad (2.5)$$

In this expression, we find $x = 0$ in the middle of a stripe of width d . Here δ is the delta function and L_w is the terrace width. This equation represents a sum of the local forces, exhibited periodically only at the phase boundaries and steps, with the force being zero inside the regions with a single phase. Neighbouring phase boundaries possess opposing force monopoles $\Delta\lambda$, which repel each other, forcing equal spacing between boundaries. The resulting displacement field in response to the force in equation 2.5 can then be calculated through:

$$\epsilon(x) = \frac{2(1 - \nu^2)}{\pi\Upsilon} \int \frac{F(x')}{x - x'} dx' \quad (2.6)$$

Here, Υ is Young's modulus, ν is Poisson's ratio. The elastic energy per unit area is the work done by the force against the displacement field:

$$E_{elastic} = \frac{1}{2L_w^2} \oint \Delta\lambda \epsilon dA = \frac{\Delta\lambda}{L_w} \int \epsilon dx = \frac{2(1 - \nu^2)\Delta\lambda}{\pi\Upsilon L_w} \ln \left(\frac{L_w}{\pi a} \sin \left(\frac{\pi d}{L_w} \right) \right) \quad (2.7)$$

where a is a microscopic cut-off of the order of a unit cell size, which helps avoid short-wavelength divergences, but is not impactful towards the final results. Details on the derivation of equations 2.5, 2.6 and 2.7 can be found in Müller and Saúl, 2004. With $C_\lambda = \frac{(1 - \nu^2)\Delta\lambda}{\pi\Upsilon}$, the energy contribution from the elastic interactions becomes:

$$E_{elastic} = \frac{2C_\lambda}{L_w} \ln \left(\frac{L_w}{\pi a} \cos \left(\frac{\pi p}{2} \right) \right) \quad (2.8)$$

Here, the coverage parameter varies from $p = -1$ for full coverage of one phase to $p = 1$ for full coverage of the other, and $p = 0$ for equal coverage.

The electrostatic fields are a result of the difference in work functions between the two phases. The electrostatic energy has a similar form to equation 2.7:

$$E_{electrostatic} = \frac{1}{L_w^2} \oint dS \int v(\vec{r} - \vec{r}') \left(\frac{\Delta\phi}{4\pi} \right)^2 dr' \quad (2.9)$$

Vanderbilt, 1992 shows that from the reciprocal space sum of energies for a striped surface of alternating domains, the energy reduction is:

$$E_{electrostatic} = \frac{\Delta\phi^2}{4\pi^2 L_w} \ln \left(\frac{L_w}{\pi a} \cos \left(\frac{\pi p}{2} \right) \right) \quad (2.10)$$

Then, defining a constant for electrostatic interactions as $C_\phi = \frac{\Delta\phi^2}{8\pi^2}$, the energy due to electrostatic interactions becomes:

$$E_{electrostatic} = \frac{2C_\phi}{L_w} \ln \left(\frac{L_w}{\pi a} \cos \left(\frac{\pi p}{2} \right) \right) \quad (2.11)$$

Now we can combine elastic and electrostatic interactions to describe the total energy associated to the relaxation of atoms along the phase boundary (Hannon et al., 2001):

$$E_{relax} = \frac{2C_m}{L_w} \ln \left(\frac{L_w}{\pi a} \cos \left(\frac{\pi p}{2} \right) \right) \quad (2.12)$$

where $C_m = C_\lambda + C_\phi$.

Putting back the contributions in equations 2.2, 2.3 2.12 into equation 2.1, the total formation energy from these contributions per unit area becomes:

$$E_{total/A^2} = \frac{C_b}{L_b} + p \frac{\Delta S(T - T_0)}{2} - \frac{2C_m}{L_b} \ln \left(\frac{L_b}{\pi a} \cos \left(\frac{p\pi}{2} \right) \right) \quad (2.13)$$

Here, L_b is the length of a boundary. The coverage parameter p is the ultimate balancing factor in this equilibrium of competing forces. Neighbouring boundaries repel each other, forcing the phase boundary towards the middle of the terrace, favouring equal coverage - $p = 0$. This is balanced by the free energy difference $\Delta\gamma = \Delta S(T - T_0)$, which forces a larger area for the energetically less-expensive phase as the temperature goes further away from T_0 . This effect favours an imbalance of the coverage and pushes p to 1 or -1 . Overall, the elastic relaxation compensates for the costs of boundary creation and maintaining an unfavourable phase with a higher surface energy. These forces balance out at equilibrium and determine the configuration of coexisting domains by setting the phase boundary's overall position.

All these interaction energies at the boundary need to balance out in not only where the boundary is, but what its shape is. The force monopoles at the phase boundaries are driving the boundary towards compressing the phase with a larger tensile surface stress than the other. This leads to temporary kinks, or **fluctuations** of the boundary. They are enabled through a mass transport mechanism along the boundaries, driven by a density difference between the phases. Entropy gained through having a more random wandering boundary shape would also aid

the boundary fluctuations. This is countered by the cost of boundary creation, which pushes the boundary towards the shortest possible variant and favours a straight boundary, thus reducing the amplitudes of fluctuations. The repulsion between force monopoles at neighbouring boundaries also pushes towards a straight boundary (N. C. Bartelt et al., 1992; Hannon & Tromp, 2003).

The energy cost of creating a small deformation is governed by the **boundary stiffness** $\tilde{\beta}$. It is defined as the energy cost of introducing a bend to the boundary and combines the cost of increasing the boundary length and the cost of changing its orientation, giving:

$$\tilde{\beta} = \beta(\theta) + \frac{\partial^2 \beta}{\partial \theta^2} \quad (2.14)$$

for some θ rotation. We consider the 1D profile of a boundary $y(x)$, with $y = 0$ being the reference straight boundary, and x running along that reference. Then, as a result of the boundary stiffness, the energy change, associated to creating a small offset in the boundary from $y = 0$ is given by (Hannon & Tromp, 2001; Jeong & Williams, 1999):

$$\Delta E = \int \frac{\tilde{\beta}}{2} \left(\frac{\partial y}{\partial x} \right)^2 dx \quad (2.15)$$

The quadratic dependency of the energy change ΔE to the step deformation gradient $(\partial y / \partial x)$ suggests that smaller fluctuations, possessing a larger $(\partial y / \partial x)$, would decay much quicker. To utilise this result, it is natural to look at the Fourier transform of the boundary profile $y(x, t)$:

$$y_q(t) = \frac{1}{N} \sum_x y(x, t) \exp(-iqx) \quad (2.16)$$

In that transformation, the short-wavelength modes would be expected to have smaller amplitudes. This relationship is shown experimentally in many systems (Ondrejcek et al., 2003; Ondrejcek et al., 2005; Ondrejcek et al., 2002, 2004) and, as suggested by equation 2.15, follows a quadratic relationship between the mean squared amplitude $|y_q(q)|^2$ and the wave number q :

$$\langle |y_q(q)|^2 \rangle = \frac{k_B T}{L_b \beta q^2} \quad (2.17)$$

The repulsion between neighbouring steps and boundaries adds to the energy change in a deviation from $y = 0$ along the boundary. That repulsion can be

modelled as a quadratic potential, in analogy to a simple harmonic oscillator (N. C. Bartelt et al., 1990):

$$V(y) = cy^2 \quad (2.18)$$

For that confining potential, the step distribution is a Gaussian shape:

$$P(x) = \frac{1}{\sqrt{2\pi}\sigma} \exp\left(-\frac{x^2}{2\sigma^2}\right) \quad (2.19)$$

Where σ is the standard deviation of the Gaussian, given by N. C. Bartelt et al., 1992 to be:

$$\sigma^2 = \frac{k_B T}{\sqrt{8c\tilde{\beta}}} \quad (2.20)$$

If we consider the confining potential as the main driving force behind the boundary position in equation 2.1, we can obtain an expression for the confining constant. Keeping in mind that the confining potential is per unit length, from equation 2.18, the confining constant c becomes:

$$c = \frac{1}{2} \frac{\partial^2(L_b E)}{\partial d^2} \quad (2.21)$$

Differentiating, we get:

$$c = \left(\frac{\pi}{L_b}\right)^2 C_m \left(1 + \tan^2 \frac{p\pi}{2}\right) \quad (2.22)$$

If we consider the fluctuations when the coverage of the two phases is equal, $p = 0$, for the width of the Gaussian distribution, for the variance σ^2 we get:

$$\sigma^2 = \frac{k_B T L_b}{2\pi(2\tilde{\beta}C_m)^{\frac{1}{2}}} \quad (2.23)$$

The fluctuations distribution is directly accessible from experiments and, if we know the boundary stiffness $\tilde{\beta}$, **gives a direct measurement of the elastic and electrostatic interactions constant C_m .**

2.1.2 Coexistence in Growth

The knowledge of how a surface exhibits phase coexistence is valuable in practice, as the quality of the grown material is directly linked with the quality and uniformity

of the substrate surface - growing on the appropriate surface reconstruction can be impactful. If one wants to grow in a region of conditions where a stable phase coexistence would appear, as described above, a logical workaround to avoid the extra complexity of the two phases on the surface is to move away from the conditions just enough so that only one of the two phases remains on the surface and grow there. Despite everything, in such a situation the surface can still exhibit phase coexistence between the two phases during the deposition itself.

To understand this phenomenon, let's explore a newly formed small circular island on a flat surface during growth. It can be thought of as a growing circular terrace with a height of one atomic layer, bound by a step. As we have seen in Section 2.1.1 above, interactions at phase boundaries and steps can help in stabilising a less favourable surface phase (Plass et al., 2001). As is observed in the experiments

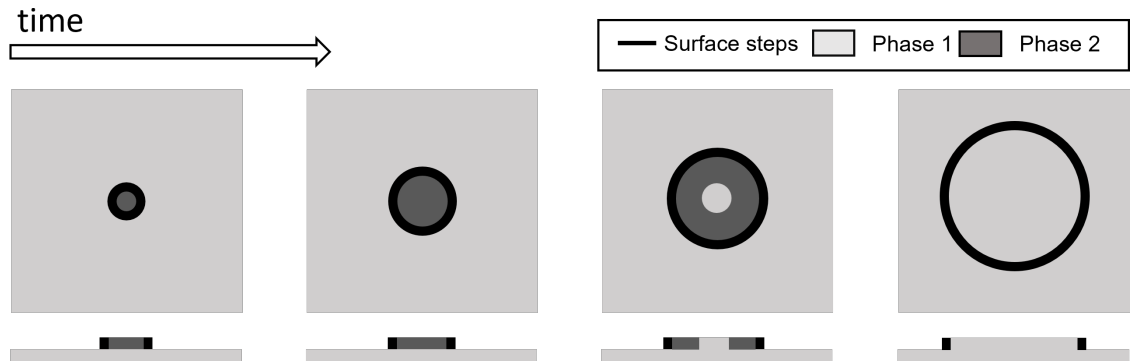


Figure 2.6: A diagram demonstrating the evolution of a step island containing an unfavourable phase (Phase 2).

conducted in Chapter 4 during MBE growth deposition, the less favourable phase appears on these newly formed islands. The islands continue growing until the less favourable phase gives way to the main phase of the surface, as depicted in Figure 2.6.

The system can be described through the probability per unit area and time ρ that the favourable phase nucleates on the unfavourable, at which point we lose one of the unfavourable domains. The probability distribution for the phase transformation inside an island is derived by Hannikainen et al., 2019 as:

$$f(R) = \rho \frac{\pi R^2}{\nu} \exp \left(- \frac{\rho \pi R^3}{3\nu} \right) \quad (2.24)$$

The probability is dependent on the radius of the island R and the step velocity

during growth ν , which is experimentally found and shown to be constant over time in Chapter 4. This yields the average domain radius upon phase transformation through $\langle R \rangle = \int_0^\infty R f(R) dR$. The average domain radius upon transformation is then:

$$\langle R \rangle = \Gamma(4/3)^{-1} \left(\frac{3\nu}{\pi\rho} \right)^{\frac{1}{3}} \quad (2.25)$$

where Γ is the Gamma function. The nucleation probability parameter ρ is dependent on the energy barrier of nucleating the new phase E_{barrier} and follows the Arrhenius form:

$$\rho = \rho_0 \exp \left(- \frac{E_{\text{barrier}}}{k_B T} \right) \quad (2.26)$$

Here, ρ_0 is the initial number of domains, k_B is the Boltzmann constant and T is the temperature on the surface. The energetics of a circular island, covered by the unfavourable phase are similar to the form of Equation 2.13 in Section 2.1.1 previously. In a dilute regime, where the unfavourable phase is pronouncedly the minority phase in the coexistence, different nucleating islands do not interact with each other and we can focus on the energetics of a single island. The total energy for an island of radius R sums up the contributions in 2.1 and is given by Ng and Vanderbilt, 1995:

$$E_{\text{total/island}} = 2\pi R C_b + \pi R^2 \Delta\gamma - 2\pi R C_m \ln \left(\frac{4R}{ae^2} \right) \quad (2.27)$$

Even though the form is similar to the stripe pattern case, there are differences for each of the energetic contributions in the growth island energetics that are worth noting. The first term represents the boundary creation cost. In the circular island case, the length of the boundary grows as the unfavourable domain grows. This leads to a linear increase to the boundary creation cost, in contrast to the approximately constant boundary creation cost of the stripe pattern case. Concerning the second term, the difference in free energies $\Delta\gamma$ in the case of growth additionally incorporates a contribution from the flux of atoms. The effect of the supersaturation on the surface due to the external flux introduces a change in the chemical potential μ and is equivalent to changing the local free energy difference by an amount $\Delta N(\mu - \mu^c)$, where ΔN is the difference in reconstruction atoms in the two phases and μ^c is the chemical potential at the phase transition. In other words, the presence of extra atoms favours the phase whose reconstruction incorporates a larger number

of atoms. In the third term, which accounts for the elastic interactions, there is a lack of periodicity, as illustrated in Figure 2.7. This leads to a monotonic decay of the elastic interactions as the island radius R increases.

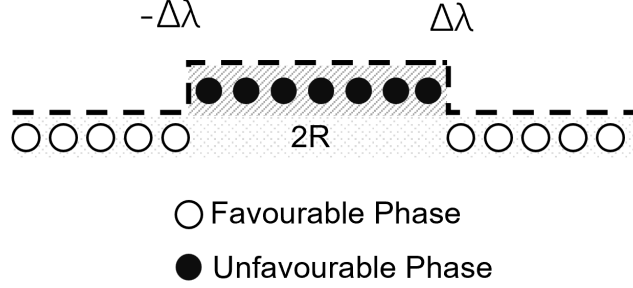


Figure 2.7: A diagram of the elastic interactions in a step island containing an unfavourable phase.

The barrier energy is when the island grows enough that the minority phase becomes unstable towards the majority phase. In other words, $E_{\text{barrier}} = E_{\text{total/island}}(R')$ at some radius R' , where $\partial E_{\text{total/island}}/\partial R = 0$. When this is used to express the nucleation probability in Equation 2.26, this type of **coexistence during growth** can be described through the domain radii upon transformation $\langle R \rangle$ with Equation 2.25.

2.2 Low-energy electron microscopy (LEEM)

Low-Energy Electron Microscopy (LEEM) belongs to the family of *cathode lens* electron microscopy, where the sample itself is used as a cathode, emitting the electrons out of which the image is formed. LEEM does that through the effect of *elastic backscattering* - the reflection of an electron beam from the crystal surface without loss of energy. LEEM is designed to study the structure and morphology of surfaces, thin-films and surface-based nanostructures with high temporal and spacial resolution. This is possible due to the low energy of the electrons, which limits their penetration depth and makes LEEM very surface-sensitive. The nature of the interaction between the electron beam and the surface enables high contrast between different structures and reconstructions on a crystalline surface, enabling the detailed imaging of surface dynamics *in situ*. It is a sample-preserving technique, which opens up its application to beam-sensitive materials (Bauer, 2014).

2.2.1 Low energy electrons

LEEM uses electrons with energies in the range of 0 – 100 eV, with the de Broglie wavelength of electrons with such energies being of the order of a few Å. This wavelength is similar to X-ray wavelengths, and is comparable to typical atomic separations in solids. For this reason, the elastic scattering of the electrons off the crystalline surface enables diffraction in LEEM imaging. This provides a great advantage, as LEEM is able to tap into both real space and reciprocal space.

The reflection during elastic backscattering off of a crystalline surface occurs at certain discrete diffraction angles, which are determined by Bragg's condition, requiring constructive interference between backscattered electrons. Since the electrons are *elastically* backscattered, they must also satisfy the requirement for conservation of momentum. These discrete Bragg angles can be practically observed as the reciprocal space diffraction imaging - the places where bright spots are allowed to form on a diffraction image, as they are focused to the same image spots by the microscope's optical system. Bragg's condition can be visualised through the construction of the Ewald sphere. With the shallow penetration depth of the low energy electrons, we can simplify the construction of the Ewald sphere to account for just two dimensions, assuming the low energy electrons only 'see' the first atomic layer of a surface. An electron of energy E will have a momentum of:

$$\vec{k} = \frac{2\pi}{h} \sqrt{2m_e E}$$

where h is Planck's constant and m_e is the electron mass. This momentum must be conserved throughout the interaction. We can split the total momentum into components $\Delta\vec{k}_\perp$ and $\Delta\vec{k}_\parallel$, perpendicular and in-plane of the surface. As a consequence, If, for example, the electron gains an angle of deflection, as permitted by Bragg's condition, it will gain an in-plane component of its momentum $\Delta\vec{k}_\parallel$, which must be compensated by a reduction in its surface-perpendicular component $\Delta\vec{k}_\perp$, so that the magnitudes of the momenta before and after interaction remain the same and only the direction of momentum changes:

$$\|\vec{k}_i\| = \|\vec{k}_f\| = \|\vec{k}_\parallel\| + \|\vec{k}_\perp\|$$

The size of the sphere corresponds to the energy of the incident electrons. The reciprocal lattice is extended by building imaginary rods at the reciprocal atomic

spacing of the surface. The crossing points between the Ewald sphere and imaginary rods are where diffracted electron beams are allowed to reflect. This translational symmetry parallel to the surface dictates that \vec{k}_{\parallel} can only change in multiples of the lattice vector upon reflection. As a consequence, the diffraction pattern spacings observed in the Low-Energy Electron Diffraction (LEED) pattern are equivalent to a lattice vector on the surface and the constants of a unit cell can thus be directly determined. A diagram illustrating the construction of the Ewald sphere on top of a crystalline surface is shown in Figure 2.8.

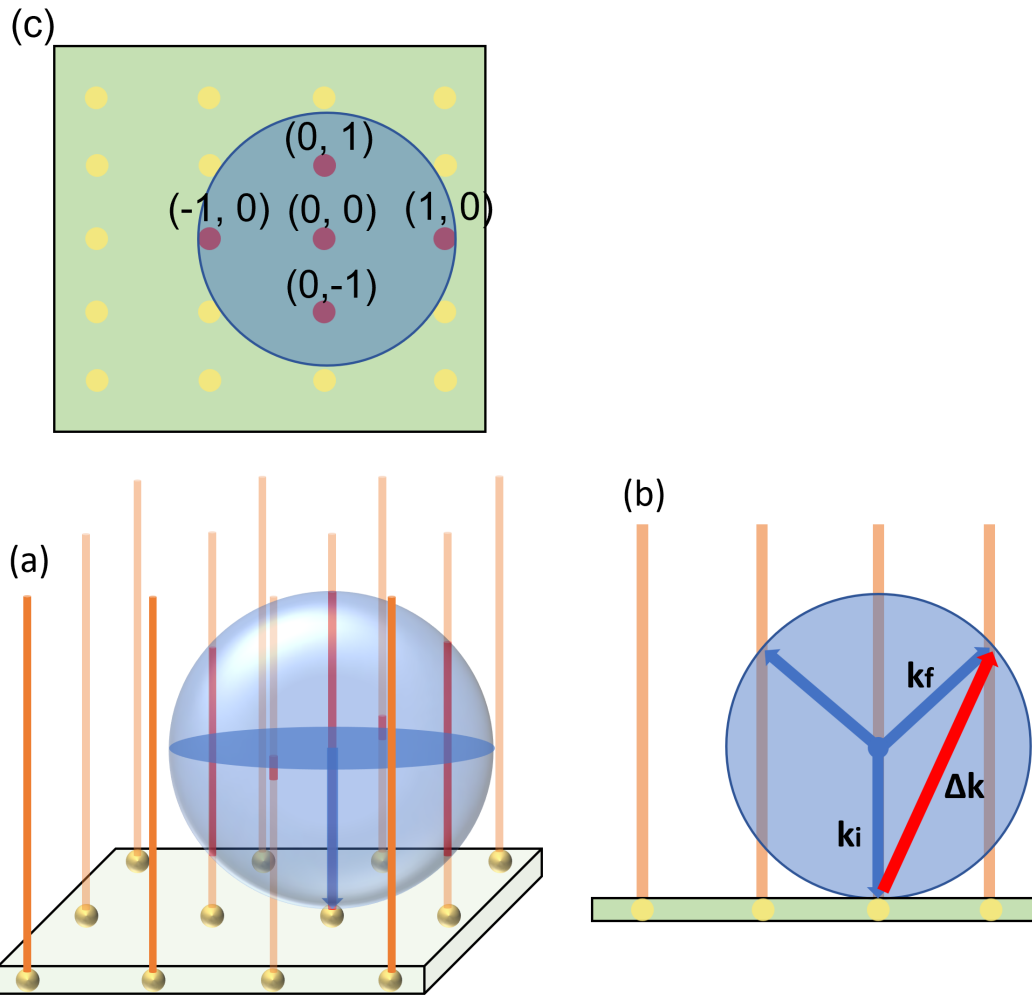


Figure 2.8: A diagram of the construction of the Ewald sphere. (a) The sphere is constructed on top of the reciprocal surface, where the incident beam falls. The Ewald sphere represents Bragg's condition. The reciprocal lattice is extended with imaginary rods, built at the reciprocal atomic spacing. Where the rods cross the sphere, the diffraction conditions are met (b) and beams will form a diffraction spot (c).

This construction suggests that the visible diffraction spots remain constant

with changes in electron energies. However, in practice we observe modulations in diffraction spots as we vary the electron energy, due to the finite, but multiple layer penetration of the electrons. This can be represented by modulations in the rods in the Ewald sphere construction, as shown in Figure 2.9. In practice, we observe this modulation when we vary the electron beam energy and diffraction spot intensities change due to the Ewald sphere growing and shrinking and passing through the rod modulations.

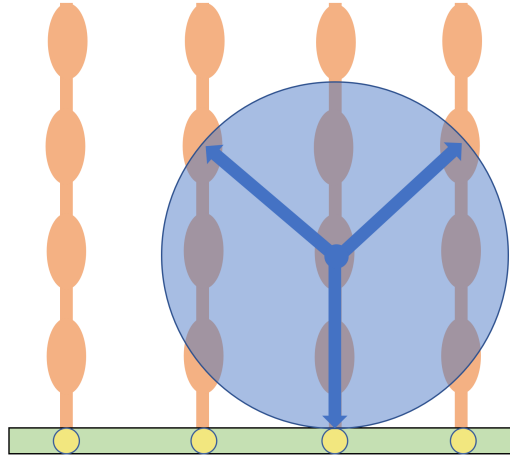


Figure 2.9: A diagram of the Ewald sphere for a finite penetration depth of electrons.

A more comprehensive description of diffraction pattern formation is achieved with the paradigms of multiple elastic scattering and the Bloch wave approach (Flege & Krasovskii, 2014; Hove & Moritz, 2022; Krasovskii, 2004).

The strong surface sensitivity of the low energy electrons leads to the main two contrast mechanisms of the LEEM microscope - *phase contrast* and *diffraction contrast* (Bauer, 2014; Flege et al., 2012).

Phase contrast occurs due to variations in the morphology of the sample, which cause spacial phase shifts to the electron waves without otherwise affecting their amplitude. A common observation due to this effect is a surface step, where the height difference around the step causes the phenomenon (Altman et al., 1998). As the electron wavelengths in LEEM are of the order of atomic layer thicknesses, they are also of the order of surface step heights. The phase shift ϕ is then directly dependent on the path length difference d and the electron wavelength λ :

$$\phi = \frac{2\pi d}{\lambda}$$

Phase contrast then originates from the interference of the electron waves, reflected from the opposite sides of a step. Practically, a range of phase shifts can be sampled by varying the electron energy.

Diffraction contrast, also known as amplitude or reflectivity contrast, occurs due to the difference in reflectivity of different structures on the sample surface. It is observed as a spacial variation of electron intensity after reflection from different surface reconstructions and structures and is sensitive to the incident electron energy. It is due to the unique sets of diffraction peaks, caused by different structures with different lattice and structure factors.

2.2.2 The LEEM imaging system

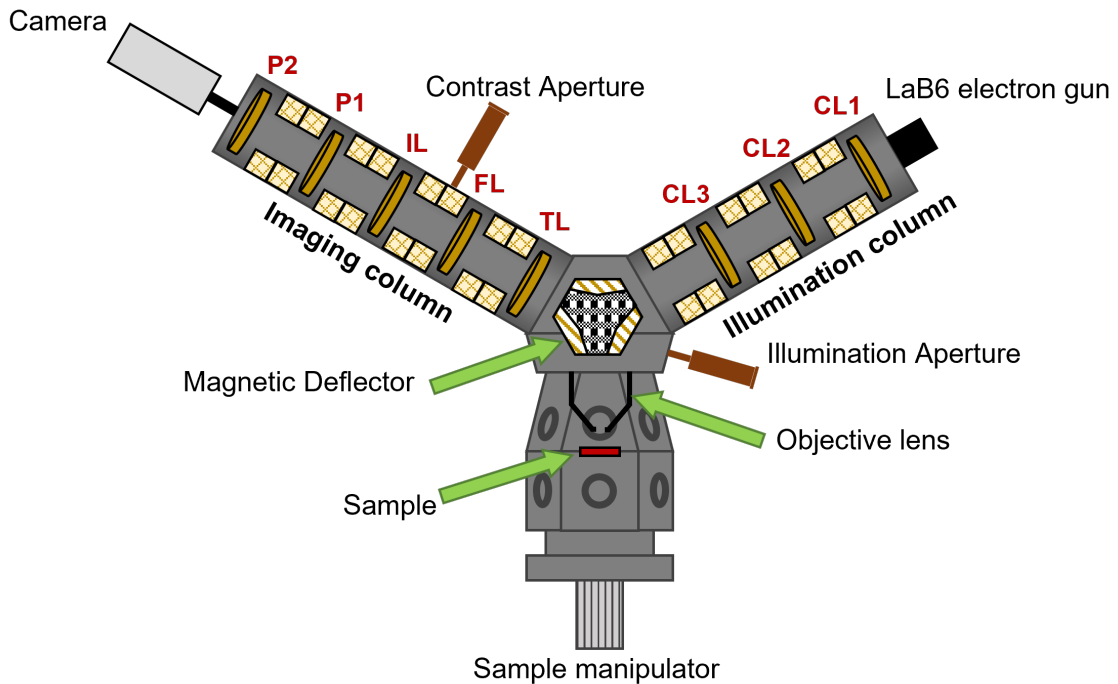


Figure 2.10: A diagram of the Elmitec LEEM-III with its key components labelled. The Illumination column contains three Condenser Lenses (CL), who's job is to deliver a well-shaped, collimated and coherent beam to the sample. An illumination aperture at the end of the Illumination column allows the limiting of the beam size and shape, as it reaches the sample. The beam passes through a beam splitter in the middle of the apparatus, which deflects the incident beam towards the sample and the reflected beam towards the imaging column. The imaging column uses a Transfer Lens (TL), a Field Lens (FL), an Intermittent Lens (IL) and two Projective Lenses (P1, P2) to focus and scale the image formed by the objective lens onto a Multi-Channel Plate, followed by a camera.

The basic setup of a LEEM instrument is illustrated in Figure 2.10. It follows similar design patterns to Transmission Electron Microscopy (TEM) instruments, controlling the electron beam with electromagnetic lenses, which are aligned by deflectors. The setup can be broadly divided into three sections. The beam is produced by an electron gun and it initially passes through the Illumination column, which serves to collimate and control the beam shape, as it reaches the sample. Then, the beam passes through a beam splitter and an immersion objective lens to deflect the beam towards the sample, focus it and slow it down. After the electrons interact with the sample, they go through an Imaging column, which focuses the reflected beam to form a high resolution image. Beam apertures are placed at the end of the Illumination column to control the beam size as it reaches the sample, and in the Imaging column, where the reciprocal image is formed, to filter out diffraction spots and enable different LEEM imaging modes, which are detailed in Section 2.2.3 below. The pressures throughout the LEEM system are maintained in the Ultra-High Vacuum (UHV) order range using ion pumps.

The design of the LEEM itself has historically posed several challenges before the technique could become a routine reality. To minimise the effects of imperfections in the lenses or alignment, the beam passes by the microscope lens setup at 20 keV, and to achieve the low electron energies in the order of several eV, it must be decelerated with rates of about 10 keV mm^{-1} . This is achieved with the electrostatic immersion objective lens, which places the sample in a strong electrostatic field, as shown in Figure 2.11.

As the beam is reflected back from the sample, it tracks back its previous path. Overall, it passes through the objective lens twice. The first pass focuses the beam onto the sample, and the second pass forms a real image of the sample. The uniformity and strength of the electrostatic immersion field between the two passes is a main factor in the overall performance of the microscope (Tromp, 2000). To split the "folded" beam into an incident and a reflected beam, a magnetic beam separator, or the beam splitter, is designed to deflect the beams at opposing angles in both directions (Tsuno et al., 1995), which in the case of the LEEM-III are 60° deflections.

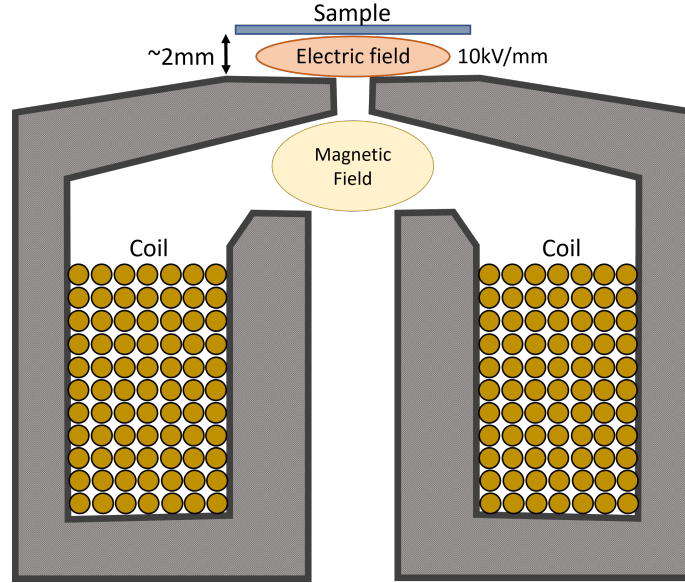


Figure 2.11: A schematic of the immersion objective lens, designed to both focus the beam onto the sample through its magnetic lens, and slow the beam down between itself and the sample through an electrostatic field. As the beam is sensitive to stray magnetic fields when it is slow, the lens must isolate the magnetic field well.

2.2.3 LEEM Techniques

There are several different configurations of the LEEM instrument, which allow imaging in different modes, each carrying its own benefits. Here, we give short overviews of the main imaging modes the LEEM system provides.

Photoemission Electron Microscopy (PEEM) is a type of imaging, where light sources, such as simple Hg lamps in standard LEEM instruments and synchrotron based light sources in dedicated beamlines, are used to illuminate the sample and excite photoelectrons. The tunability of light energy and polarisation enable powerful techniques, such as x-ray absorption spectroscopy and angle-resolved photoemission spectroscopy.

For the work in this thesis, PEEM finds an important role in the initial alignment procedure of the instrument, where it allows the Imaging column lenses to be aligned independently of the Illumination column.

Mirror Electron Microscopy (MEM) is an imaging mode, where the electrons are given such little energy that they are stopped by the immersion field before they reach the surface of the sample. Instead, they are reflected in front of

the sample surface and only interact with its 'near-sample' field. The reflected electrons carry information on the surface morphology, creating contrast between surface objects. It is especially useful for imaging surfaces without a crystalline structure, where topological information can still be gathered, despite the inability to use other LEEM methods.

For the work in this thesis, this mode is used during the routine alignment of the instrument and during surface preparation, before experiments begin.

LEED and micro-LEED (μ LEED) allow the imaging of reciprocal space when the lens configuration of the instrument is set to image the back-focal plane. This LEED configuration produces diffraction patterns from a crystalline sample. When the illumination aperture is used to limit the beam to a small spot on the sample surface, a μ LEED diffraction pattern is produced only for that spot. This method is used to track the surface structure and identify the observed surface phases during experiments.

Bright Field (BF) and Dark Field (DF) imaging uses the instrument's contrast aperture on the LEED pattern to isolate a single beam and produce real-space images from only that specific reflection. If the selected beam is the central (00) beam of the diffraction pattern, which usually has the strongest intensity, we enter the BF imaging mode, while if another beam is isolated, we enter the DF imaging mode. Both these imaging modes utilise the diffraction contrast mechanism to create contrast between different surface structures and phases and are the main imaging modes for the duration of most experiments. While BF imaging produces more intensity and is able to produce higher quality images, DF enables the imaging of a selected single surface phase, resulting in very high contrast imaging.

Other techniques bring improvements and unlock new possibilities in LEEM imaging. The recently developed Selected Energy Dark Field Low-Energy Electron Microscopy (SEDFLEEM) technique allows the optimisation of electron energy during DF imaging, resulting in discrimination of several phases when imaging through common diffraction spots (Niu et al., 2019). Another newly developed technique allows the analysis of I-V curves mapping of LEEM im-

ages for the precise identification of different surface phases on the sample surface (Masia et al., 2022).

2.2.4 Resolution Limits

While temporal resolution becomes important in some applications, such as in Chapter 3, spacial resolution is generally one of the most important imaging conditions in most experiments. The resolution of a LEEM instrument, such as the LEEM-III, is limited mainly by *chromatic aberrations*, *spherical aberrations* and *diffraction limit* (Altman, 2010; Bauer, 2014; Flege et al., 2012). These instrument limitations also affect the contrast during image formation (Pang et al., 2009; Yu et al., 2019). Usually, mirror-based methods are used to compensate spherical and chromatic aberrations in aberration-corrected instruments (Tromp, 2019). The LEEM instrument’s ultimate theoretical limit without extra correcting devices is 3 – 8 nm, depending on the used electron source (Bauer, 2014; Tromp et al., 1998). While mechanical and electrical instabilities can also have an impact on the resolution, they are usually negligible in well-designed instruments, compared to the main three factors, which we describe shortly here.

Diffraction limit This effect arises in LEEM when using the contrast aperture.

The size of the aperture is the deciding factor here. A trade-off between a small aperture size, which creates a small acceptance angle of the selected beam and increases the diffraction limit, and a large aperture, which allows other aberrations to dominate the resolution limits is necessary.

Chromatic aberrations are caused by the change of focal length with electron energy variations. These variations are a result of the energy spread of the electron gun. With the energy spread of the LaB6 electron gun ($\Delta E \approx 0.7\text{eV}$), the Elmitec LEEM-III microscope resolution is limited to about 8 nm. Field emission guns usually have a smaller energy spread, at the cost of lower imaging intensity. Electrostatic tetrode mirror correctors can be used to compensate for this effect and bring improvements in the instrument’s resolution (Tromp et al., 2013).

Spherical aberrations are a result of the electrons travelling at an angle to the

optical axes of lenses. The electrons in the beam would then be deflected towards a slightly different focal point, causing image deterioration. This is corrected with the alignment procedure, where the lens deflectors are adjusted to make sure the beam is aligned to the optical axis of the instrument.

2.2.5 Advantages of LEEM

The LEEM microscope is one of a number of electron microscopies available. However, it comes with its distinctive properties and brings key advantages that make the data gathered by it unique and a valuable addition to surface science observations (Altman, 2010). Its benefits enable the monitoring of real-time dynamics of crystal surfaces *in-situ*, in a variety of experimental conditions.

Surface sensitivity The low energy electrons have a very short penetration depth, which is just 1-2 atomic layers at its minimum around 50 eV leads to the high surface sensitivity of LEEM. The penetration depth at very low energies rises to the orders of a few nm, enabling the probing of deeper layers, while also experiencing a sharp increase in surface reflectivity, enabling short acquisition times during experiments.

Structural sensitivity LEEM images with high contrast between surface structures and phases, due to phase and amplitude differences in reflected electrons. The variation of electron wave amplitudes arises from their reflections from parts of the surface with different reflection coefficients. These spacial variations of the amplitude depend on the incident beam energy, and as a result, contrast changes with electron energy variations. This effect is utilised in BF and DF imaging.

Non-scanning The electrons in LEEM imaging arrive at the sample surface as a collimated, coherent beam that illuminates a surface area simultaneously. The resulting image is formed from information, gathered at the same time from the surface. This ensures that any dynamical effects are truthfully recorded in every image, without needing to account for scanning rates during imaging.

Sample preserving The electrons arrive at the surface with very low energies during LEEM imaging and it is therefore suitable for imaging beam-sensitive

Parameter	Elmitec LEEM-III limit
Max. Resolution	8 – 10 nm
Max. Acquisition Time	20 fps
Min. Background Pressure	1×10^{-10} Torr
Max. Sample Temperature	1200 °C

Table 2.1: A summary of our practical experimental condition limits with the Elmitec LEEM-III.

surfaces. The effects of burning and charging samples are negligible, and there are no effects on the surface dynamics, brought by the imaging.

The LEEM-III at Cardiff University is specifically designed to emulate the growth conditions during Molecular Beam Epitaxy (MBE) growth of III-As materials. It is equipped with a Gallium, Indium and Arsenic sources and can bring the samples to more than 1200 °C. The experimental conditions limits are shown in Table 2.1.

2.3 Computer Vision for microscopy imaging data

The copious amounts of imaging data that the LEEM microscope produces open a wide plain for analysis, the manual completion of which requires significant effort and exposes the studies to errors and inconsistencies. For this reason, the data analysis throughout the work presented in this thesis is approached with Computer Vision (CV) algorithms and purpose-built data analysis pipelines, through which the extraction of information becomes systematic, consistent and precise.

With the impressive advancements of Machine Learning (ML) and Deep Learning (DL) algorithms in the domain of images, it is very tempting to solely focus on their usage and forget about the decades worth of classical CV algorithms developed, tested and established with time. However, even though the new State-Of-The-Art (SOTA) algorithms have been shown to outperform the old generation in many CV tasks, certain advantages still lie in the older methods. To begin with, traditional CV methods are quick in simple tasks, since they have been incrementally improved and optimised with time and are a good alternative to the complexity of training an ML algorithm. Furthermore, the traditional algorithms are founded in mathematical manipulations and as a result are more stable, predictable and explainable compared

to their ML counterparts. Additionally, there are applications of traditional CV methods, which have still not been clearly surpassed by ML and DL techniques in fields, such as in image enhancement, object tracking, optical flow and image stitching. Finally, certain weaknesses can emerge with the application of the ML and DL approaches, such as lack of sufficient training data, or data labelling capabilities, which can become a barrier. In such situations, traditional methods can still provide a powerful solution. Overall, ML and DL methods have shown clear superiority in many fields, but traditional CV methods still have a plethora of applications. In this work, we make use of both approaches, depending on the tasks at hand. For the purposes of preprocessing and object tracking in Chapters 3 and 4, we construct pipelines of traditional CV algorithms, while for the more complex analysis in Chapter 5, we utilise ML and DL approaches.

2.3.1 The use cases of traditional Computer Vision

LEEM imaging is powerful in its temporal and lateral resolution, which allows observation of surface dynamics on a nanometer scale. However, the images naturally come with inherent imperfections, which we address to improve the quality of our observations. CV methods can become a powerful tool to mitigate imaging limitations and enable a new level of precision in measurements, as well as to extract new information from images (de Jong et al., 2020). In the following section, we outline the building blocks of our CV pipelines that we use for preprocessing and analysing our LEEM imaging data. The 'toolbox' of algorithms was built in Python, mainly using the implementations in *scikit-image* and *OpenCV* (Bradski & Kaehler, 2008; van der Walt et al., 2014).

Sample Drift

A frequently observed phenomenon during LEEM imaging is the imaged crystalline surface appearing to slowly move during imaging. This can be due to the sample itself moving slowly as a result of small temperature variations, electrostatic effects due to small sample charging, or outside disturbances during the experiment. Similarly, the electron beam may drift due to some instabilities in the imaging system, or variations in the chamber's background pressure. In order to observe events

over time, this drifting motion must be accounted for.

To address the issue, we use the *scikit-image* implementation of template matching, followed by an applied translation function to our images. For a sequence of images, a template is taken from the central regions of the first image and the best match is sought using normalised cross-correlation of the Fourier transform convolutions of the template and the second image (Briechele & Hanebeck, 2001; J. P. Lewis, 1995). The normalized cross-correlation (NCC) function between a template image T and a search image I at position (x, y) can be expressed mathematically as:

$$N(x, y) = \frac{\sum_{i,j} (T_{i,j} - \mu_T)(I_{i',j'} - \mu_I)}{\sqrt{\sum_{i,j} (T_{i,j} - \mu_T)^2} \sqrt{\sum_{i,j} (I_{i',j'} - \mu_I)^2}} \quad (2.28)$$

where μ_T and μ_I are the mean pixel intensities of the template and search images, respectively. The corresponding pixel positions i', j' in the search image for the template position (i, j) are given by $i' = i + x$ and $j' = j + y$.

With the best match coordinates, the subsequent image is aligned to the initial one through a simple linear translation with a similarity transformation. This is done iteratively for every pair of images sequentially.

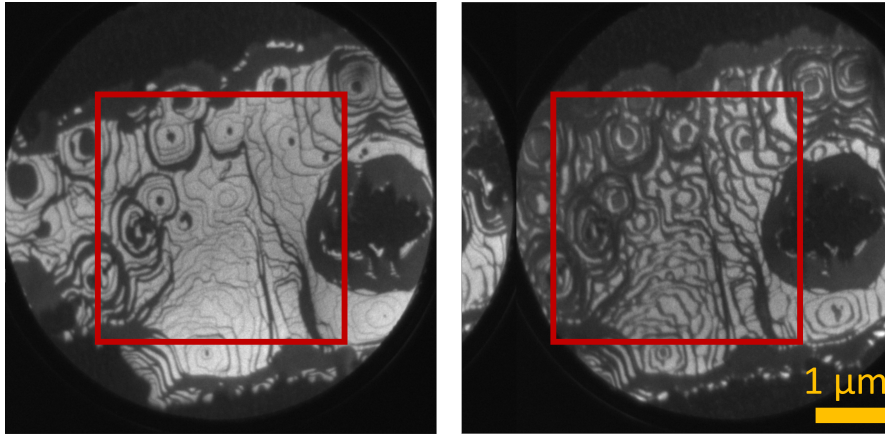


Figure 2.12: Drift correction example on a set of images, gathered during a LEEM experiment. The section lined in red is the part of the image that was matched to the previous template, and used as a new template to be matched with a section of the next image. Due to the sequential approach to alignment, where each frame is aligned to the previous one, instead of a fixed template, imaging sequences with surface dynamics that gradually change the layout, such as in the given example frames, can still be aligned well.

Intensity Gradient

Another common effect is observing an intensity gradient, both spatially along the image, and temporally, across subsequent frames. The gradients within a single image are due to an uneven illumination of the electron beam on the surface and larger Field Of View (FOV) imaging suffers more from this effect. The temporal variations are due to instabilities in the electron beam source. These intensity variations can be tackled with histogram equalisation methods, which balance the images and increase contrast.

The simplest approach to unifying the intensities in the image data collected throughout an experiment is to normalise it to a single intensity range of 0 to 1. This is useful when most of the images are uniform and with high quality. It avoids adding extra complexity to the pipelines, but due to its linearity, it suffers from drawbacks in images with low quality or with limited saturation, where contrast may be lost. It is used in the work in Chapter 4, where the imaging had no significant noise or contrast limitations.

Applying histogram equalisation carries the extra benefit over linear normalisation of preserving the relative contrast of different objects and enhancing the overall contrast in the image. It is agnostic of the image content, making it more useful over larger and more varied image datasets. This ensures uniformity across subsequent images. A further improvement comes with using adaptive histogram equalisation techniques, which treat different regions of the same image separately. Using the further improved Contrast Limited Adaptive Histogram Equalization (CLAHE) method carries the extra benefit of limiting the amplification of noise, making it valuable for large datasets of noisy images with low contrast (Pizer et al., 1987). It is used in the work in Chapter 3, where the images were taken on the limits of the LEEM microscope's capabilities. The three general approaches to intensity equalisation are demonstrated with an example in Figure 2.13.

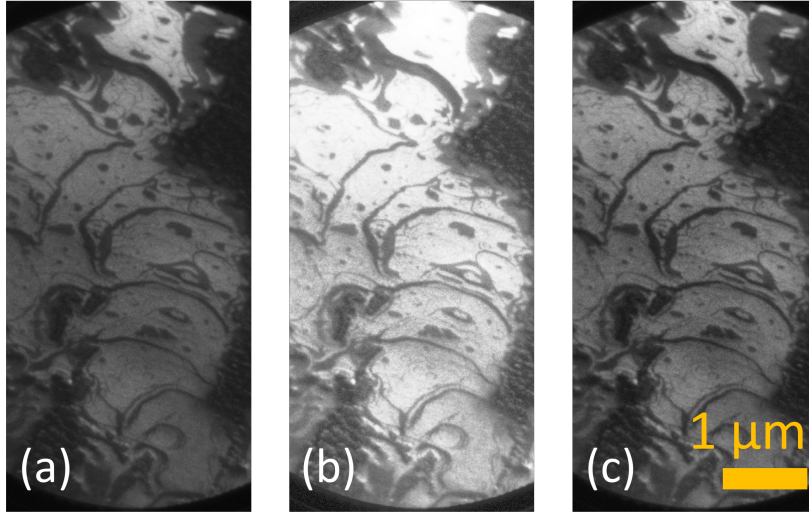


Figure 2.13: Histogram equalisation examples of a LEEM image with a mild intensity gradient due to imperfect alignment. The linear normalisation (a) does not improve image contrast. The global histogram equalisation (b) brings improvements of contrast, but suffers from over-saturation due to the intensity gradient in the image. The CLAHE method (c) keeps the information in the image, while still producing incremental improvements in the image contrast.

Noise reduction

Noise reduction is a fundamental task in image processing that aims to remove unwanted noise from images while preserving important image features. There are two broad categories of noise reduction methods: standard methods and edge-preserving methods.

Standard Linear Translation-Invariant (LTI) methods, such as median filtering and Gaussian smoothing, are simple and effective techniques for reducing noise in images. Median filtering replaces each pixel with the median value of its neighborhood, which loses the finer features on the surface, but reduces noise. Gaussian smoothing convolves the image with a Gaussian kernel, which results in a smoother image with reduced noise.

Edge-preserving methods, such as bilateral filtering and Non-Local Means (NLM) filtering, are designed to preserve important image features while reducing noise. Bilateral filtering takes into account both the spatial distance and the intensity difference between neighboring pixels when filtering the image. This allows the method to preserve edges and other important image features while removing noise. NLM filtering uses a similar approach, but instead of computing the intensity difference

between neighboring pixels, it compares the similarity between patches of pixels in the image. This allows the method to preserve texture and fine details while removing noise. While the edge-preserving methods are able to reduce noise without deteriorating image information, they are more computationally expensive and are not suitable for real-time applications. Examples of the effects of some of the most widely used denoising methods is shown in Figure 2.14.

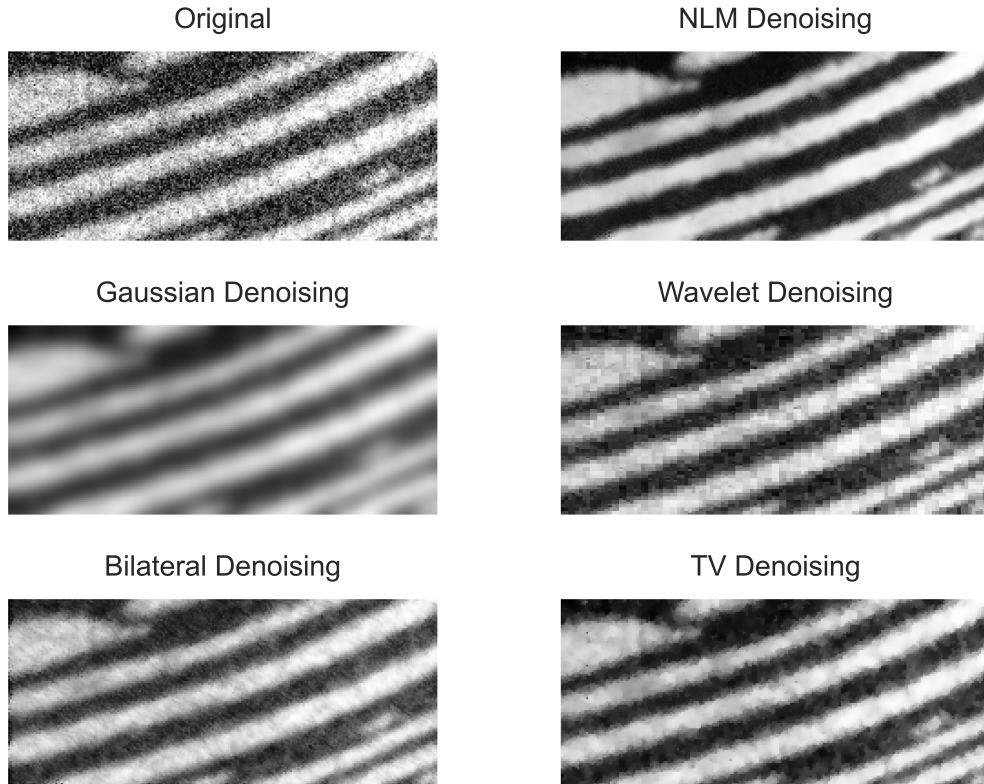


Figure 2.14: Effect of different denoising filters on an example noisy LEEM image.

Gaussian: Convolution with a Gaussian kernel. The only LTI filter from the examples. **Bilateral:** Averaging based on spacial closeness and intensity similarity. **NLM:** Averaging between local pixels with similar surrounding patches. **Wavelet:** Thresholding small values in wavelet domain and reconstructing. **Total Variation (TV):** Minimisation of the total variation of the image gradient through optimising algorithms. Note that all denoising was done using scikit-image, after CLAHE has been applied to the original image.

Thresholding

Image thresholding is a powerful tool when there is a profound contrast between the objects of interest and the rest of the image. It is a mandatory step in most

object detection and tracking methods, and is thus a necessary addition to the preprocessing toolbox. While manual thresholding is error prone and unfeasible for large and varied data, automatic thresholding is enabled by one of the most widely used thresholding methods, introduced by Otsu, 1979. Otsu's method outputs a value for the threshold, such that it minimises the variance between the intensities of the two groups of pixels it splits. This is expressed as:

$$\sigma_{\text{intra}}^2(t) = w_0(t)\sigma_0^2(t) + w_1(t)\sigma_1^2(t)$$

where t is the threshold value, $w_0(t)$ and $w_1(t)$ are the probabilities of the two classes, and $\sigma_0^2(t)$ and $\sigma_1^2(t)$ are the variances of the two classes. The goal of Otsu's method is to find the threshold value t^* that minimizes the intra-class variance:

$$t^* = \underset{0 \leq t \leq T}{\operatorname{argmin}}(\sigma_{\text{intra}}^2(t))$$

where T is the maximum gray-level value.

Once the threshold value t is determined, the image can be segmented into two classes: pixels with gray-level values less than or equal to t belong to one class, while pixels with gray-level values greater than t^* belong to the other class.

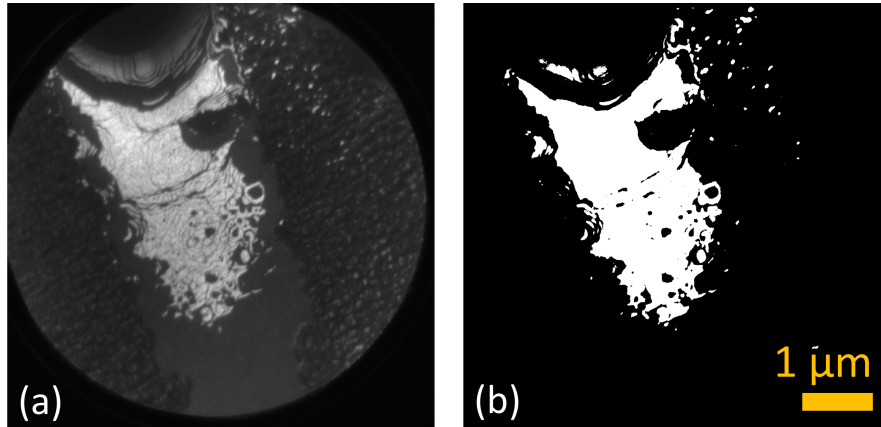


Figure 2.15: Otsu thresholding example in a LEEM image.

Gradient-based Detection

Gradient-based detection methods are a common technique in computer vision for detecting the edges in an image. These methods rely on computing the gradient of the image, which represents the rate of change of the pixel intensities. Edges in

an image correspond to areas of high gradient magnitude, where the pixel intensities change rapidly.

The most common gradient-based edge detection method is the Sobel operator, which applies a matrix derivative to both the horizontal and vertical directions of the image:

$$\text{horizontal} = \begin{bmatrix} -1 & 0 & 1 \\ -2 & 0 & 2 \\ -1 & 0 & 1 \end{bmatrix} \quad \text{vertical} = \begin{bmatrix} -1 & -2 & -1 \\ 0 & 0 & 0 \\ 1 & 2 & 1 \end{bmatrix}$$

The convolution with these two kernels over the image calculate its gradient in both the horizontal and vertical directions. The gradient magnitude at each pixel is then calculated as the Euclidean norm of the horizontal and vertical gradients. Pixels with high gradient magnitude are considered to be part of an edge.

This basic approach, like other gradient-based operators, provides good results in images with well-defined edges, but is susceptible to noise, which is why extra preprocessing steps, such as denoising can be useful. This is why the more sophisticated method of Canny edge detection has become a well-established algorithm, as it incorporates both a denoising step before the application of a Sobel operator, and edge connectivity checks after it, to facilitate a more robust detection (Canny, 1986).

2.3.2 Machine Learning and Deep Learning

Machine Learning (ML) is the part of the Artificial Intelligence field, which implements algorithms able to learn and improve based on data, without the need of explicit programming to complete a task. Deep Learning (DL) is a subset of ML, where artificial neural networks are used for the same purpose, but are generally larger and more computationally expensive to train. They are aimed at learning and making predictions on larger and more complex datasets. Here, we refer to the more traditional learning approaches, such as random forests, decision trees, gradient boosting methods and support vector machines as the ML approaches and we refer to algorithms and architectures based on Neural Networks as the DL approaches.

The progress in ML and DL methods in CV applications in the past decade has enabled significant advancements in Materials Science and microscopy (Ede,

2021a; Mueller et al., 2016; Ramprasad et al., 2017; von Chamier et al., 2021). The field's progress has allowed a plethora of data-driven applications in microscopy imaging, such as data cleaning (Koho et al., 2016; Yang et al., 2018), analysis of real space imaging and diffraction data (Aguiar et al., 2019; Xing et al., 2018), image segmentation (Akers et al., 2021; Yao et al., 2020) and process automation (Ivanov et al., 2020; Krull et al., 2020; Pinkard, 2019). ML and DL approaches usually bring great improvements in accuracy and performance over standard CV methods, and become indispensable when faced with a task that cannot be approached with analytical solutions or an intuitive rule set.

In such cases, the usage of DL algorithms in particular can be thought of as making a learned approximation to the solution function, which is defined as the unknown function that takes the input and calculates the correct output. In practice, when fed with data that describes an observed phenomenon in a large enough scope, DL algorithms are able to learn generalisations of the data and approximate the physical model that describes the phenomenon, based on the observed data. This is why extra care must be taken in preparing the data, as to not bring biases to the model and encompass as many variations of the observation as possible with balanced representation in the dataset. In essence, the quality of the data dictates the quality of the DL model.

Supervised and Unsupervised Learning

The learning approaches in ML and DL can be broadly classified into two types: supervised and unsupervised learning, depending on whether the training dataset comes labelled with the correct outputs for the task we want the algorithm to learn to predict.

Labelled datasets are needed for supervised problems such as classification, where the data needs to be categorised, or regression, where the correct output needs to be approximated in a non-discrete space. It is especially useful in microscopy imaging for tasks, where the data is simulated with known parameters, or is taken from examples that are well described and the variables are well controlled. Common examples of such tasks are identification of images and diffraction patterns, classification of particles, phases and structures.

On the other hand, in unsupervised learning, the algorithm is trained on an unlabelled dataset, where the correct output is not known. The algorithm learns to find patterns and structure in the data without any prior knowledge of what the output should be. Both the learned outputs of the algorithms and the found semantics in the data to achieve these outputs can be very useful. Common tasks in microscopy imaging that rely on unsupervised learning are image clustering for analysis, image segmentation, denoising and generation of microscopy imaging data.

Both ML and DL approaches are utilised in Chapter 5.

Machine Learning

Traditional ML approaches are powerful when used for relatively small, well-structured datasets where the relationships between the features and the target variable are well understood. They rely on feature engineering as a preprocessing step for the data before their training for best performance.

When approaching suitable tasks, it is common to test multiple algorithms and compare them based on their success. This is usually done through metrics such as *accuracy*, *f1-score* and *recall* for classification, or *mean absolute error* and *r2-score* in regression tasks. These metrics compare the outputs of algorithms to the expected outputs to measure their performance. Details on the most common metrics for model evaluation are given in Table 2.2.

The most commonly used algorithms for classification and regression tasks include Naive Bayes, k-Nearest Neighbours (kNN), Random Forests, Decision Trees, XGBoost and Support Vector Machines (SVM) with different kernels. The other important application of the traditional ML approaches is in clustering and manifold learning. These applications reveal relationships between data examples, based on the distances in a learnt space, where the data examples are represented by a point. Such algorithms include K-Means Clustering, SVMs, Gaussian Mixture Models and Density-Based Spatial Clustering of Applications with Noise (DBSCAN).

These traditional ML algorithms are cheap to train and can be easily implemented using popular machine learning libraries such as scikit-learn and PyTorch (Paszke et al., 2019).

Metric	Task	Description	Formula
Accuracy	Class.	Proportion of correct predictions out of total predictions	$\frac{TP+TN}{TP+TN+FP+FN}$
Precision	Class.	Proportion of true positives out of predicted positives	$\frac{TP}{TP+FP}$
Recall	Class.	Proportion of true positives out of actual positives	$\frac{TP}{TP+FN}$
F1-score	Class.	Harmonic mean of precision and recall	$2 \cdot \frac{TP}{2TP+FP+FN}$
MAE	Reg.	Average absolute difference between predicted and actual values	$\frac{1}{n} \sum_{i=1}^n y_i - \hat{y}_i $
MSE	Reg.	Average squared difference between predicted and actual values	$\frac{1}{n} \sum_{i=1}^n (y_i - \hat{y}_i)^2$
R2-score	Reg.	Proportion of variance in the target variable explained by the model	$1 - \frac{\sum_{i=1}^n (y_i - \hat{y}_i)^2}{\sum_{i=1}^n (y_i - \bar{y})^2}$
ROC AUC	Class.	Performance of binary classifier at different thresholds	Area under ROC curve

Table 2.2: Common metrics for evaluating classification and regression models. **R2-score** is also known as the Coefficient of Determination and **ROC AUC** computes the Area Under the Receiver Operating Characteristic (ROC) Curve.

Deep Learning

DL approaches involve the construction of Neural Network (NN) models, which are suitable for dealing with vast amounts of data with large complexity and variability. Their application in the field of CV is particularly strong, and has led to a significant amount of innovation in microscopy imaging (Ede, 2021b). DL methods are capable of ingesting data without particular need for preprocessing and feature engineering steps, although image augmentation as a preprocessing step has been shown to be very beneficial, especially when working on relatively small datasets (Shorten & Khoshgoftaar, 2019).

Different NN model architectures are designed to deal with specific tasks, such as

image classification, segmentation, reconstruction or generation. The networks are constructed by stacking layers with different sizes and functionalities and controlling the flow of data between them. Most of the layers contain parameters, which are adjusted during the training process, enabling the model's learning. The networks can be built using Python frameworks, such as PyTorch and Tensorflow (Abadi et al., 2016).

Here, we describe the common ideas and most widely used building blocks of NN models in the context of CV and microscopy imaging applications and their importance for model performance.

Key concepts in the training process. The aim of the training process is to adjust the weights of the network to minimise the difference between the network's predicted outputs and the expected outputs, given the set of training data. The difference between the predicted and expected outputs is defined through the *loss function*. The loss function quantifies how well the model is performing on a specific task, and the goal of the training process is to minimise the loss by adjusting the model's parameters with *optimisation algorithms*, such as the Adam Optimiser (Kingma & Ba, 2015).

The key process used to apply changes to the model parameters is *backpropagation*. It works by calculating the error at the output layer of the network and then propagating that error backwards through the network, layer by layer, to adjust the weights. The adjustment is computed through *gradient descent*, which uses the gradient of the loss with respect to the weights. The weights in the network are then updated in the opposite direction of the gradient. This is an iterative process, which happens over many steps and many iterations of the data, called *epochs*, until the training loss is minimised.

To ensure the model has been trained well, it is crucial to check the trained model's performance on testing data that it has not seen during its training. Under-performance on such data, compared to the model's performance during training can indicate *overfitting*. This usually happens when the model's size is too large, compared to the dataset, which allows the network to simply learn the different examples it is presented with during training 'by heart', resulting in poor generalisation of the data and low performance on unseen examples.

The neural layers. Almost all the learning during the NN model’s training happens in layers of neurons, which contain almost all of the model’s learning parameters. Neurons are nodes in layers, through which the data flows and computations are made. Neurons contain weights, usually for each input they receive, which are adjusted during training to optimise the outputs of the model.

The simplest such layer is the Fully Connected (FC) layer, also known as the dense layer. In this type of layer, all neurons in the previous layer are connected to every neuron in the current layer. This means that each neuron in the current layer receives input from every neuron in the previous layer, and outputs a single value to be passed to the next layer.

In the heart of models trained for image processing tasks, convolutional layers are commonly used instead of the FC layers. Convolutional layers apply a set of filters by means of their kernels, which contain the trainable parameters. The kernels are applied over the images with dot products and are able to extract sets of *feature maps* from them, which have been trained to contain features of interest for the specific task during model training. When constructing models, we are able to adjust hyperparameters, such as the number of filters, size of the kernels and kernel stride for each convolutional layer.

Non-linear activation functions. A non-linear activation function is usually added as a layer before each pass onto a learning layer. It allows the network to learn complex and non-linear relationships between inputs and outputs, which is often necessary in CV and microscopy applications where the data can be highly complex and non-linear. Without non-linear activation functions, a neural network would essentially be reduced to a linear model, which would severely limit its ability to model complex patterns in the data. Therefore, non-linear activation functions such as exponential linear unit (ELU), rectified linear unit (ReLU), leaky rectified linear unit (LeakyReLU), sigmoid, and tanh are commonly used in deep learning architectures to introduce non-linearity and improve model performance. Their equations and shapes are shown in Table 2.3. Modern approaches also include trainable activation functions (Apicella et al., 2021).

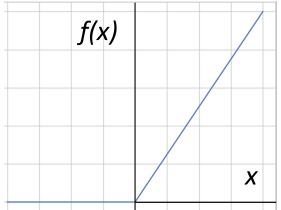
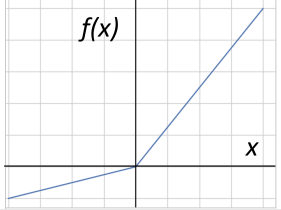
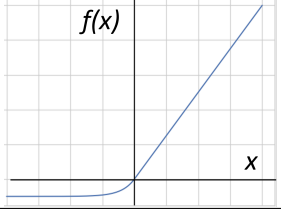
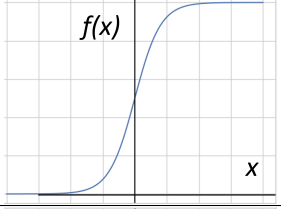
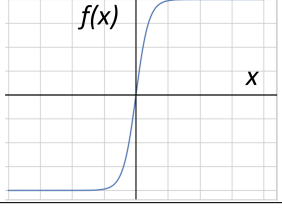
Activation Function	Formula	Graph
ReLU	$f(x) = \max(0, x)$	
Leaky ReLU	$f(x) = \begin{cases} x, & x \geq 0 \\ \alpha x, & x < 0 \end{cases}$	
ELU	$f(x) = \begin{cases} x, & x \geq 0 \\ \alpha(e^x - 1), & x < 0 \end{cases}$	
Sigmoid	$f(x) = \frac{1}{1 + e^{-x}}$	
Tanh	$f(x) = \frac{e^x - e^{-x}}{e^x + e^{-x}}$	

Table 2.3: Common activation functions with their formulas and graph shapes.

Normalisation. Normalisation keeps the data in a defined range of values throughout its pass in the model. It is a necessary step to ensure that data values do not grow out of control and remain in the range, where they can be easily manipulated by the layer weights and the non-linear activation functions. The most common approach in CV applications is the usage of Batch Normalisation, which performs its normalisation over the entire batch of data that passes through the model at each training step or model inference (Ioffe & Szegedy, 2015). It contains learnable parameters, which adapt to the data. The mathematical formulation of Batch Normalisation is:

$$\text{BatchNorm}(x_i) = \frac{x_i - E(x)}{\sqrt{\text{Var}(x) + \epsilon}} \gamma + \beta$$

where x_i represents the i -th input to the Batch Normalisation layer, $E(x)$ is the mean of the batch of inputs, $\text{Var}(x)$ is the variance of the batch of inputs, γ and β are learnable parameters that scale and shift the normalised inputs, respectively, and ϵ is a small constant added to the variance to prevent division by zero. This is applied to all channels of images simultaneously, with separate learnable parameters.

Architectural Patterns. These basic building blocks for neural networks are layered together to create DL models. Different DL architectures can be engineered for various purposes through modifications in the stacked structures, layer sizes and the way the data flows through these layers and structures. Here, we overview some of the most impactful architectures for CV tasks, which can be very useful in the context of microscopy imaging.

Using DL for image classification involves one of the most basic architectures - the Convolutional Neural Network (CNN) (Alex et al., 2012). The network involves stacking building blocks, constructed of a convolutional layer, a normalisation layer and an activation function layer, as shown in Figure 2.16. The building blocks can

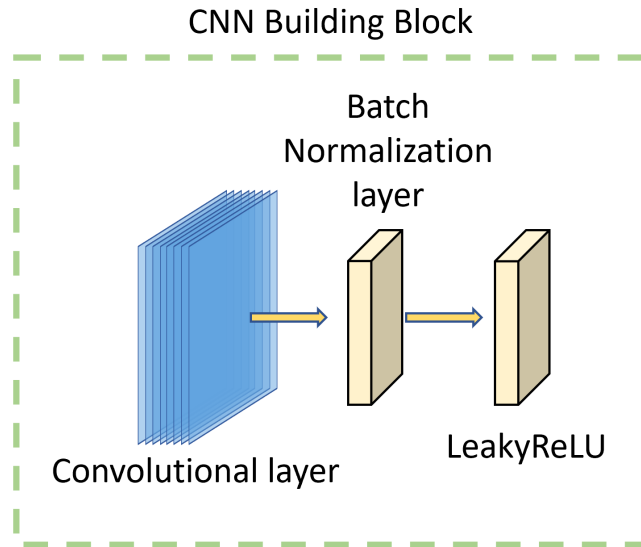


Figure 2.16: A common CNN building block, consisting of a convolutional layer, a normalisation layer and an activation layer. The convolutional layer carries tunable hyperparameters, such as its *kernel size*, *stride* and *padding type*.

also include MaxPooling or MeanPooling layers for downsampling - the reduction of dimensions as the images flow through the network. The data flows directly through all the layers and results in an array of numbers with the length of the number of

classes in the task, as shown in Figure 2.17. The model training has the objective of predicting the image classes through its output of numbers.

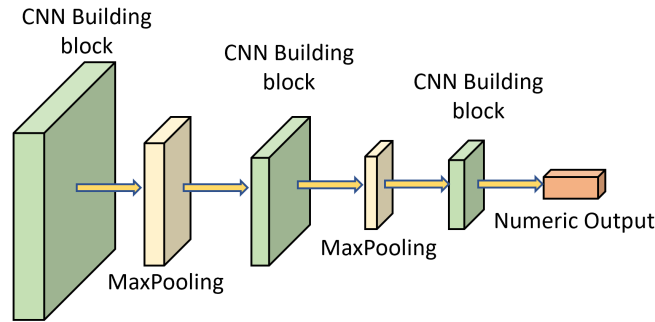


Figure 2.17: A general CNN architecture. It uses MaxPooling layers to gradually reduce image dimensions to suit the final output dimensions for its classification or regression purpose.

By setting the layer sizes in a specific way, we can take the CNN architecture and create an Autoencoder (AE) architecture. The AE architecture forces the images to squeeze through a very small bottleneck dimension, called the latent space, and then get reconstructed back, with the objective of recreating the original image, as shown in Figure 2.18. This pushes the algorithm towards learning a generalisation of the dataset in its latent space. With that, the algorithm learns the most important features of the images and is capable of removing features that are not consistent, such as noise. For that reason, AE networks are powerful in denoising applications and anomaly detection, but the learnt data generalisation in the latent space can also be utilised for unsupervised data analysis. This is what is used in Chapter 5.

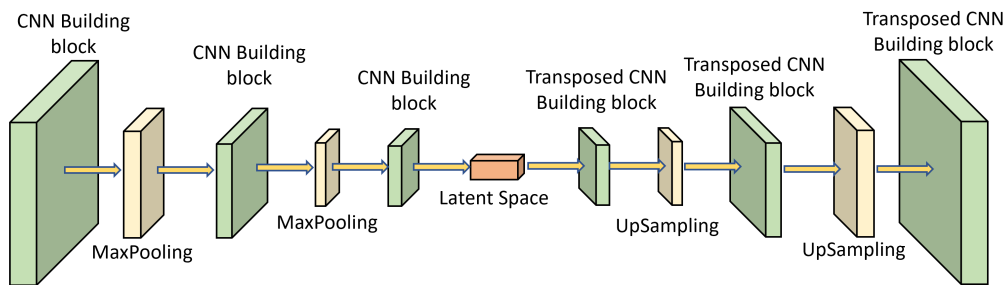


Figure 2.18: A general AE network. It reduces the dimensions of the image to a bottleneck in the latent space, and then expands them back to the original dimensions.

A milestone architecture, the Residual Neural Network (ResNet) (He et al., 2015), is reached by taking the CNN network and modifying the flow of data. It adds the idea of skip connections - an extra channel in a building block that duplicates the image and 'skips' the network layers to merges back at the end of the

building block, as shown in Figure 2.19. This results in the identity of the image being preserved, and the network learning not to map the image entirely for its task, but to add residual mapping on top of it. ResNet networks enable very deep networks and are used in very large models. They are mainly used for classification tasks.

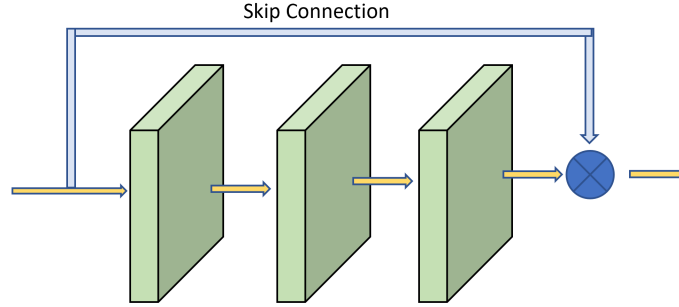


Figure 2.19: A general ResNet architecture. It uses a skip connection to enable a data flow outside the stacked CNN building blocks.

One of the most impactful architectures for image segmentation, the U-Net (Ronneberger et al., 2015), combines the idea of skip connections with the AE architecture. U-Net downsamples the input image through a series of convolutional and pooling layers, and then upsamples the resulting feature map through a series of transposed convolutional layers, as shown in Figure 2.20. The final output of the network is a binary mask that indicates the presence or absence of the target features in each pixel of the input image. It can be used to identify structures or features of interest, such as particles or defects.

Other impactful applications lie in image generation, which we do not expand on here for brevity. There, different types of Generative Adversarial Networks (GANs) (Goodfellow et al., 2014) and Diffusion models (Sohl-Dickstein et al., 2015) can be used in applications such as expanding datasets with synthetic images.

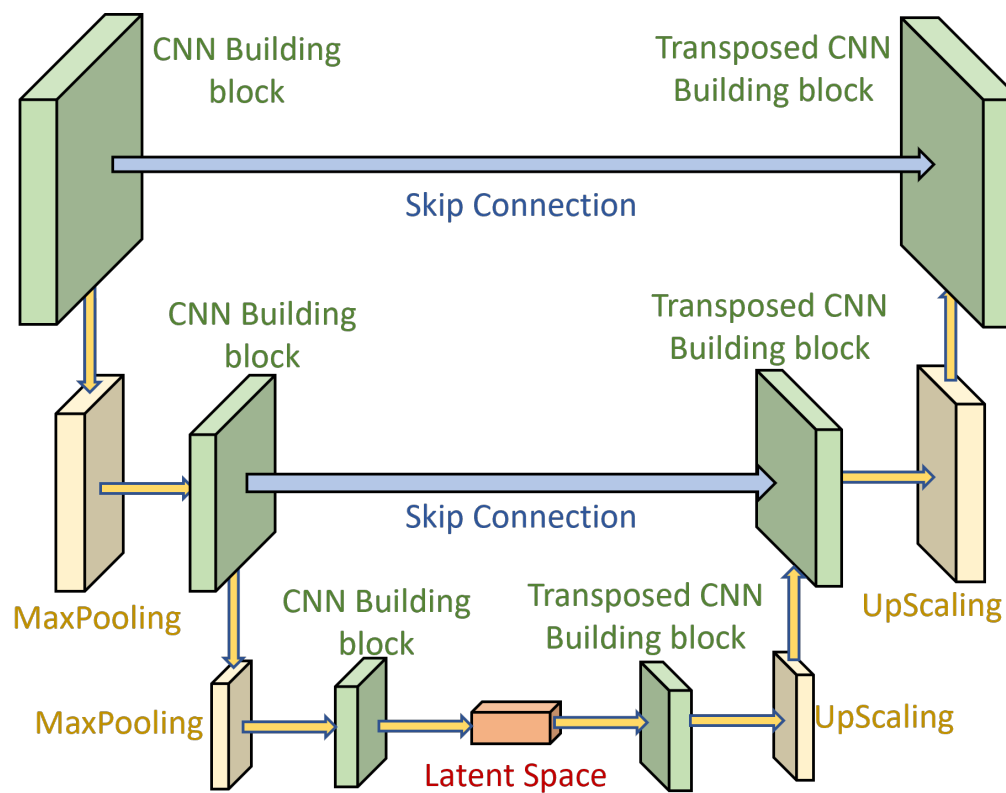


Figure 2.20: A general UNET architecture. It uses the skip connections idea to preserve the identity of the data.

Chapter 3

Measuring entropy difference through phase coexistence monitoring with LEEM

3.1 Introduction

Entropy is a key thermodynamic property of the semiconductor surface that governs much of the surface phase behaviour. Its contribution to surface energetics can be a valuable consideration in theoretical surface models, but measuring entropy differences between phases experimentally is elusive and the parameter is usually neglected. In this work, we show that in the context of a first-order phase transition, this can be achieved through three sets of measurements within a single experiment using Low-Energy Electron Microscopy (LEEM). LEEM microscopy has been established as one of the most effective methods for the detection of phase coexistence (Teliëps & Bauer, [1985](#), [1986](#)) and its ability to observe surface dynamics in real-time with great precision allows the measurements of the phase coverage and boundary fluctuations, which can then be analysed with the methods reviewed by Hannon and Tromp, [2003](#).

The understanding and control of the GaAs(001) semiconductor surface structure is a crucial factor in maintaining the high quality of epitaxial growth for the high-precision fabrication of heterostructures for optoelectronic devices (Ibach, [1997](#); Joyce & Vvedensky, [2004](#); Krzyzewski & Jones, [2008](#); Ohtake et al., [2013](#); Ohtake

et al., 2014; Orton & Foxon, 2015; Yasuda et al., 2008). As a result, the structure, defined by its surface phases, has been extensively studied and considerable understanding of the behaviour and underlying processes has been reached (LaBella et al., 2005; Ohtake, 2008; Pristovsek et al., 2003). A significant part of that behaviour, especially during some phase transitions, is the possibility of having multiple surface phases simultaneously. This phase coexistence phenomenon can be successfully accounted for by the energetics of long-range elastic and electrostatic interactions and its stability is largely governed by two fundamental parameters - the stress difference and the entropy difference between the two phases (Hannon et al., 2001). The elastic and electrostatic interactions, which are dependent on the surface phase coverage, give access to the entropy difference. The stress difference manifests itself through the stiffness of the boundaries between the two coexisting phases and so it is found by closely monitoring the boundary fluctuations (Alfonso et al., 1992; N. C. Bartelt et al., 1992). A description of the theory behind these interactions is outlined in Chapter 2.1.1.

We bring together methods in LEEM imaging and analysis and demonstrate their ability to obtain fundamental surface parameters of a compound semiconductor independently and without the need for external characterization. We develop a modular computational algorithm to automate the analysis process, making the method easily applicable to most semiconductor and metallic surfaces.

3.2 The stability of the (6×6)

Our experimental observations focus on the stable phase coexistence between the (6×6) and the $c(8 \times 2)$ as we aim to settle the ongoing debate about the stability of the (6×6) phase. Multiple (6×6) geometries have been determined through theoretical calculations, but were shown to not be stable (Ohtake, 2007; Pristovsek et al., 2003; Seino et al., 2006). These geometries are found through density Functional Theory (DFT) calculations - the main tool for theoretically describing the energetics of a surface reconstruction. In GaAs(001), it is used to derive the zero temperature formation free energies of different structures and to plot them against the Gallium chemical potential μ_{Ga} to get a phase diagram for its surface. With this approach,

many models for the (6×6) have been proposed, such as Kuball (Kuball et al., 1995), McLean (McLean et al., 1999), Xu (H. Xu et al., 2002) and Kocan (Kocán et al., 2004), but all of them suggest a high formation energy, making them inaccessible on a real GaAs(001) surface. The likeliest candidate out of them is the Kocan model, as it possesses the lowest free energy. To make that model more accessible, modifications were also proposed, adjusting the proportions of As-As dimers, resulting in the most likely candidate for the (6×6) structure so far - a (12×6) -sized unit cell (Seino et al., 2006). However, this optimal structure is still not stable at any chemical potential value, suggesting a $\beta 2(2 \times 4) \rightarrow c(8 \times 2)$ phase transition sequence. By contrast, experiments show a $\beta 2(2 \times 4) \rightarrow (3 \times 6) \rightarrow (6 \times 6) \rightarrow c(8 \times 2)$ transition.

Despite the predicted instability multiple surface structures and compositions of the phase were experimentally observed using Scanning Tunneling Microscopy (STM) measurements (Ohtake, 2007). LEEM microscopy was recently used to observe that the (6×6) phase manifests itself on the GaAs(001) surface through three separate regimes, depending on the experimental conditions. In its low-temperature regime, it can indeed be stable within a very narrow window and cover most of the surface area, as observed through control over the chemical potential under As flux (Zheng et al., 2019). In its high-temperature regime, where the surface is mostly covered by the $c(8 \times 2)$ phase, the (6×6) enters a state of metastability, with patches appearing and disappearing dynamically (Hannikainen et al., 2019). In between the two regimes lies a broad $(6 \times 6) \leftrightarrow c(8 \times 2)$ transition, where a stable coexistence between the two phases is observed under a large spectrum of temperatures during the transition (Niu et al., 2019; Zheng, Tersoff, et al., 2016). These observations contradict surface energy calculations, which exclude the (6×6) from the sequence of phase transitions altogether. It was suggested that since calculations are done at $T = 0$ K, the entropy difference at non-zero temperatures could be responsible for the stabilization of the otherwise unfavourable (6×6) phase (Zheng et al., 2019).

We show that with the unified method, we are able to fill this gap between theory and experiment, as we explore the (6×6) phase and gain valuable insights from its coexistence with the $c(8 \times 2)$.

3.3 Experimental details

3.3.1 Experimental setup

Experiments were performed using the Elmitec LEEM-III microscope. Using very low energy electrons ($0 - 15\text{eV}$) makes the LEEM highly sensitive to the structure of the crystal surface, allowing real-time non-scanning in-situ observation of the processes occurring on a crystal surface under a variety of conditions, with high lateral resolution (Bauer, 2014). A GaAs(001) sample is placed under Ultra-High Vacuum (UHV) of around 2×10^{-10} Torr, its surface is initially prepared by annealing for 2 h at 580°C . Gallium droplets of up to $5\text{ }\mu\text{m}$ in diameter are then produced at 620°C and allowed to run on the surface, creating flat regions of at least $15\text{ }\mu\text{m}$ length (Tersoff et al., 2009; Zheng, Tang, et al., 2016). After the atomically flat surface is created, the droplets are slowly evaporated at temperatures of around 530°C . The sample is then brought up to 550°C , which is in the middle of the temperature region where both the $c(8 \times 2)$ and the (6×6) phases can be found (Zheng, Tersoff, et al., 2016). The forming domains are always monitored and maintained for enough time to ensure equilibrium before an experiment is conducted. The phases are confirmed by observing the low-energy electron diffraction patterns at select small surface patches (μLEED) and the discrimination of phases can be further enhanced by utilising the high contrast between phases using Selected Energy Dark Field Low-Energy Electron Microscopy (SEDFLEEM), as described by (Niu et al., 2019), with the consequence of a lower overall image intensity.

3.3.2 Experimental design

The full experiment is split into two main procedures - the first one focuses on the larger scale coverage, while the other focuses on small-scale dynamics of boundary fluctuations. A supplementary measurement is necessary in order to quantify the specific electrostatic interactions in the system.

Coverage measurements

First, experiments are done to determine the behaviour of the coverage against varying temperature. The measurements are done by changing the temperature

in small steps between 500 °C and 620 °C and monitoring the phase transition between the $c(8\times 2)$ and the (6×6) phases. Each temperature was held for 2 hours to ensure stability. Figure 3.1 shows the variation in coverage for the full range of temperatures and the corresponding images at chosen temperatures during the experiment. At higher temperatures, up to 620 °C, the $c(8\times 2)$ dominates the surface, with the (6×6) becoming unstable above 580 °C, entering a state of metastability (Hannikainen et al., 2019). At 550 °C, the coverage of $c(8\times 2)$ and (6×6) equalises, and at lower temperatures, between 550 °C and 500 °C, the (6×6) covers the majority of the surface. The patterns are proven to be thermodynamically stable, retaining a constant coverage during observations for a period of 3-4 hours. The reversibility of the process is verified by repeating the same procedure for both heating and cooling down the surface, where some hysteresis was observed. The observations indicate that the transition between the (6×6) and the $c(8\times 2)$ phases is first-order, as the contrasting areas in the images show that the boundaries between the (6×6) and $c(8\times 2)$ patches are sharp.

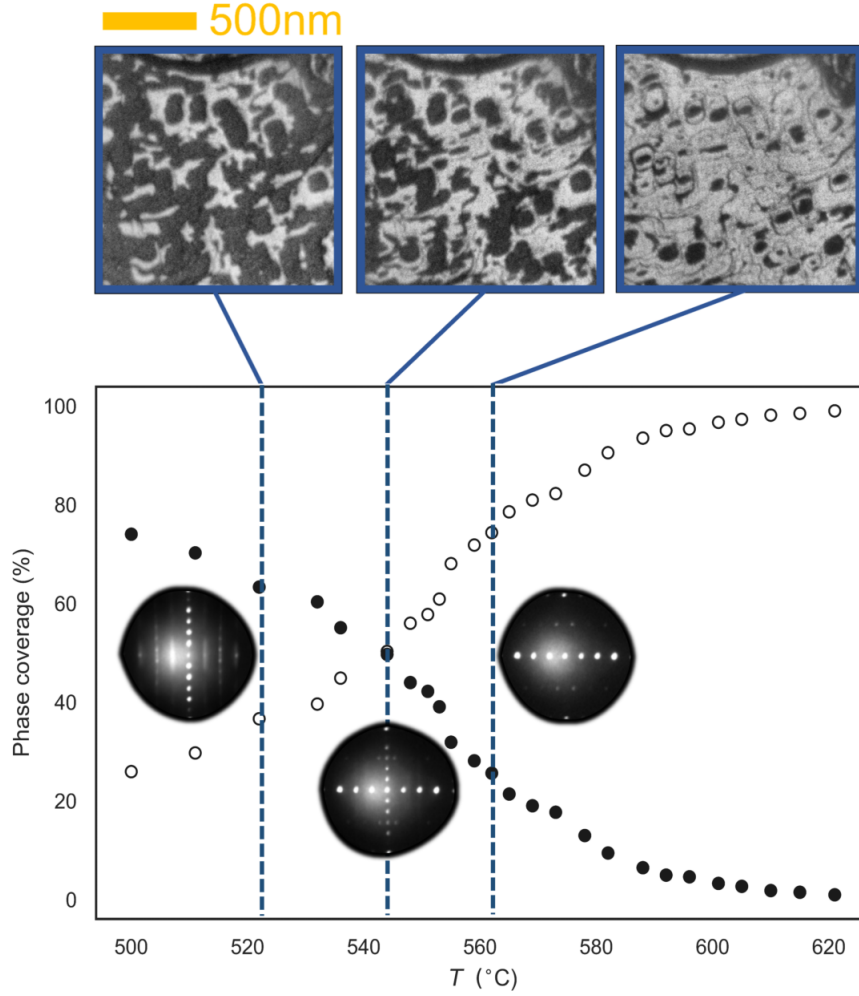


Figure 3.1: A diagram of the full coverage variation between the $c(8 \times 2)$ (white dots) and (6×6) (black dots) phases with temperature. LEEM images of the dark (6×6) domains and the bright $c(8 \times 2)$ domains are shown at the corresponding temperatures. The images show how the coverage of the (6×6) decreases as the temperature is increased. Low-Energy Electron Diffraction (LEED) images show the diffraction patterns at the temperature regions with different coverage proportions of the two phases. The diffraction pattern in the middle of the range, at around equal coverage, is a mixture of the (6×6) and the $c(8 \times 2)$ patterns in the low and high temperature range, respectively.

Fluctuations measurements

Fluctuation monitoring experiments are done with the temperature set to 550°C , where the coexistence between the (6×6) and $c(8 \times 2)$ phases is at about equal coverage. The surface is allowed to stabilise and selected suitable regions are imaged for 3 – 6 minutes each. With these conditions, imaging was done with frame rates of between 15fps and 20fps with sufficient signal-to-noise ratio and a lateral resolu-

tion of about 10 nm. Fluctuations detection and processing was designed in such a way as to accommodate different boundary sizes and shapes, and to work well in a variety of imaging conditions. This extends the application of the method to materials that do not necessarily exhibit a particular structural order in their steps and boundaries, just like the GaAs(001) surface examined in this work. The algorithm's process of detecting boundaries is shown in Figure 3.2 and the process of converting the boundaries to fluctuations data is visualised in Figure 3.3. The detection process starts with the boundaries marked by the user and isolated (Figure 3.2 step 0.). After that, the following methods, corresponding to the illustrated steps, are applied to each video frame, as illustrated in Figure 3.2:

1. **Normalisation:** The selections are normalised linearly or through Contrast Limited Adaptive Histogram Equalization (CLAHE) (Pizer et al., 1987), depending on intensity gradients and noise levels in the image section.
2. **Bilateral Denoising:** A non-linear edge-preserving denoising method is applied to filter noise without destroying small features (Jain & Tyagi, 2016; Tomasi & Manduchi, 1998).
3. **Canny-Devernay Detection:** A sub-pixel variant of the powerful and stable Canny edge detection is applied, giving the boundary positions for each video frame with sub-pixel accuracy (Canny, 1986; Devernay, 1995). The size of each pixel is equivalent to 6 nm.

In total, about 15500 video frames were analysed, producing sets of coordinates for 10 boundaries. Figure 3.3(a.1) shows the area of the selected boundary for which the boundary coordinates were gathered and Figure 3.3(a.2) gives an example of the edge detection for the whole area. The precise detection for each frame is shown in Figure 3.3. The detected boundary from the first frame of the LEEM video is used to construct perpendiculars which adapt to boundary's general shape, allowing for boundaries of arbitrary shapes to be analysed without additional bias Figure 3.3(b.1). The constructed perpendiculars, shown in full in Figure 3.3(b.2), are the reference frame to which all detected points are aligned. The detection points from the Canny-Devernay algorithm are projected onto the reference frame by finding the crossing points with the perpendiculars using WENO interpolation

(Janett et al., 2019). Figure 3.3(c.1) shows how the detected boundary around an example perpendicular from the reference frame is interpolated and crossed with the perpendicular to produce a data point. The image intensity profile along that perpendicular is shown in Figure 3.3(c.2) at the example detected point position, demonstrating the positional accuracy of the detection. In total, over 3.1 million data points were analysed with this method. The algorithm's final output is the distance offset of each detection with respect to the average position over the whole experiment, as detected in every image of the video by the initially constructed frame of reference.

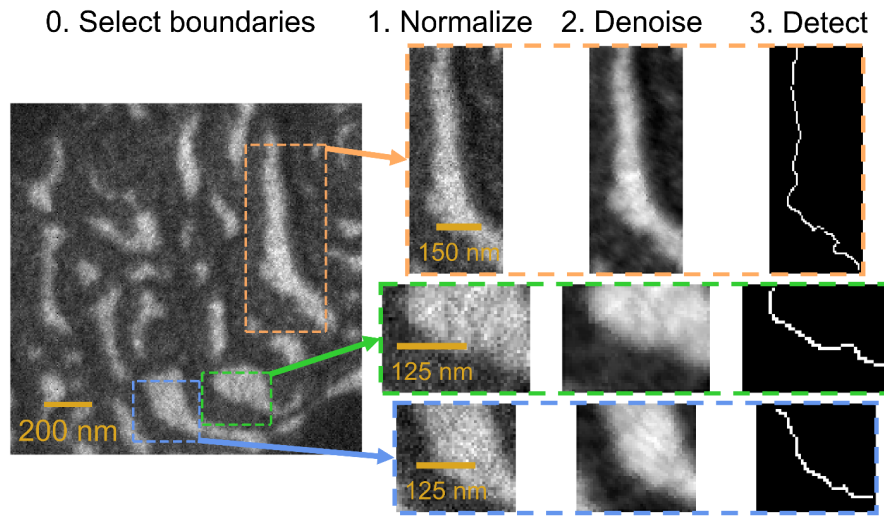


Figure 3.2: The process of extracting boundary coordinates from raw images through edge detection.

The coverage experiments were done in Dark Field (DF), by switching between the $(1/4, 0)$ spot with an electron beam energy of 6.2 eV to observe the $c(8 \times 2)$, and the $(3/6, 0)$ spot of the (6×6) at an energy of 7.8 eV. The fluctuations experiments were all done in Bright Field (BF) at 8.5 eV electron beam energy.

Work function measurements

The work function difference between the (6×6) and $c(8 \times 2)$ phases was measured by varying the Start Voltage to change the incident electron energy from -1.5 eV to 2.5 eV. By using the transition between mirror-mode and LEEM-mode in the microscope imaging of each phase, as shown by Yim et al., 2008, the energies corresponding to the largest intensity variation is found for both phases, the differ-

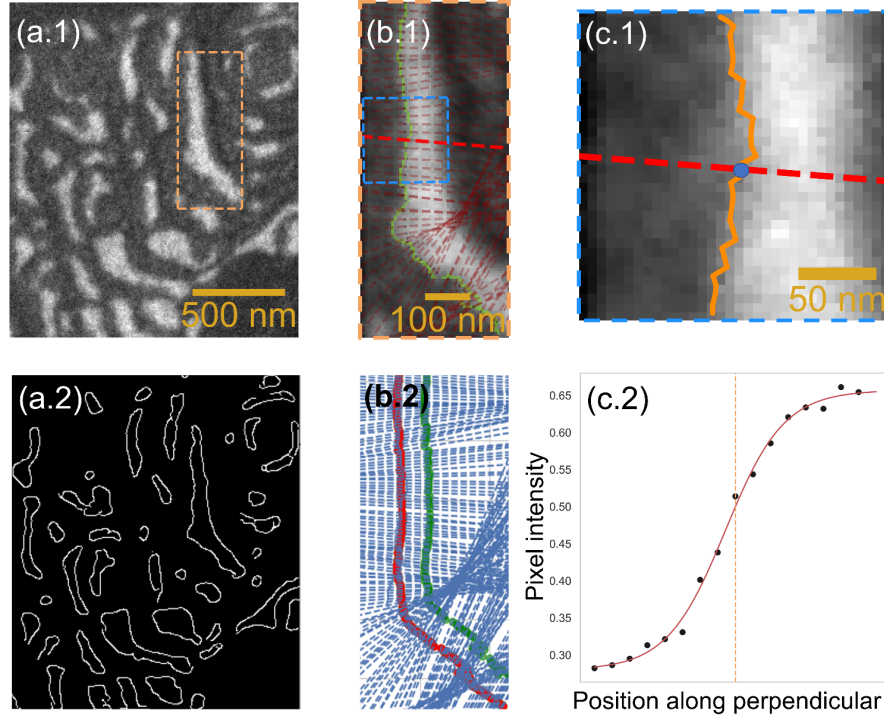


Figure 3.3: The logical steps of the algorithm for converting the detected boundary coordinates to fluctuations (offsets).

ence of which gives the work function difference, in eV. It is found that the work function difference has an insignificantly small contribution to the results, compared to contributions from elastic interactions.

3.4 Results

In order to explore the coexistence during the transition, we perform analysis over two complementary steps - analysis of the phase coverage and analysis of the phase boundaries, as demonstrated by Hannon and Tromp, 2003.

3.4.1 Phase Coverage

Phase coexistence occurs when the energy gain from creating and subsequently maintaining an unfavourable phase and its boundaries is compensated by the elastic and electrostatic interactions at those phase boundaries, which allow local relax-

ation. The total surface energy per unit area is (Hannon et al., 2001):

$$E_{total}/A^2 = \frac{C_b}{L_b} + p \frac{\Delta S(T - T_0)}{2} - \frac{2C_m}{L_b} \ln \left(\frac{L_b}{\pi a} \cos \left(\frac{p\pi}{2} \right) \right) + \frac{C_d}{L_b^2} \tan \left(\frac{p\pi}{2} \right) - \frac{8C_r}{L_b^3} \left(\frac{1}{(1+p)^2} + \frac{1}{(1-p)^2} \right) \quad (3.1)$$

This is an extended version of Equation 2.1, derived in 2.1.1, with added higher-order interactions that do not impact the final results. Here, $p = (2\frac{A_{(6 \times 6)}}{A_{total}} - 1)$ is the surface coverage parameter. It is defined with the areas of (6×6) and $c(8 \times 2)$ coverage, such that it expresses the asymmetry between the two phases. It varies from $p = -1$ for full $c(8 \times 2)$ coverage to $p = 1$ for full (6×6) coverage. $T_0 \approx 550^\circ\text{C}$ is the temperature where the two phases have equal coverage, ΔS is the difference in entropy between the phases and L_b is the distance between steps, or terrace width. This expression can then be minimised with respect to the coverage, $\partial E/\partial p = 0$, to give a dependence between coverage and temperature.

$$T - T_0 = - \left(\frac{2}{\Delta S} \right) \left[\frac{\pi C_m}{L_b} \tan \left(\frac{p\pi}{2} \right) + \frac{\pi C_d}{2L_b^2} \cos^{-2} \left(\frac{p\pi}{2} \right) + \frac{16C_r}{L_b^3} \left(\frac{1}{(1+p)^3} - \frac{1}{(1-p)^3} \right) \right] + const \quad (3.2)$$

A fitting of the experimental data is shown in Figure 3.4 and yields the constants in Equation 3.1. The C_0 term accounting for the boundary creation energy costs vanishes with the differentiation. From the fit, the value of the constant representing the elastic and electrostatic interactions at the phase boundaries is $C_m = (6.44 \pm 1.39) \text{ meV } \text{\AA}^{-1}$, the interaction between boundaries and steps - $C_d = (8.65 \pm 0.98) \text{ eV}$, the short-range boundary-boundary interactions - $C_r = (57.78 \pm 0.15) \text{ eV } \text{\AA}$, and the difference in entropy is $\Delta S = (7.21 \pm 1.55) \times 10^{-4} \text{ meV K}^{-1} \text{\AA}^{-2}$. To estimate the values of the C_d and C_r parameters more accurately, the fitted values of C_m and ΔS are bound to within an order of magnitude of the values derived in the fluctuations analysis.

The higher order interaction terms C_d and C_r have a negligible contribution at the regions of equal coverage $p \approx 0$ (Hannon et al., 2001), giving a linear dependence:

$$\tan \left(\frac{p\pi}{2} \right) \approx - \frac{L_b \Delta S}{2\pi C_m} (T - T_0) \quad (3.3)$$

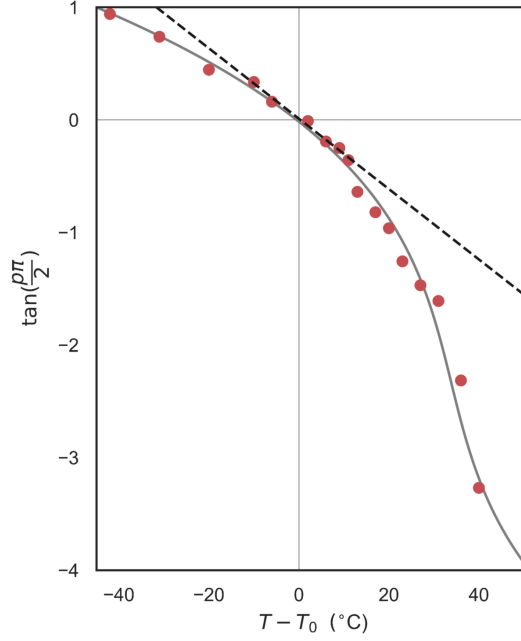


Figure 3.4: Experimental results (red dots) of dependence of $\tan(\frac{p\pi}{2})$ on the temperature T . The gray curve is a fit from the minimisation of Equation 3.1 and the dashed linear fit represents the linear dependence expected at around equal coverage (Equation 3.4). The slope of the fit is $(-0.031 \pm 0.002) \text{ K}^{-1}$ and gives us the result in Equation 3.4.

As can be seen in the linear fit shown in Figure 3.4, experimental data agrees with the linear behaviour indicated by Equation 3.3 around equal coverage. This is a strong indication that the elastic relaxation at the boundaries is the most important interaction that contributes towards the observed coexistence (Hannon & Tromp, 2003). The linear fit yields a relation between the entropy difference ΔS and C_m , which can be used to calculate the entropy difference (Hannon et al., 2001). Given the terrace sizes on the GaAs(001) surface where measurements were made during the experiment are $L_b = (185 \pm 13) \text{ nm}$, the slope corresponds to:

$$\frac{\Delta S}{C_m} = (1.06 \pm 0.20) \times 10^{-4} \text{ K}^{-1} \text{ \AA}^{-1} \quad (3.4)$$

3.4.2 Boundary fluctuations

The value of C_m can be obtained by analysing the boundary fluctuations between the two phases in the coexistence. In Equation 3.4, C_m is the sum of the contributions from electrostatic interactions,

$$C_\phi = \frac{(\Delta\phi)^2}{8\pi^2} \quad (3.5)$$

in electrostatic units (Vanderbilt, 1992), coming from the work function difference $\Delta\phi$ between the two phases, and elastic interactions,

$$C_\lambda = (\Delta\lambda)^2 \frac{(1 - \nu^2)}{\pi\Upsilon} \quad (3.6)$$

arising from the stress difference $\Delta\lambda$ between the two phases. Here $\nu = 0.31$ is Poisson's ratio and $\Upsilon = 0.53 \text{ eV}/\text{\AA}^3$ is Young's modulus. The origin of these two constants is described in Chapter 2.1.1 - see the derivations of Equations 2.10 and 2.7. The difference in work functions between the two phases can be found experimentally, as outlined in Section 3.3.2, giving $\Delta\phi = 0.1 \text{ eV}$. This results in an electrostatic interaction constant of $C_\phi = 0.01 \text{ meV } \text{\AA}^{-1}$.

The stress difference $\Delta\lambda$ is found through measurements of the phase boundary fluctuations (N. Bartelt et al., 1996; Hannon & Tromp, 2001) at the temperature of equal coverage $T_0 = 550^\circ\text{C}$. The phase boundary fluctuations are closely imaged at 15 fps for about 4 min and processed as shown in Figures 3.2 and 3.3. These imaging conditions push the LEEM to the limits of its temporal and spatial resolution capabilities.

The boundary fluctuations are defined as the offsets $y(x, t)$ of each point x along the boundary for a unit time t . In practice, that is the measured point offset for each image frame, with respect to its average position over all frames. These measurements are first used to find the boundary stiffness β . Through the Fourier transformation in the form:

$$y_q(t) = \frac{1}{N} \sum_q y(x, t) \exp(-iqx) \quad (3.7)$$

the Fourier components can be analysed. The mean squared Fourier components of the deflections $\langle |y_q|^2 \rangle$ can be expressed through Equation 2.17:

$$\langle |y_q|^2 \rangle = \frac{k_B T}{L_b \beta q^2} \quad (3.8)$$

, where k_B is the Boltzmann constant, L_b is the length of the explored boundary and $q = 2\pi n/L_b$, where $n = 1, 2, \dots, N$. This gives a linear relationship between $\langle |y_q|^2 \rangle^{-1}$ and q^2 . The linear fit to the data, using Equation 3.8 as shown in Figure 3.5(a), gives a boundary stiffness of $\beta = (28.3 \pm 11.0) \text{ meV nm}^{-1}$. The linearity of the experimental data, when adapted for Equation 3.8, is an indication of how independent the fluctuations of each analysed boundary are.

The boundary stiffness is used to find C_λ using the probability distribution of the phase boundary deflections Δx , shown in Figure 3.5(b). The standard deviation of the Gaussian fit to the data corresponds to the expected distribution, given by Equation 2.23:

$$\sigma^2 = \frac{k_B T L_b}{2\pi(2\beta C_\lambda)^{\frac{1}{2}}} \quad (3.9)$$

From Equation 3.9, the value of the elastic contributions constant becomes $C_\lambda = (9.75 \pm 6.06) \text{ meV } \text{\AA}^{-1}$. Using Equation 3.6, we are then able to find the stress difference $\Delta\lambda = (0.15 \pm 0.05) \text{ eV } \text{\AA}^{-2}$.

The much larger value of C_λ compared to C_ϕ suggests the elastic contributions are prevalent during the coexistence. We can now find $C_m = (9.76 \pm 6.06) \text{ meV } \text{\AA}^{-1}$, and so, from Equation 3.4, we can obtain the value for the entropy difference $\Delta S = (10.32 \pm 6.82) \times 10^{-4} \text{ meV K}^{-1} \text{\AA}^{-2}$.

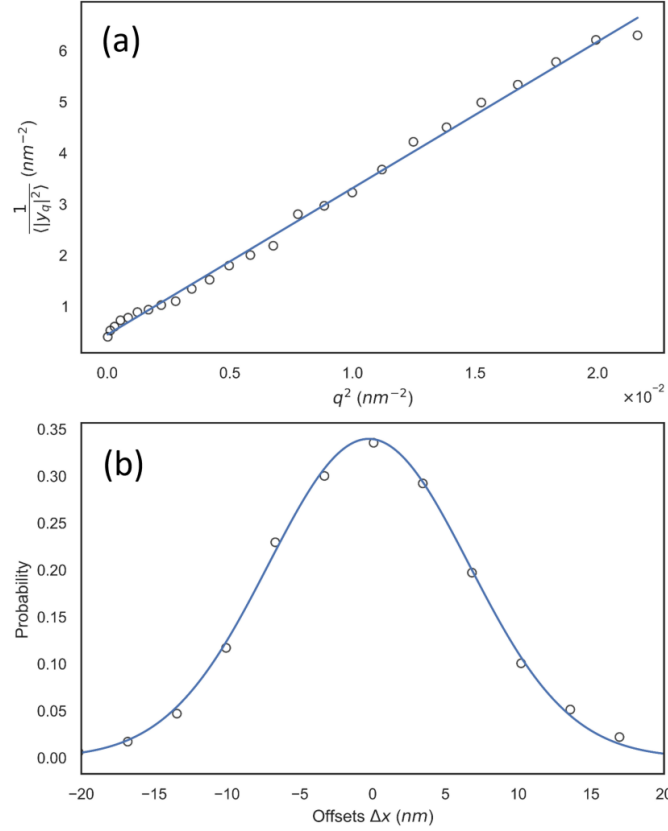


Figure 3.5: Example of the fluctuations analysis. These results were generated for the marked edge in Fig. 3.3.

(a) A linear fit of the Fourier components of the boundary fluctuations (Equation 3.8). The slope of the fit is $\frac{L_b \beta}{k_B T}$.

(b) Probability distribution of the boundary fluctuation deflections Δx , with respect to the mean boundary position (Equation 3.9). The measured standard deviation over all the data is $\sigma = (5.88 \pm 1.08) nm$.

3.5 Conclusion

The uncertainties in the results are in part due to the disordered nature of the surface steps configurations, affecting interactions at each individual boundary and giving a spread in the measured values for every analysed boundary. Nonetheless, the behaviour of the coverage, as seen in Figure 3.4, fits the predicted behaviour, providing a relationship between the entropy and elastic interactions at the boundaries that enables us to reach fundamental conclusions on the thermodynamics of the system. Despite the chaotic nature of the step arrangements and the complexity of the compound material, the coexistence in GaAs(001) obeys the same rules as

the coexistence in a more predictable and thoroughly detailed system, such as the one in Si(111) between the (1×1) and (7×7) phases in Hannon et al., 2001, giving confidence in the broad applicability of the method. The density-functional theory (DFT) calculations in previous works show that none of the available (6×6) models are stable at $T = 0$ K, as shown by Pristovsek et al., 2003. By contrast, experiments are conducted at a range of temperatures around $T_0 \approx 550$ °C, which has led to the suggestion that the entropy difference due to configurational entropy can help stabilise the (6×6) with its contribution to the formation energy by Seino et al., 2006; Zheng et al., 2019. In the context of the (6×6) , the entropy difference found above contributes to the formation energy with:

$$T_0 \Delta S = (13.6 \pm 9.0) \text{ meV } ((1 \times 1) \text{ cell})^{-1} \quad (3.10)$$

The contribution to the formation energy needed to stabilise the most energetically favourable (6×6) structure models is approximately $50 \text{ meV } ((1 \times 1) \text{ cell})^{-1}$ (Zheng et al., 2019). The contribution from the entropy difference in Equation 3.10 is not negligible, but not large enough to stabilise the (6×6) with respect to the $c(8 \times 2)$ by itself. These results strongly suggest that (6×6) phase is not stable and the elastic relaxation associated to the phase boundaries is necessary to stabilise it.

In conclusion, we propose a new methodology that brings together separate experimental methods that are well established within the LEEM community to provide an estimate of the entropy change between surface phases. The unified technique demonstrates the ability of LEEM microscopy to provide insight on elusive, but key thermodynamical parameters in semiconductors through a unitary, self-contained method. We show the applicability of the method on complex semiconductor materials and develop computational methods that generalise the approach to surfaces with irregular step geometry. With that, the developed method is capable of giving straightforward access to the entropy difference and stress difference between two coexisting phases on many semiconductor surfaces, adding valuable insights on phase transitions that can have a significant impact on surface science. Using the unified method, we resolve an important uncertainty around the surface energetics of GaAs(001), namely, we show that for the temperature spectrum where the (6×6) is observed in its coexistence regime, it is still the unfavourable phase, but the elastic relaxation at the boundaries during its coexistence with the $c(8 \times 2)$

phase is a key contribution to reach the lowest energy state of the surface and enable its stability.

3.6 Data analysis

Here, we give a summary of how the results are extracted from the raw data. First we look at how this analysis was done in the past, what were its weaknesses and why we need to solve our analysis with a new approach. We outline the procedures in each of the new developed algorithms for that purpose. Algorithm 1 takes raw images that go through a preprocessing procedure and detects the selected boundary in each image sequentially, outputting a list of boundary coordinates. Algorithm 2 takes the output of Algorithm 1 and transforms it into boundary offsets, outputting data that represents the boundary fluctuations in a robust and unbiased manner. Algorithm 3 takes the boundary offsets data and analyses it, as described in Section 3.4, outputting and recording the sought parameters and generating relevant graphical representations of the analysis. The importing of raw images in Python is done through the convenience of Lin Zhu's package at <https://github.com/zhulincqu/LEEMImage> and the images are processed using the scikit-image Python package (van der Walt et al., 2014).

3.6.1 Previous approaches

An overview of literature on similar experimental fluctuations measurements for line stiffness estimation is presented in Table 3.1. The works that were used as a basis for the boundary detection was done on LEEM images of Silicon by Hannon and Tromp, 2001, which monitors phase boundary fluctuations in an analogous manner to the much more explored step fluctuations (N. Bartelt et al., 1996). The images there were denoised using Boxcar averaging, which works by substituting each pixel with the average value of its neighbourhood - 9 to 11 pixels in the previous works. It is simple and quick, but comes with inherent drawbacks that lead to a reduction in the measured fluctuation amplitudes. The steps and boundaries were then detected by fitting a hyperbolic tangent (\tanh) function along at each line perpendicular to the average direction of the steps. The \tanh lines have a width of one pixel and fit

the intensity profile where they cross the image. Curve-fitting methods like this are powerful, but they are, just like all edge detection methods to different degrees, prone to getting fooled by the noise. Because of this, good control over noise during data gathering and its optimal removal during preprocessing is essential for the quality of the measurements. The ability for improvements over previous approaches stems from the availability and accessibility of newer techniques that have been shown to be very powerful, but a necessity also comes from the nature of the GaAs surface. In particular, the steps are more chaotic and can take complex shapes, as shown in Figure 3.6. The straight line in the average step direction used in the well-ordered

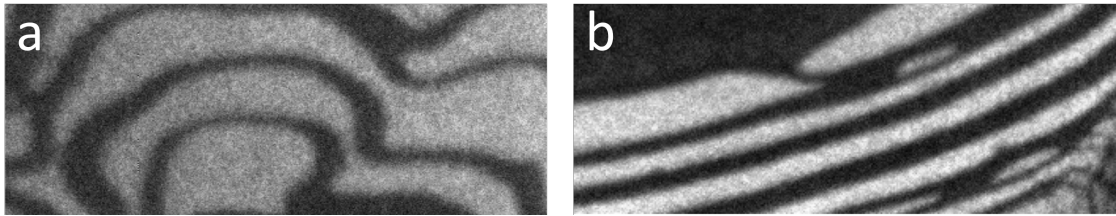


Figure 3.6: LEEM image examples of (a) a complex step arrangement and (b) a well-behaved step arrangement in GaAs(100), produced under the same experimental conditions, as detailed in the 'Experimental procedure' section. The image analysis should be aimed to perform well in both situations and not allow for hidden sources of error.

systems in previous works as a reference to measure step offsets would be prone to errors with the variations in the step shapes. The aim is to build a robust and automated modular pipeline for the detection, as well as the analysis procedures, taking the raw data from the microscope, saving the work done at each significant step and outputting the end results in numbers and graphs.

Publication	Material	Technique	Temperature	Type	Stiffness
Alfonso et al., 1992	Si(111)	REM	900 °C	Step	680 $\mu\text{eV nm}^{-1}$
N. C. Bartelt et al., 1993	Si(111)	REM	900 °C	Step	300 $\mu\text{eV nm}^{-1}$
N. Bartelt et al., 1996	Si(001)	LEEM	790 °C	Step	13 $\mu\text{eV nm}^{-1}$
Hannon and Tromp, 2001	Si(111)	LEEM	860 °C	Boundary	180 $\mu\text{eV nm}^{-1}$
Cohen et al., 2002	Si(111)	REM	1100 °C	Step	163 $\mu\text{eV nm}^{-1}$
Ondrejcek et al., 2003	Mo(011)	LEEM	820 – 1400 °C	Step	250 – 360 $\mu\text{eV nm}^{-1}$ (anisotropy)
Ondrejcek et al., 2004	Pt(111)	LEEM	1225 °C	Step	175 $\mu\text{eV nm}^{-1}$
Van Gastel et al., 2004	Pb on Cu(111)	LEEM	330 – 380 °C	Step	22 – 8 $\mu\text{eV nm}^{-1}$
Ondrejcek et al., 2005	Pd(111)	LEEM	730 – 1130 °C	Step	210 $\mu\text{eV nm}^{-1}$
Pang et al., 2008	Si(111)	LEEM	890 °C	Step	600 $\mu\text{eV nm}^{-1}$
Freitas et al., 2017	Cu(111)	MD sim.	1025 °C	Step	370 $\mu\text{eV nm}^{-1}$

Table 3.1: List of experimental work in finding step stiffness for a number of materials and temperatures.

3.6.2 Boundary Detection

During experiments, a large amount of data is collected that needs to be processed - more than 20000 frames from the 25 selected edges, each edge yielding a total of ≈ 130000 data points over all frames. Processing this data involves an initial denoising step, followed by edge detection and conversion of detected edges to boundary fluctuation data. This is then analysed through the methods described in the main text to give us the entropy difference between the two phases on the GaAs(100) surface. It is important to find the optimal trade-off between precision in measurements and stability of the methods used. This would help to achieve the best accuracy across the whole dataset without the necessity for error-prone and laborious manual inspection and corrections on each image frame. We utilise well-known powerful edge detection methods and approaches and adjust them to suit the task in hand. From here onward, we use the terms *edge* and *boundary* interchangeably.

Canny edge detection has previously been successfully employed to detect edges in scanning probe microscopy (SPM) imaging (Campbell et al., 2009) and more recently, it was shown to be effective with particle size estimation in scanning electron microscopy (SEM) images (Meng et al., 2018; Stephens et al., 2019). It works by using the image gradient at each pixel of the image to find whether that

pixel is a local maximum in its gradient direction. The directions are in windows of 45° , in both forward and backward directions, and if a pixel happens to be a local maximum in its gradient direction, it is recorded as an edge candidate and is a subject to a threshold and a connectivity search - e.g. it is more likely to be an edge if it has other edge candidate neighbours. The basis for the detection method here is the implementation in the scikit-image Python library (van der Walt et al., 2014). There, they give us the following summary of the process:

- * Smooth the image using a Gaussian with “sigma” width.
- * Apply the horizontal and vertical Sobel operators to get the gradients within the image. The edge strength is the norm of the gradient.
- * Thin potential edges to 1-pixel wide curves. First, find the normal to the edge at each point. This is done by looking at the signs and the relative magnitude of the X-Sobel and Y-Sobel to sort the points into 4 categories: horizontal, vertical, diagonal and antidiagonal. Then look in the normal and reverse directions to see if the values in either of those directions are greater than the point in question. Use interpolation to get a mix of points instead of picking the one that’s the closest to the normal.
- * Perform a hysteresis thresholding: first label all points above the high threshold as edges. Then recursively label any point above the low threshold that is 8-connected to a labelled point as an edge.

There are a few weaknesses in the Canny edge detection method that affect the precision of the phase boundary detection and need to be addressed.

The first issue arises in the **denoising step**. It uses a *Gaussian convolution*, which, similarly to Boxcar averaging, reduces the fluctuation amplitudes and can be especially detrimental to fine details, in this case - smaller fluctuations. To tackle this issue, a preceding more sophisticated denoising step can be applied, which preserves edges much better. With that, the strength of the Gaussian convolution

can be brought to a minimum and small fluctuations can be preserved.

An overview of state-of-the-art (SOTA) denoising methods can be found in Goyal et al., 2020 and an extensive survey of edge-preserving denoising algorithms was done in Jain and Tyagi, 2016. The main goal of the SOTA denoising algorithms is to remove noisy pixels while preserving edges and fine details. Linear Translation-Invariant (LTI) filters, like the mean filtering used in the past (N. C. Bartelt et al., 1993; Hannon & Tromp, 2001), or Gaussian blur filtering, have been found to be destructive towards sharp features, blurring edges and losing fine detail. For this reason, the current SOTA utilises non-linear and non-local methods, which enable better edge preservation, as described in Chapter 2.3.1. Bilateral Filtering and Non-Local Means (NLM) denoising were found to perform best. While both algorithms can be used with good success, NLM is strong in preserving texture and Bilateral Filtering is designed to preserve fine-grained image features, such as the small details in a phase boundary, and fits the analysis goals better.

These methods are specifically designed to deal with Gaussian noise, as is the noise added by the CCD camera sensor. However, another source in the experimental images is shot noise, which has a Poisson distribution. Thus, we can reasonably expect a mixture of Gaussian and Poisson noise in our experimental data. As shot noise is a signal dependent, whereas Gaussian noise is additive, the Gaussian targeted noise filtering methods, such as the Bilateral Filter, would have limited success in removing shot noise, even though such approaches are still utilised to reduce Poisson noise in recent LEEM image processing applications (de Jong et al., 2020). To check if this limited efficiency of Bilateral Filtering on shot noise has an effect over the final results in our experiments, we extract two sets of data from the image sequence of the same edge - the first one using our standard Bilateral Filtering, and the second one using the same Bilateral Filter in conjunction with an Anscombe Transformation, as shown in Figure 3.7. The Anscombe Transformation is a variance-stabilising method, which transforms a Poisson distribution into a Gaussian one, enabling the efficient application of Gaussian targeting noise filters (Anscombe, 1948; Mäkitalo & Foi, 2013). The results show that the Anscombe Transformation has a visible, but limited effect over the extracted data from the images, with the example analysis giving differences of $\Delta\sigma = 0.02 \text{ nm}$ in the standard

deviation and $\Delta\beta = 2.5 \text{ meV nm}^{-1}$ in the boundary stiffness. This suggests that the application of Bilateral Denoising on the experimental data is sufficient to prepare the images for analysis.

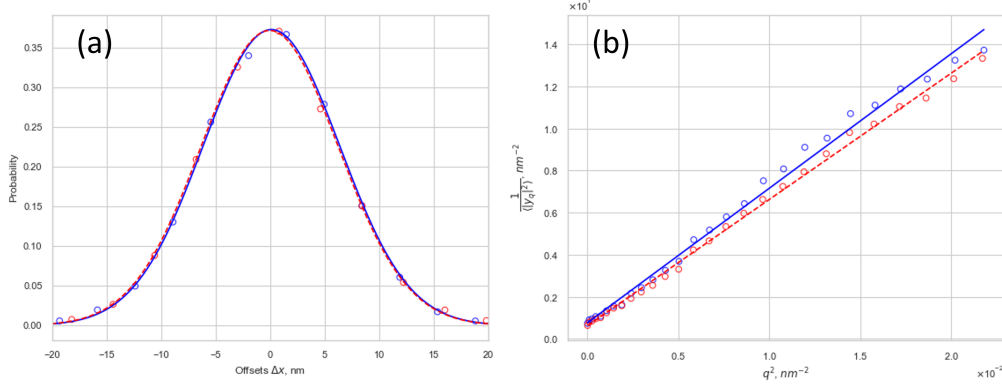


Figure 3.7: A comparison between results from denoising using only the standard Bilateral Filtering (solid blue lines) and an identical Bilateral Filtering in conjunction with the Anscombe Transformation (dashed red lines).

After the Bilateral Denoising, mostly features coming from imperfections of the channel plate may sometimes be preserved, requiring minimal Gaussian blur, down to a standard deviation of around $\frac{1}{4}$ of a pixel, or $\sigma \approx 1.5 \text{ nm}$, as opposed to the $\sigma \approx 12 \text{ nm}$ that the raw images would require otherwise. This can only affect very small fluctuations, which are error-prone anyways, falling far below the resolution of the microscope.

The algorithm is susceptible to **intensity gradients** across the images, as it uses thresholding to distinguish edges and noisy intensity variations. This is addressed by the local image preprocessing, as well as a more sophisticated thresholding method, called Otsu thresholding.

Canny's method detects edge *pixels*. It is a **pixel method** and so its accuracy is limited to the image grid size. To address this, we use a method by Devernay, 1995 that intuitively builds on it to give the detection *sub-pixel accuracy*. Canny edge detection uses Sobel kernels to find the gradient G_x and G_y in the horizontal and vertical directions, for each pixel and then sort the found gradients by direction, utilising the signs and magnitudes of G_x and G_y , as shown in Table 3.2. The magnitude at each point is:

$$G_0 = \sqrt{G_x^2 + G_y^2}, \quad (3.11)$$

Degree window	G_x	G_y	Magnitudes
$0 - 45^\circ$	+	+	$G_x > G_y$
	-	-	$G_x > G_y$
$45 - 90^\circ$	+	+	$G_x < G_y$
	+	-	$G_x < G_y$
$90 - 135^\circ$	-	+	$G_x < G_y$
	+	-	$G_x < G_y$
$135 - 180^\circ$	-	+	$G_x > G_y$
	+	-	$G_x > G_y$

**Table 3.2: Canny edge detection sort-
ing of gradient directions.**

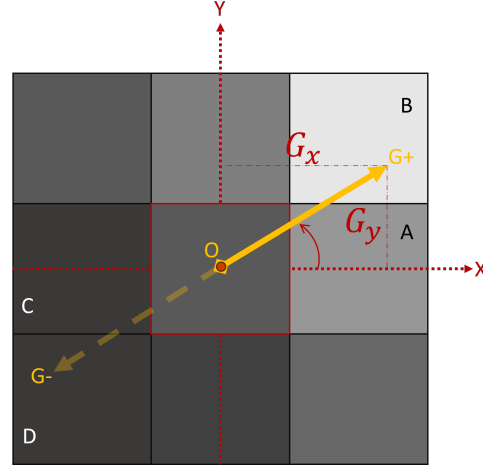


**Figure 3.8: A diagram of the image gra-
dient, calculated for a single pixel.**

and the normal to the edge is defined via the ratio:

$$w = \frac{G_x}{G_y}. \quad (3.12)$$

Using that, the gradient magnitudes a pixel forward and a pixel backward in the direction of the gradient can be estimated. This is done with a simple interpolation of the two nearest points to the gradient. The sorting of gradient directions into degree windows determines the used points. With the example illustrated in Figure 3.8, the gradients are:

$$G_+ = wG_A + (1 - w)G_B, \quad (3.13)$$

$$G_- = (1 - w)G_C + wG_D. \quad (3.14)$$

Here, G_A , G_B , G_C , G_D are the differences in intensity between the origin pixel O and its surrounding pixels A , B , C and D . If the magnitude of the gradient at the examined pixel is bigger than G_+ and G_- , the point is recorded as an edge candidate. Here, Devernay's method adds an extra step to find the location of the edge within this pixel with sub-pixel accuracy. Assuming the gradient profile is parabolic, as shown in Figure 3.9, it calculates a quadratic offset:

$$\eta = \frac{1}{2} \frac{G_+ - G_-}{G_+ + G_- - 2G_0}, \quad (3.15)$$

where, if the pixel is an edge, $-0.5 < \eta < 0.5$. The offset is expressed in the x and y directions and added to the pixel coordinates to give the method sub-pixel accuracy.

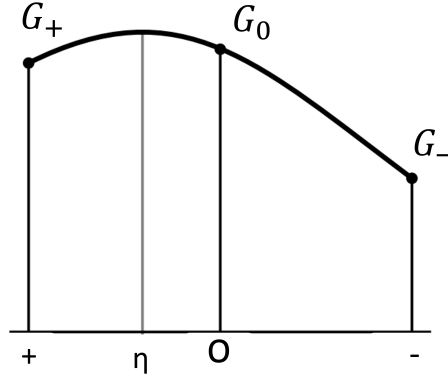


Figure 3.9: Example of the norm of the gradient profile in the direction of the gradient of the pixel at point O. Adapted from Grompone Von Gioi and Randall, [2017](#).

As with the standard Canny’s method, this process is done at each pixel, after which the algorithm moves on to connectivity and threshold checks. Since Devernay’s addition utilises the image gradients that are already found by the standard method, the new algorithm’s computational efficiency is close to the original method.

The last issue to address stems from non-ideal experimental conditions, rather than weaknesses in the algorithm. During the experiment, imperfections in the images are likely to occur. Namely, three variations in imaging are always going to be present during long imaging - **sample drift**, **intensity gradient** and **image flickering**. To correct for the sample drift, the first frame of each video is saved and used as a template to which all subsequent frames are aligned to match it. The alignment method uses the scikit-image implementation of fast, normalised cross-correlation, as detailed in Chapter [2.3.1](#). Intensity gradients are a common issue with edge detection tasks, which can cause the thresholding step to act differently in regions of the image with different intensities. A similar effect is caused by image flickering, which causes intensity differences between subsequent frames, rather than between image regions, as detailed in Chapter [2.3.1](#). To help with those, we utilise CLAHE histogram equalisation, which fragments each image into tiles and equalises histograms locally, enhancing and evening out the contrast in both dark and bright regions of the image. In our image preprocessing, the CLAHE equalisation was done in windows of $1/8$ of the image dimensions and using 256 bins. As well as adaptively enhancing the image contrast, we adaptively determine the thresholding values that are used by the edge detection step in the algorithm. For that, we use Otsu’s

method, which iteratively searches for the optimal threshold value. It goes through all possible thresholds to find the one which minimises the variance of the two groups of pixels that each threshold splits the image into. Calculating that separately for each image adds extra consistency between frames. The last improvement to help with intensity variations is to process the edge locally. The edge is selected and only the parts of the image that are around the selection are processed. This limits the intensity variations, as well as giving a significant performance boost to the algorithm's pre-processing steps.

The step-by-step algorithm for detecting the boundaries between the two surface phases is given in Algorithm 1.

Algorithm 1 Detecting a phase boundary

Input: Ordered list of Raw LEEM Images

Output: Coordinates of each point on selected boundary at each frame

```

1: for first image do
2:   Save in memory as template for Alignment           ▷ If images drifting with time
3:   Show to user
4:   Create mask of boundary, drawn by user
5: for each image ∈ rest of images do
6:   Alignment via template matching
7:   Crop image to fit only masked area
8:   CLAHE Histogram Equalisation
9:   Non-Local Means denoising
10:  Canny-Devernyay Edge Detection with mask and Otsu
11:  Get resulting binary images                       ▷ 0 ⇒ no edge, 1 ⇒ edge
    and sub-pixel boundary coordinates
12: Save coordinates of detected boundary to drive; shape: [frame, [x-coords, y-coords]]

```

3.6.3 Data transformation

The boundary detection algorithm results in the coordinates for a boundary as it varies its position in each recorded frame. The next step is to use the raw boundary positions to extract meaningful fluctuations data. We define a boundary

fluctuation y as an offset in the boundary position at a given frame t , with respect to the boundary's mean position over the full experiment duration $\langle y(x) \rangle$. This measurement is gathered at each position along the boundary x , for all frames t resulting in the boundary fluctuations data $y(x, t)$.

The simplest way of defining the position and direction of the fluctuations is to take a straight line in the general direction of the boundary and record offsets as perpendicular distances to it, for every pixel along it. However, the boundaries in our data are often curved and irregular. This means that this standard approach brings errors in detection, proportional to the angle at the local step direction compared to the mean direction. In other words, the degree of curvature and irregularities brings a corresponding degree of errors in the measured fluctuation offsets, as illustrated in Figure 3.10.

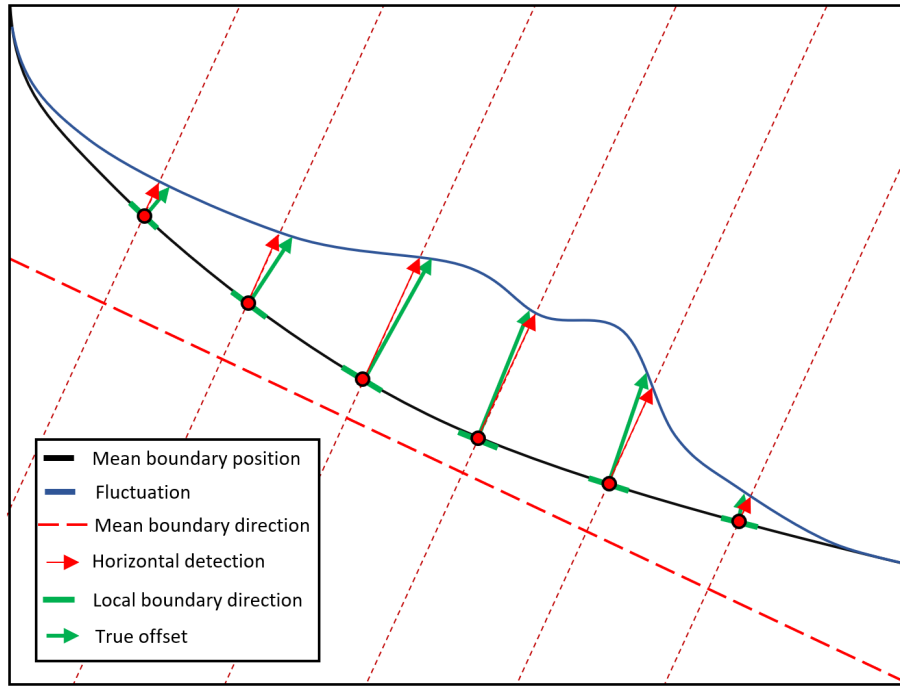


Figure 3.10: An illustration of how a curved step causes errors in the measured fluctuation offset.

To minimise this effect, we construct a unique reference system for fluctuations measurements on each boundary. To adapt to the boundary shape, we use the average position of the boundary. We smooth out small and sharp curvatures with the Ramer-Douglas-Peucker algorithm and only preserve larger-scale curvature to ensure stability in the measurements. The reference system is then created by constructing perpendicular bisectors across this reference shape.

The measurement against this reference system looks at where the boundary crosses these bisectors at each frame. As the line of the boundary is discrete, with each point on it corresponding to a pixel in the original image, we interpolate between the points on the line to find the crossing points with the bisectors. We use weighted essentially non-oscillatory (WENO) interpolations (Janett et al., 2019) to avoid the loss of accuracy with a linear interpolation, while also not suffer from instability in the interpolations.

This approach enables us to measure against the local boundary shape and direction, rather than the general global one.

Algorithm 2 Extracting boundary fluctuations

Input: Detected Edge Coordinates

Output: Edge fluctuation w.r.t. mean position

Load coordinates of detected edge for each frame from Algorithm 1

```

1: for edge coordinates of first frame do
2:   for each point on edge do
3:     Get neighbouring  $N$  points
4:     Smooth by approximating with Ramer Douglas Peucker algorithm
5:     Fit straight line segment through approximated polygon
6:     Build line segment bisector
7: for each edge coordinates  $\in$  rest of frames do
8:   for all bisectors do
9:     Find closest  $N$  points out of all points on edge
10:    Do WENO interpolation between points
11:    Cross interpolation with bisector and save position
12: for each bisector do
13:   Find mean position of all points on bisector
14:   Subtract mean from all points' positions
15: Save all positions: shape: [position on each bisector, frame]
```

Algorithm 3 Analysing boundary fluctuations

Input: Boundary fluctuations for one edge

Output: Distribution analysis and FFT analysis

- 1: **procedure** FOURIER TRANSFORM
 - 2: Load data of boundary fluctuations from Algorithm 2
 - 3: **for all** frames **do**
 - 4: Fast Fourier Transform of boundary offsets at each frame to find y_q^2
 in Equation 7 in the Main Text
 - 5: Perform linear fit of $\frac{1}{y_q^2}$ against q^2 and get slope
 - 6: **return** resulting β from slope of fit
 - 7: **procedure** FLUCTUATIONS DISTRIBUTION
 - 8: Load data of boundary fluctuations from Algorithm 2
 - 9: Compute histogram of data ▷ Only spacial distribution matters here
 - 10: Fit Gaussian to histogram, as predicted by Equation 3.9
 - 11: **return** mean, standard deviation of Gaussian
-

Chapter 4

Growth monitoring near a Ga droplet on GaAs (001)

4.1 Introduction

Molecular Beam Epitaxy (MBE) has been extensively developed and optimized in the past decades and remains a widely utilized technique for crystal growth today (Orton & Foxon, 2015). Its systematic and predictable layer-by-layer epitaxial deposition of materials allows for precise control over the growth process down to the sub-monolayer level, making it a popular choice among researchers and manufacturers who wish to produce materials and nanostructures with specific and highly accurate properties and qualities. However, in order to fully take advantage of the capabilities of MBE, a thorough understanding of the behavior of the surface during growth is necessary (Joyce & Vvedensky, 2004).

The aim of this work is to shed light on surface behavior during MBE growth and provide new insights into the control and manipulation of surface properties with the potential to inform the design of new materials with improved qualities. We utilize Low-Energy Electron Microscopy (LEEM) to observe surface growth dynamics during deposition and our focus falls on high-temperature growth on GaAs(001), which is the most widely used compound semiconductor in industry and often serves as a substrate for MBE growth (Wu & Jin, 2015). The growth on the high temperature Ga-rich surface reconstructions on GaAs(001) is known to produce a generally rougher final surface (Neave et al., 1984). The reasons behind the impact of recon-

structions on growth outcomes are significant, but still not fully understood (Ohtake et al., 2013; Ohtake et al., 2014).

The high-temperature growth process occurs on the Ga-rich $c(8 \times 2)$ surface, where we find a dynamic metastable coexistence between the $c(8 \times 2)$ and (6×6) phases, caused by the As-pressure. This is, as far as we are aware, the first such observation of phase metastability during MBE growth and has potential implications for the control and manipulation of surface properties. To give us a fuller picture, we use Ga droplets on the surface to act as our Ga source, giving us a spectrum of surface chemical potentials to observe (Zheng, Tersoff, et al., 2016). With that, we are able to quantitatively analyse our observations and gain insights for the surface behaviour during MBE growth.

4.2 Experimental details

4.2.1 Experimental setup

Experiments were performed using the Elmitec LEEM-III microscope. Details on the microscope can be found in Chapter 2.2.

A GaAs(001) sample is placed under ultra-high vacuum of around 2×10^{-10} Torr, its surface is initially prepared by annealing for 2 h at 580 °C. Gallium droplets of up to 5 μm in diameter are then produced at 620 °C and allowed to run on the surface, creating flat regions of at least 10 μm length (Tersoff et al., 2009; Zheng, Tang, et al., 2016). After the atomically flat surface is created, the sample is brought to 530 °C. At this point, surface is ready and the $c(8 \times 2)$ -covered reconstruction covers the flat regions near the droplet.

4.2.2 Experimental design

The sample is exposed to Arsenic pressure by opening an As cracker cell, with the cracker heated to 900 °C and the reservoir put at 380 °C. With the As-pressure on, a flat region near a droplet is continuously monitored at 4 frames per second and at a field of view of 10 μm . The imaging is done in Bright Field (BF) mode, at an electron energy of 8.5 eV. The Ga droplet is slowly consumed by the incoming As

and shrinks continuously, until it is fully gone. During that process, we observe small round (6×6) domains form at random places around the $c(8 \times 2)$ covered surface, then grow to different sizes and transform back into $c(8 \times 2)$, leaving behind a new round island on the surface. An example of a full raw image during the experiment is shown in Figure 4.1 and snippets from an example of the (6×6) patch evolution process are shown in Figure 4.2. As the droplet gets smaller throughout the experiment and the surface moves towards equilibrium, it allows a larger metastable (6×6) coverage. This coverage variation is due to the chemical potential gradient the droplet and the As-flux cause, which changes as the droplet size is reduced. The effects of that change are manifested through the forming (6×6) domains being allowed to grow to a progressively bigger size over the course of an experiment, before transforming back and leaving a $c(8 \times 2)$ terrace behind.

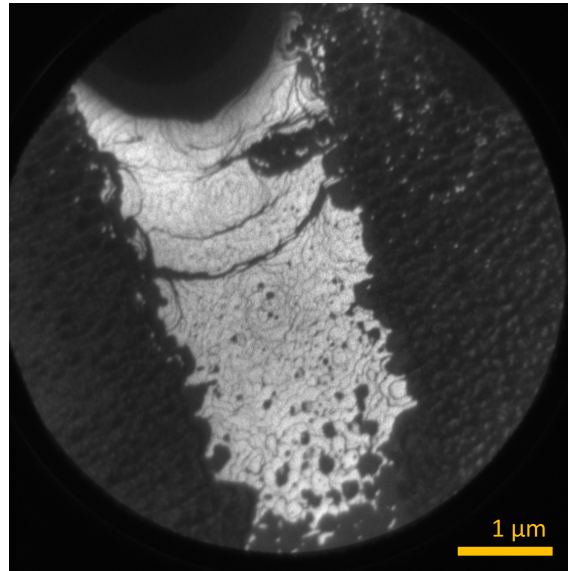


Figure 4.1: An image frame from the experiment. The droplet is partially visible on the top of the image. The (6×6) domains are the dark portions of the droplet trail, while the bright portions are covered by the $c(8 \times 2)$ phase. The images were taken in Bright Field with a beam energy of 8.5 eV.

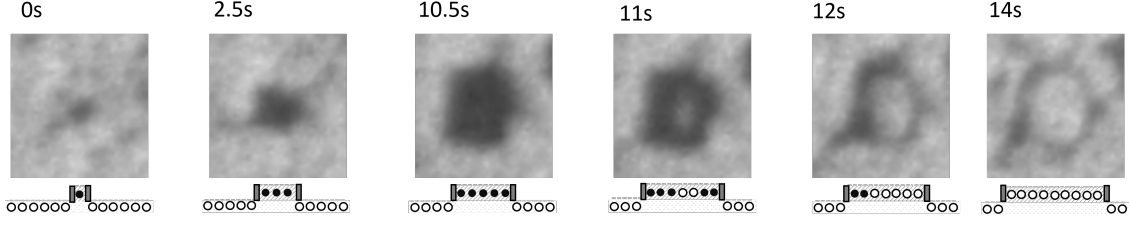


Figure 4.2: Example evolution of a (6×6) patch.

4.3 Analysis

The system can be described through the sizes of the (6×6) metastable domains at the moment of their transformation back into a $c(8 \times 2)$ terrace, which depend on the chemical potential μ_{Ga} at their position. Using Equations 2.25 and 2.26, the average radius upon transformation becomes:

$$\langle R \rangle = \Gamma^{(4/3)-1} \left(\frac{3\nu}{\pi\rho_0} \right)^{\frac{1}{3}} \exp \left(\frac{E_{barrier}}{3k_B T} \right) \quad (4.1)$$

The energy barrier of transformation $E_{barrier}$ is the energy where the transition between the (6×6) and $c(8 \times 2)$ phases occurs:

$$\frac{\partial E_{total/island}}{\partial R} = 0 \quad (4.2)$$

As described in Chapter 2.1.2, the total energy in the case of a circular phase domain includes contributions from the creation cost of the boundary between the two phases, the maintaining of the unfavourable phase and the elastic relaxation of atoms at the domain boundaries.

An insight on these contributions can be gained by examining how the domains grow. The full process of the detection of domain growth is described in Section 4.6 below. Overall, over 400 representative domain growth events were detected. A few representative examples of how domain sizes grow with time is shown in Figure 4.3a. As can be seen, the growth rate of the domains tends to be linear, suggesting that the elastic relaxation does not have a significant influence in this scenario (Hannon & Tromp, 2003). To confirm the linear trend, the linearity of all detected domains is checked by fitting a linear regression model to each and extracting the Pearson correlation coefficient (r-value) of the best fit. The extracted r-values are shown in Figure 4.3b and demonstrate a significant tendency of the domains to exhibit linear growth. Examination of patches with the non-linear growth behaviour in the

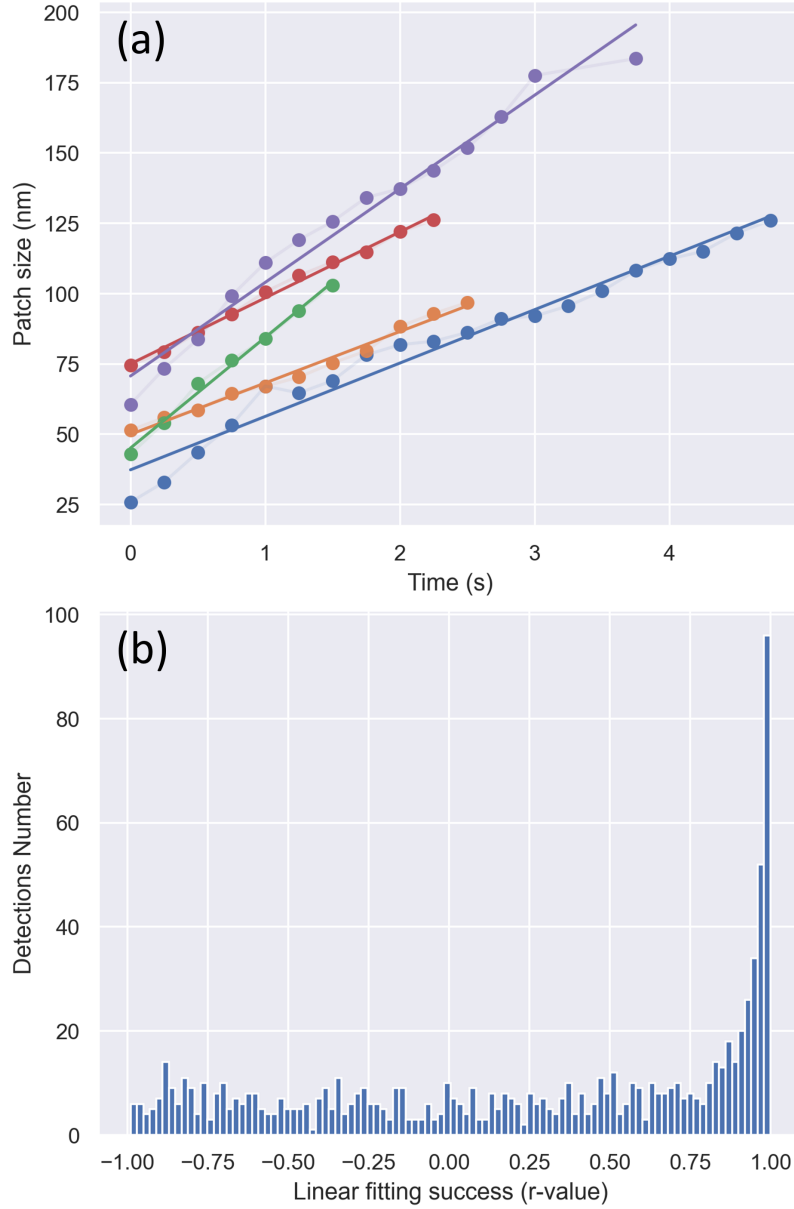


Figure 4.3: Linearity of the (6×6) patches' growth process. (a) Size evolution during growth of some example patches. (b) The linearity measurement for all (unfiltered) detections. The r-value reaches negative values due to a number of detected events, where (6×6) patches shrank until disappearance. The graph shows a sharp upwards trend in number of detections after an r-value of about 0.75.

experimental videos shows that the non-linearity is most often caused by the patch experiencing some interference from nearby steps or by a merging event with another patch during growth, while patches without such events during their lifetimes tend to exhibit linear growth.

In contrast to the stable phase coexistence case at the congruent temperature of $T_0 = 550^\circ\text{C}$ detailed in Chapter 3, in the current case away from that temperature

the data suggests the elastic relaxation is negligible. Using Equation 2.27, the total energy of a circular domain of size R then becomes:

$$E_{total/island} = 2\pi RC_b + \pi R^2 \Delta\gamma \quad (4.3)$$

where C_b is the energetic cost of creating a unit length of boundary, and $\Delta\gamma$ is the free energy difference between the two phases and can be expressed with the chemical potential μ_{Ga} through $\Delta\gamma = (\Delta N_{As} - \Delta N_{Ga})(\mu_{Ga} - \mu_{Ga}^c)$. Differentiating Equation 4.3 using 4.2, the critical radius upon transformation becomes $R_{critical} = \frac{-C_b}{\Delta\gamma}$. This can now be substituted to express the energy barrier for $c(8 \times 2)$ phase nucleation:

$$E_{barrier} = \frac{\pi C_b^2}{(\Delta N_{Ga} - \Delta N_{As})(\mu_{Ga} - \mu_{Ga}^c)} \quad (4.4)$$

Using this and Equation 4.1, the average domain radius upon transformation is:

$$\langle R \rangle = \Gamma(4/3)^{-1} \left(\frac{3\nu}{\pi\rho_0} \right)^{\frac{1}{3}} \exp \left(\frac{\pi C_b^2}{3k_B T (\Delta N_{Ga} - \Delta N_{As})(\mu_{Ga} - \mu_{Ga}^c)} \right) \quad (4.5)$$

4.4 Results

In Equation 4.5, it can be seen that the average critical radius is a function of the chemical potential μ_{Ga} at the spot where a (6×6) domain nucleates. To model the observed growth with that equation, we need to extract μ_{Ga} from the experimental data.

The chemical potential μ_{Ga} is strongly affected by the nearby Ga droplet during the experiment. As shown in Figure 4.4, Zheng et al., 2019 maps the chemical potential μ_{Ga} to a Ga droplet, putting its value at the droplet edge at $\mu_{Ga} = 0$ eV. Likewise, the transition between the $c(8 \times 2)$ and (6×6) phases is mapped at $\mu_{Ga} = -0.125$ eV.

These two events of interest can be tracked during our experiment and used as references for extracting μ_{Ga} . The chemical potential between the two points is assumed to have a linear behaviour. As mentioned before, during the As-flux in the experiment, the Ga droplet is gradually consumed over time, meaning that μ_{Ga} is not only a function of the distance to the Ga droplet, but also varies with time. This is practically observed through the $c(8 \times 2) \rightarrow (6 \times 6)$ transition boundary, which moves towards the droplet, as the droplet gets consumed over time in the

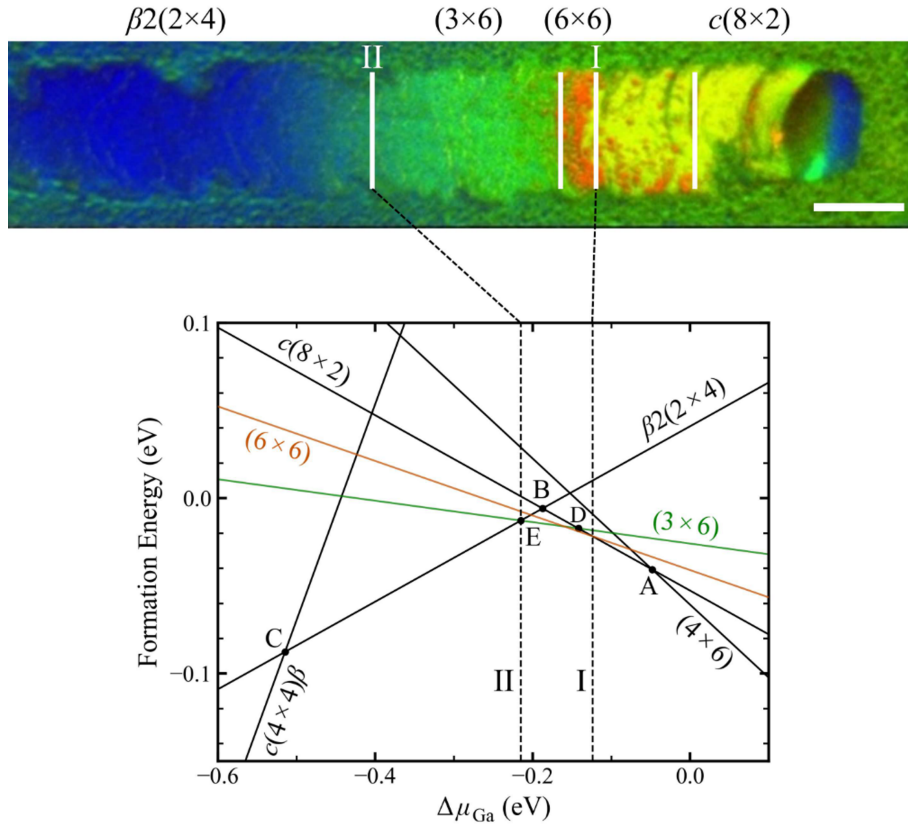


Figure 4.4: The observed phases on a Ga droplet trail and their extracted phase diagram mapping. We use the experimentally derived chemical potential transition point **I** as a reference, and set the chemical potential at the edge of the droplet at $\mu_{Ga} = 0$ eV. Both of these points of interest are visible throughout most of our observations. Adapted from Zheng et al., 2019

experiment, as seen in Figure 4.5. By knowing or extrapolating the position of the (6×6) , we now have two reference points, which map to known chemical potential values from Figure 4.4 - the position of the droplet edge at $\mu_{Ga} = 0$ eV and the position of the (6×6) transition at $\mu_{Ga} = -0.125$ eV.

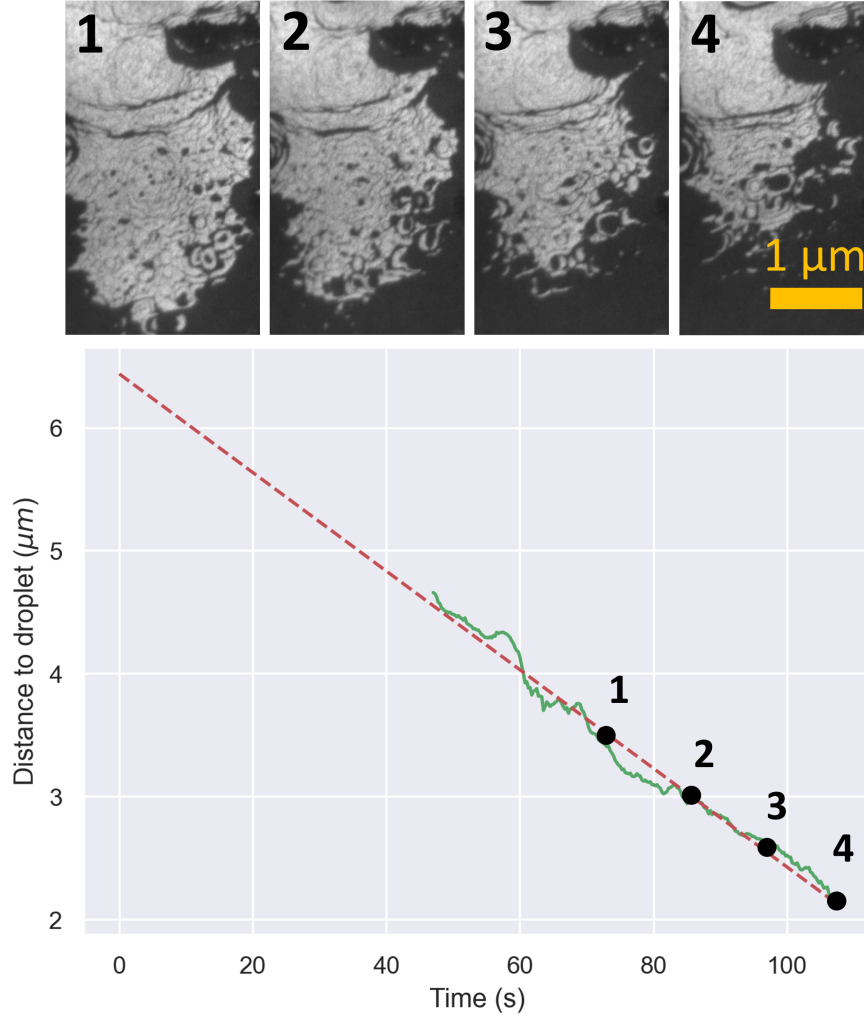


Figure 4.5: (6×6) boundary movement. The boundary is not always visible throughout the experiment. In the initial stages of the growth, the Ga droplet is still big and the boundary is too far out of the Field of View. To estimate its position, it is extrapolated (red line) from the position measurements at the final stages of the growth (green line), which show a linear boundary movement with time. The movement of the boundary movement is illustrated in experimental video frames shown above, which are selected at an equal time interval.

Another parameter that can be estimated from the experimental data is the step velocity ν . This can be observed through the growth rate of the (6×6) patches. As shown previously, the patches' radii grow at a constant rate. As the (6×6) patches are constrained by a circular step, the growth velocity is determined by the step velocity ν . Figure 4.6 shows the distribution of growth rates of the radii of all (6×6) patches, which are equivalent to the step velocity ν .

The peak of the fitted distribution is at $\nu = 22 \text{ nm s}^{-1}$.

The change in reconstruction atoms ($\Delta N_{As} - \Delta N_{Ga}$) can be estimated from the

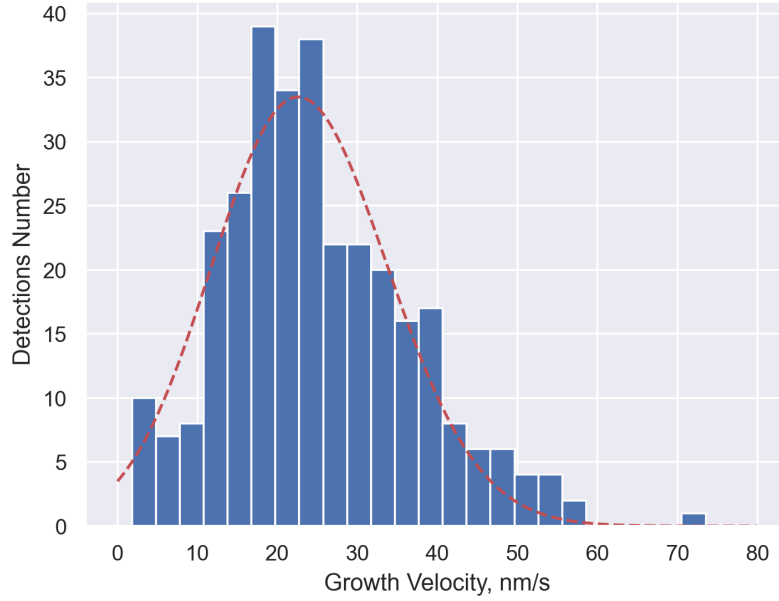


Figure 4.6: Step velocities distribution. The distribution follows a Displaced Poisson curve (red).

phase diagram in Figure 4.4. The difference between the slopes of the $c(8 \times 2)$ and (6×6) can be used, giving $(\Delta N_{As} - \Delta N_{Ga}) = 0.09$. The estimates for the step velocity and the reconstruction atoms change parameters fit directly into Equation 4.5. With the estimate of the chemical potential μ_{Ga} , which is the variable in the model, also defined, we are only left with the density of nucleation sites ρ_0 and the cost of boundary creation C_b . We gather the radii upon transformation for the (6×6) patches using an automated Computer Vision algorithm, demonstrated in Section 4.6, and we fit the model to the experimental data against these two fitting parameters. To address the bias in the transformation data coming from the uneven distribution along the chemical potential axis, the regions with larger amounts of data points are given more weight in the fit compared to regions with fewer points, proportional to the number of data points. This gives more importance to the more representative regions of the data and limits the bias of the uneven spread. The result of the fitting is shown in Figure 4.7. and yields an edge energy of $C_b = (4.340 \pm 0.001) \times 10^{-2} \text{ eV nm}^{-1}$ and a nucleation site density of $\rho_0 = (416.8 \pm 1.2) \text{ nm}^{-2}$.

The probabilistic behaviour of the patch size distribution is visible in Figure 4.8.



Figure 4.7: Patch size against chemical potential upon transformation. The final size of each patch before transformation is represented with a blue dot. The *average* radius size (green bars) is calculated for chemical potential steps of $\Delta\mu_{Ga} = 0.015 \text{ eV}$ and the fit from Equation 4.5 is shown with the red dashed line.

The Normal distribution suggests that the thermal-based approach we apply is valid, as opposed to approaching the problem with an energetically fixed transformation barrier that would have been seen if the elastic relaxation at the phase boundaries played a main role in stabilising the unfavourable (6×6) phase. In such a case, a clear cut-off would be seen at the small-sized patch transformations, as well as a narrower overall size spread. Rather, the surface thermally jumps from the local energy minimum associated to the (6×6) to the global energy minimum associated with the $c(8 \times 2)$ with some probability, resulting in the distribution shape. As we see a minor skew in the Normal distribution, this might be an indication of a weak presence of elastic relaxation interactions, but could also be due to a bias in the detection algorithms, which naturally tend to detect larger patches easier.

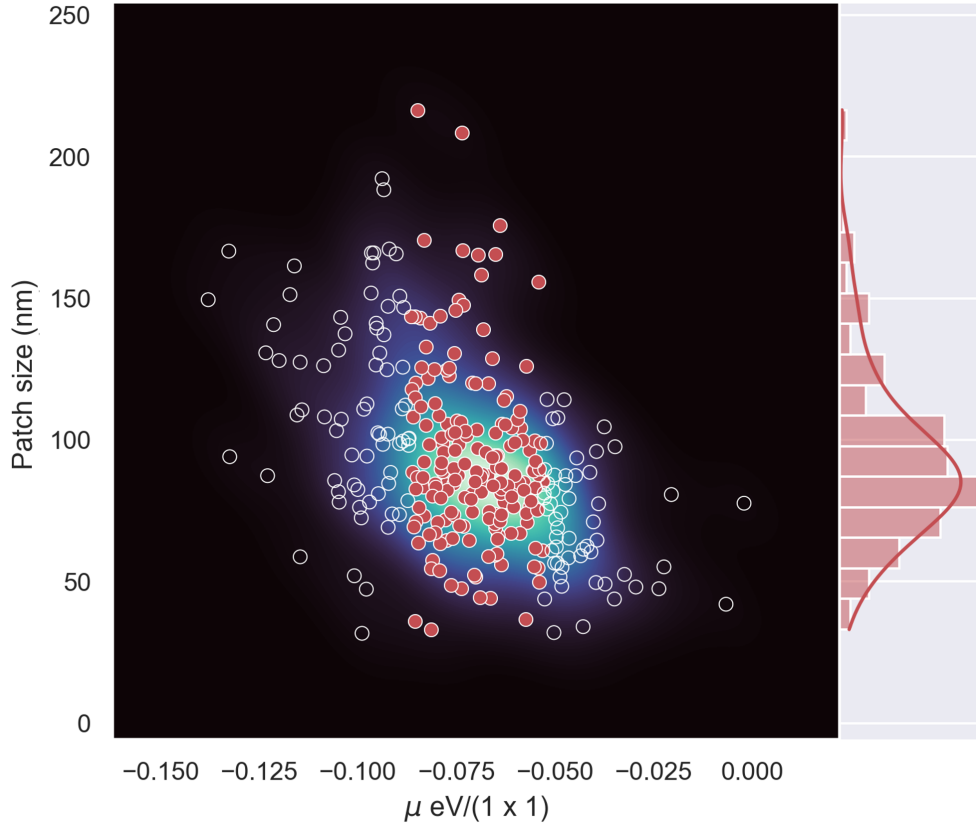


Figure 4.8: Density distribution of detections. The chemical potential region where most detections were captured throughout the experiment is isolated (red dots). The distribution of these detections shows a Gaussian spread in transformation sizes.

4.5 Conclusion

The LEEM-MBE system was used to observe dynamic phase coexistence during growth on GaAs(001), providing valuable insights into growth on the high-temperature $c(8 \times 2)$ phase. We are able to describe and quantify the processes during the metastable growth and extract meaningful surface parameters. We show that the observed metastability process has a strong dependence on the surface chemical potential and obeys a probability distribution, defined by an Arrhenius temperature dependence on the probability of growth.

As far as we are aware, this is the first time metastability is observed during surface growth. The metastable behaviour of the surface during growth on $c(8 \times 2)$ can be a substantial reason to why such growth generally turns out rougher than growth on $\beta(2 \times 4)$ and $c(4 \times 4)$ surfaces.

4.6 Detection Methods

The (6×6) patches detection was automated through an algorithm consisting of Computer Vision preprocessing and detection methods and a simple registry object-tracker method. The resulting detection points are filtered through a set of criteria based on their features to remove false-positives. In total, $n = 313$ detected patches are extracted from the experimental data - a video, consisting of a 430 image frames taken at 4 fps.

4.6.1 Preprocessing

The initial step is aimed at removing the sample drift that is present throughout the experiment. This is done through the Template Matching technique, as described in Chapter 2.3.1. Image alignment is vital in making the subsequent object-tracking more consistent. Other preprocessing steps, such as denoising and correction for image gradients, are not needed, due to the good intensity achieved during imaging and overall high quality of the image data.

4.6.2 Detection

The images are in grayscale, where the bright parts are the $c(8 \times 2)$ phase, while the (6×6) patches and the surface steps are dark. To detect the patches, we employ a simple but effective Computer Vision approach of binarising the image and using a Blob Detector. For each video frame, we apply a threshold to the image and utilise the "*simpleBlobDetector*" method in the OpenCV library, which follows the steps:

- * Extract connected components from every binary image and calculate their centers.
- * Group centers from several binary images by their coordinates. Close centers form one group that corresponds to one blob.
- * From the groups, estimate final centers of blobs and their radiuses and return as locations and sizes of keypoints.

This performs better on the data than the gradient-based methods like *Laplacian of Gaussian*, *Difference of Gaussian* or *Determinant of Hessian*. A more elaborate approach using a *U-Net algorithm* was also examined. It was trained on artificially generated data to segment the image into $c(8 \times 2)$ regions, (6×6) regions and steps. Although the approach is promising, it requires careful data engineering and model tuning, which fell beyond the scope of this work.

The image thresholding used along with the Blob Detector was a global Otsu threshold, chosen due to its relative simplicity, noting that a k-Nearest Neighbours (kNN) algorithm for colour segmentation also performed equivalently. The Otsu method for thresholding is presented in detail in Chapter 2.3.1.

4.6.3 Object Tracking

(6×6) patches persist over multiple video frames and tracking them through their lifetime is done using a simple dictionary-based object registry system. The registry accepts patch detections as the Blob Detection algorithm goes through the video frames. It recognises *visible patches* that are present at the current time, and *disappeared* patches, that have been observed some frames ago, but are no longer active. Throughout the video, it tracks the positions of all detected patches for a new frame and the distances to the current dictionary of visible patches. Through these distances, the registry decides if the newly observed patches match active detections, or are newly formed domains that become new entries in the registry. It also retires active patches that have not been matched in the new frames. The usage of distances between objects in consecutive frames is where the preprocessing frame alignment step plays an important role.

With this simple tracking approach, we are able to accurately stack multiple blob detections over consecutive frames into a single patch's lifetime. The patch "lifetime" is naturally captured by the Blob Detection algorithm, as it stops considering a (6×6) patch a blob once it starts transforming into the $c(8 \times 2)$, as at that point it rapidly gains bright area inside its boundary.

4.6.4 Filtering

After the detection process is complete, all registered (6×6) patches over the whole video are put through a filtering process. The aim is to remove the false positive detections, through a set of validation checks. Common sense criteria are used against the collected stats for each patch. The rules for a registered detection to be considered a real detection are:

- **The patch lifetime must be longer than a second.** A short detection, even if it is an accurate one, brings no information for the analysis.
- **The detection must be entirely inside the video frame at all times.** Some parts of the surface go in and out of frame due to sample drift, which introduces inconsistencies in possible detections in such regions.
- **The patch must grow at all times.** There are also shrinking patches, which are not the focus in the study. Otherwise, if the patch does not grow consistently, it is very likely a false detection of another surface object.
- **The growth of a patch must be reasonably linear.** The limit is set to $r - value \geq 0.75$, which is based on Figure 4.3b). This removes patches, that although real, have been interfered by another object on the surface and are no longer representative data points.

The full procedure for the data extraction is given in Algorithm 4.

Algorithm 4 Patch Detection

Input: Raw LEEM images

- 1: **for each** Frame **do**
- 2: **procedure** FRAME ALIGNMENT(*Previous Frame*, *Current Frame*)
- 3: Create *template* from *Previous Frame*.
- 4: Find position of template in *Current Frame*.
- 5: Apply **Translation** to shift *Current Frame* and match *template* position.
- 6: **return** Shifted *Current Frame*
- 7: **procedure** BLOB DETECTION(Current Image)
- 8: Binarize image with **Otsu thresholding**
- 9: Detect Blobs with **cv2.simpleBlobDetector**
- 10: **return** *Blobs Stats* - position, size for all detections
- 11: **procedure** REGISTRY(*Blobs Stats*)
- 12: **for** *Blob Stats* in **each** frame **do**
- 13: Recover previous positions of active detections from *Registry Dictionary*
- 14: Create *distance matrix* by comparing positions to active detections
- 15: Associate each new detection to the best-corresponding active detection using *distance matrix*.
- 16: Threshold distances of corresponding patches to distinguish: *persisting detections*, *new detections* and *vanished patches*.
- 17: Update *Registry Dictionary*
- 18: **return** Position, Size for all detections
- 19: **procedure** FILTERING(*Blob Stats* over all frames)
- 20: **for each** Registered Patch **do**
- 21: Check compliance to **Filtering Rules**
- 22: **return** Filtered detections

Chapter 5

Real-time interpretation of CBLEED patterns with Autoencoders

5.1 Introduction

Low-Energy Electron Microscopy (LEEM) is an established technique in the field of Material Science, with its unique properties making it invaluable in gathering fundamental insight into semiconductor surfaces. In crystalline samples, LEEM is accompanied by its complementary technique for surface reconstruction characterisation - Low-Energy Electron Diffraction (LEED). With the electron beams' shallow surface penetration depth, LEED extracts structural information by tapping into reciprocal space. The electron beam in LEED can utilize energies in the range of a few eV to 100 eV, leading to an electron penetration depth of only a few atomic layers of the sample surface. Varying the energy in that range produces intensity-voltage $I(V)$ curves, giving a comprehensive view of the electron band structure at the surface of a crystalline sample. As the electron beam normally illuminates a large portion of the surface simultaneously, this information is convoluted over that surface. To extract structural information for a spatially localised region of interest, LEED is routinely used along with a small and well-positioned aperture, illuminating surfaces patches with diameters of the order of a few hundred nanometers.

While micro-LEED (μ LEED) gathers information using planar-wave electron

beams of normal incidence, Held et al., 1995 observed that having a beam approach the surface at different angles results in significant intensity modulations in the LEED pattern and enables the gathering of "*beam-rocking curves*". This provides additional structural information for the point of incidence. Spence et al., 2004 built on the same concept, suggesting the *converging beam* geometry to have multiple beams approaching the same spot at different angles, replicating the rocking curve output, but from a significantly smaller incidence area.

The idea of convergent electron beams has been explored in the past (Buxton et al., 1976). In practice, Convergent Beam Electron Diffraction (CBED) has been extensively developed in the context of Transmission Electron Microscopy (TEM) (Bird & Saunders, 1992; Goodman, 1975; J.A.Eades, 1986; J.M. Zuo, 1998; Lazić et al., 2016; LeBeau et al., 2010; Tanaka et al., 1980; Tsuda & Tanaka, 1999; Vincent & Midgley, 1994). Over the years, the TEM-based CBED has been utilised in various applications to a significant impact, such as characterising crystal defects (Ponce, Cherns, et al., 1996), lattice polarity determination, (Kato et al., 2004; Ponce, Bour, et al., 1996), lattice misfit measurement (Völkl et al., 1998), charge-density distribution mapping (Zuo et al., 1999), measuring strain fields (Clément et al., 2004) and more. Although CBED is a very versatile approach, it predominantly examines the bulk of crystalline samples and the relatively high beam irradiation on the sample during TEM, and especially with CBED, is still a challenging problem for imaging beam-sensitive materials (Lv et al., 2022).

Applying convergent beam in LEED in analogy with CBED mitigates these limitations due to the shallow penetration depth and the sample-preserving nature of the low energy electrons. These benefits allow the gathering of detailed structural information from the surface from localised regions down to several nm in diameter, much smaller than the minimal region diameters of 250 nm in μ LEED imaging (Altman, 2010). Thus, the adoption of Convergent Beam Low-Energy Electron Diffraction (CBLEED) can lead to a plethora of new applications and research findings. To make the application of CBLEED more functional and seamless, we demonstrate a method for the analysis and interpretation of the complex and abstract CBLEED patterns. With this, we aim to help streamline the adoption of the powerful experimental technique.

We show that a Machine Learning (ML) approach is able to learn and identify key surface structure properties based on the observed CBLEED pattern. We propose a tool, which enables an automated real-time read of CBLEED patterns through the joint use of a deep learning Autoencoder (AE)-based architecture and a simpler ML model. This serves to efficiently inform the researcher during an experiment, making it a more controlled and explainable process. Furthermore, the relatively inexpensive and quick analysis gives a valuable pointer towards the appropriate structures that were observed, mitigating the need for guesswork and exploration of possible structures when experimental data is fitted with simulations. With this, the approach increases the quality of the extracted information from an experiment and mitigates the need for intensive and expensive computation in order to understand the data after its acquisition.

5.2 Overview

The subject of CBLEED patterns has so far been primarily approached through scattering simulations. Spence et al., [2004](#) demonstrated the equivalence of CBLEED to the information from a conventional I-V curve. The individual LEED spots convolute into disks on a CBLEED pattern, as shown in Figure [5.1](#). There, multiple scattering calculations in metals were used to show the effectiveness and sensitivity of the approach to the surface potential.

Ruben et al., [2009](#) provided a basis for simulating CBLEED patterns on crystalline surfaces. Through kinematic single electron scattering simulations, they showed the sensitivity of the CBLEED pattern to different surface reconstructions and atomic displacements in Si(001) and established the structural sensitivity of CBLEED patterns. Constantinou and Jesson, [2019](#) built on that, performing more sophisticated multiple scattering simulations, which yield much more accurate variations in CBLEED pattern intensities in response to small atomic displacements.

The outlined current progress in the research on CBLEED patterns provides computational methods of reaching a CBLEED pattern from a determined structure and electron energy. With that, the currently available method for experimental data interpretation is the traditional brute force approach of producing a range of patterns

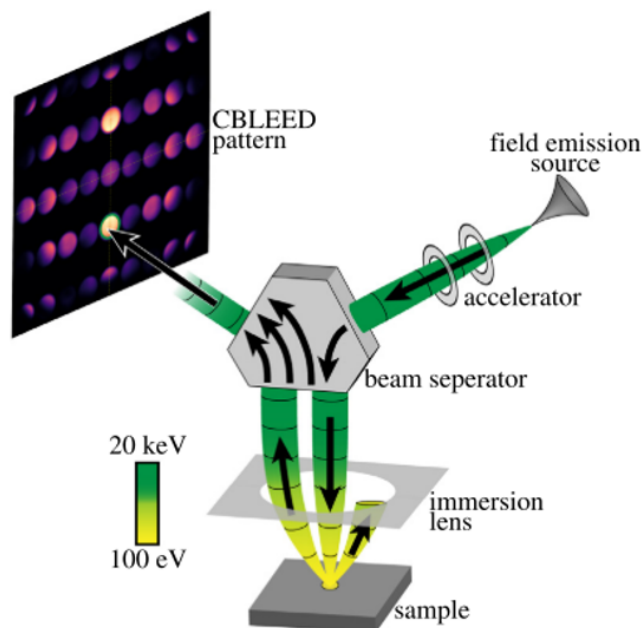


Figure 5.1: CBLEED image formation diagram. The immersion lens or the last condenser lens in the illumination column of the LEEM microscope can be used to have the beam converge at a point in the sample. Adapted from Constantinou and Jesson, 2019.

and matching with experimental ones. Unfortunately, the cost of the brute-force approach scales sharply with the complexity of the examined material, where the variational space quickly becomes large. Furthermore, the convoluted and abstract nature of the patterns does not allow manual interpretation, by eye, of a pattern by a researcher. This makes the practical application of the CBLEED technique quite difficult and expensive. On the other hand, the availability of simulated CBLEED data enables a data-centric statistical approach of analysing CBLEED patterns using Machine Learning.

Machine Learning and Deep Learning algorithms have recently been showing a lot of promise and prowess in their applications on microscopy data across a variety of microscopy imaging techniques (Ede, 2021b). In particular, ML algorithms have been successful in their application in interpreting a variety of diffraction imaging data, such X-ray diffraction (J. W. Lee et al., 2020; Oviedo et al., 2019; Suzuki et al., 2020; Vecsei et al., 2019; Wang et al., 2018), reflection high-energy electron diffraction (Kwoen & Arakawa, 2020, 2022), electron backscatter diffraction (Kaufmann et al., 2020), scanning precession electron diffraction (Martineau et al., 2019) and more. In particular, we approach the problem of CBLEED pattern analysis using a

Convolutional Neural Network (CNN)-based AE architecture. The AE architecture was recently used in the analysis of X-ray diffraction patterns (B. D. Lee et al., 2022; Utimula et al., 2022). Additionally, the speed and ability of CNN-based networks for extraction of physical parameters, have recently been demonstrated in the close context of CBED by W. Xu and LeBeau, 2018 and Zhang et al., 2020.

5.3 Methods

5.3.1 Dataset

The CBLEED dataset we use is generated by Constantinou and Jesson, 2019 through multiple scattering simulations of patterns on Si(001). The simulations adapted the CAVATN package, which is based on the CAVLEED program (Titterton & Kinniburgh, 1980). The simulations for the images used here were performed on the symmetric-dimer and buckled-dimer (2×1) structures. The electron incidence energy was varied between 30 – 100 eV and a range of dimer displacements were introduced to generate a total of about 5000 images in the dataset, examples of which are shown in Figure 5.2.

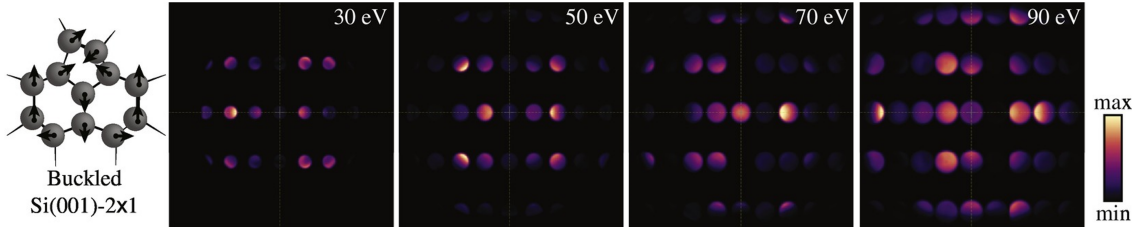


Figure 5.2: Examples from the CBLEED dataset. The dataset was generated by introducing sub-angstrom dimer displacements along the dimer-height and dimer-length, relative to a symmetric-dimer Si(001) - (2×1) structure. Adapted from Constantinou and Jesson, 2019.

5.3.2 Model Training

For this work, we utilize an autoencoder-based architecture to capture the semantics of the data. AE networks are a type of neural network techniques that learns how to compress and reconstruct high-dimensional data in an *unsupervised* manner. In an autoencoder, the input data is first encoded into a low-dimensional

representation, also known as the *latent space*, by a series of non-linear transformations through a set of encoder layers. This latent representation is then decoded back to the original high-dimensional space by a series of decoder layers, producing a reconstruction of the input data. Since the input data is in the form of images, the encoder and decoder networks in our architecture are constructed from convolutional layers, followed by a group of fully connected layers and the two networks mirror each other. The full Deep Convolutional Autoencoder (DCAE) architecture is shown in Figure 5.3.

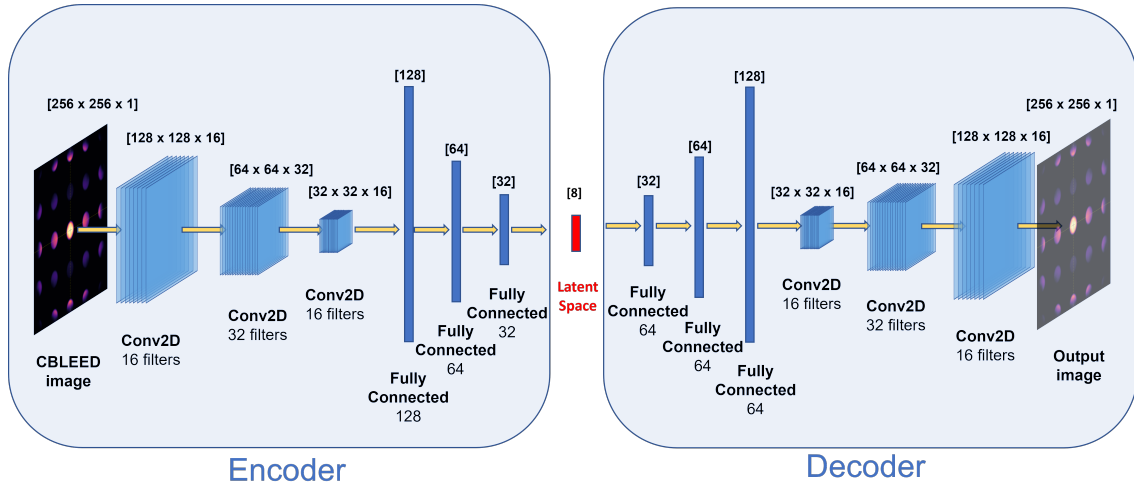


Figure 5.3: Deep Convolutional Autoencoder architecture. All convolutional layers apply "Same" padding, a kernel stride of 1. The encoder convolutions are followed by a MaxPooling layer and the decoder convolutions are followed by an UpSampling layer.

The encoder and decoder networks are trained simultaneously using backpropagation to minimize the difference between the input and output. This reconstruction goal is measured using Binary Crossentropy (BCE) loss:

$$L(y, \hat{y}) = -\frac{1}{N} \sum_{i=1}^N y_i \log(\hat{y}_i) + (1 - y_i) \log(1 - \hat{y}_i) \quad (5.1)$$

where y is the true binary label, \hat{y} is the predicted probability of the positive class, and N is the number of samples in the batch. The loss function measures the dissimilarity between the original and predicted images, with a higher loss indicating a poorer reconstruction. Here, BCE is used over simpler loss functions, such as the Mean Absolute Error (MAE) and Mean Squared Error (MSE), as it generally has the small advantage of preventing loss saturation and being a convex function. Examples

of the reconstructive ability progress of the DCAE network during its training are shown in Figure 5.4.

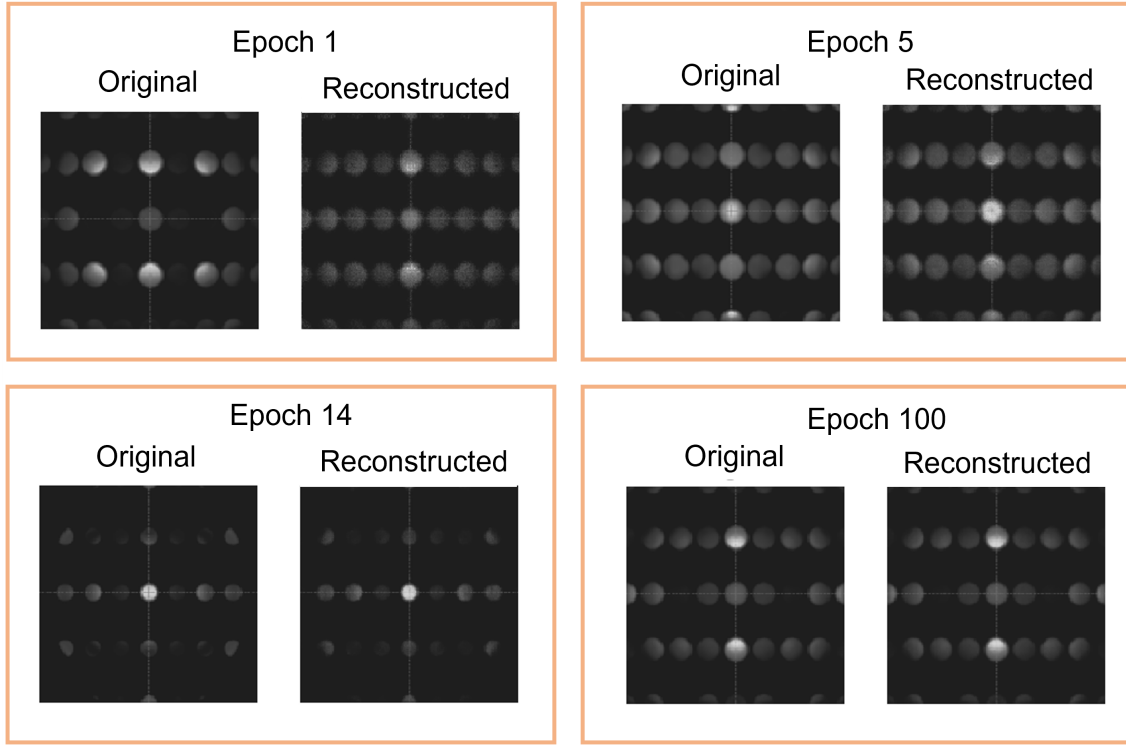


Figure 5.4: The training of the autoencoder in examples. The reconstructions of the data examples get progressively more accurate and sharper with each iteration over the dataset during training (epoch).

A consequence of the data flow and a key feature during autoencoder learning is that the data must be squeezed through the bottle neck of the small latent space without losing its essential features. As a result, the latent space needs to act as a compressed representation of the input data that preserves the important information while discarding the redundant or irrelevant information.

5.4 Analysis

The latent space of the autoencoder can be used to extract valuable information from the CBLEED pattern images by providing a compressed, lower-dimensional representation that captures the essential features of the patterns. By exploring the latent space structure, we can identify patterns, trends and clusters of similar data points which are not apparent in the original images. This can give insights onto the parameters of the structure, which produced its corresponding CBLEED

pattern. With that in mind, the size of the latent space becomes the most important hyperparameter in our AE architecture for the task.

5.4.1 Latent space size

To get the most out of the latent space, its size must be carefully chosen. While too small of a latent space will contain too little information and may start losing valuable information, too large of a latent space will hold too much information, lose its generalisation of the data and start overfitting. To find the latent space size with best trade-off, networks with a variety of latent space sizes are trained. Their loss values correspond directly to the quality of the reconstructions they achieve and are therefore an indirect measurement of how successful the latent spaces are in preserving information from the original data. The losses during training of these networks is shown in Figure 5.5. As can be seen in the network training converges after a latent space of size 8. This suggests that 8 dimensions in the latent space are just enough to encompass all the needed information from the data, and are most likely to result in the best generalisation of the data. Larger latent spaces do not bring reconstruction improvements and merely contain the same information within a larger latent space, going away from the best generalisation of the data.

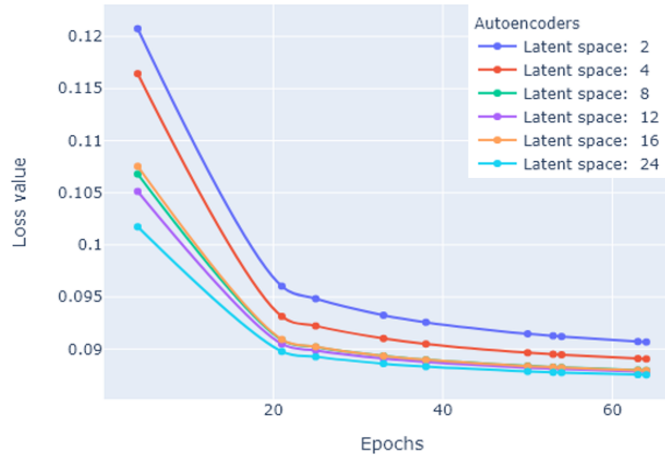


Figure 5.5: Training loss of autoencoders with different latent space sizes. The AE architecture between the separate training sessions stays the same, but the dimensionality of the latent space is varied between 2- and 24-dimensional. While the 2- and 4-dimensional AE variations even out at a higher loss, the variations with 8 dimensions and above converge around the same reconstruction loss.

5.4.2 Latent space structure

The CBLEED patterns in the data have been generated by traversing two physical parameters - the beam energy and the dimer displacement, with a step of 1 eV and 0.1 Å respectively. Note that the beam energy is usually a known variable during an experiment, but is kept as a parameter to showcase the ability of the proposed algorithm to generalise multiple physical parameters simultaneously without prior knowledge of them. Hence, the two parameters used for the generations can be considered metadata, which is not accessible to the AE algorithm at any time. In order to explore the effectiveness of the latent space generalisation of the CBLEED data, we visualise the projections of each CBLEED pattern in the latent space, labelled with its beam energy and dimer displacement parameters. The smallest examined latent space consists of 2 dimensions and is shown in Figure 5.6, after model training.

It is apparent from the distribution observed over this two-dimensional latent space that both the beam energy and dimer displacement are reasonably well represented, with only a few inconsistencies of the dimer displacement parameter projection in the low-beam energy region of the latent space cluster. On the other hand, the well-defined structure of the optimal 8 node latent space is clearly visible, as shown in Figure 5.7. This suggests the autoencoder latent space learns a good generalisation of the data that ultimately leads back to the initial data generation process, without any prior knowledge of it.

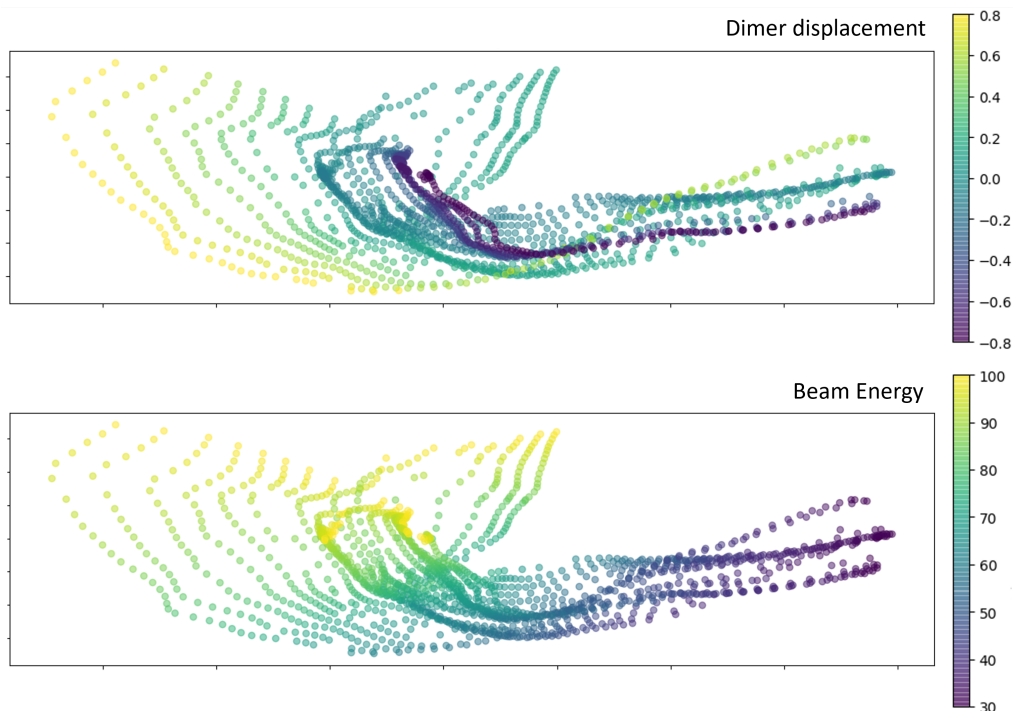


Figure 5.6: Latent space structure of the 2-dimensional autoencoder architecture after training. The continuous distribution of dimer displacements and beam energies indicates a good generalisation of the data. Small inconsistencies in the representations of the higher values of dimer displacements are visible as non-blending placements of the yellow and purple lines in the overall latent structure.

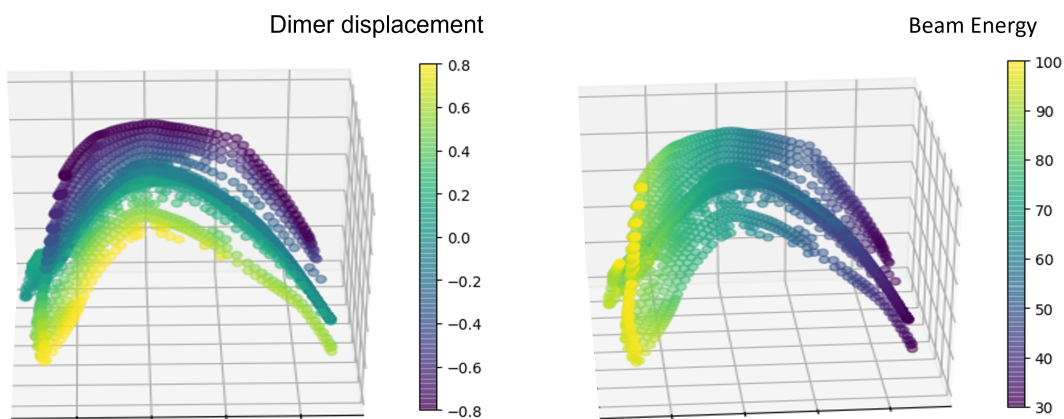


Figure 5.7: Latent space structure of the 8-dimensional autoencoder architecture after training. Hessian Locally Linear Embedding (Donoho & Grimes, 2003) is used for dimensionality reduction to three dimensions while preserving the latent space structure. Produced with a testing subset of the dataset that has not been used for training.

Algorithm	Beam Energy		Dimer Displ.	
	MAE	R^2	MAE	R^2
KNN	0.43	0.999	0.025	0.992
RBF SVM	0.83	0.995	0.050	0.978
NuSVM	0.92	0.994	0.010	0.997
DecisionTree	0.85	0.995	0.024	0.980
ExtraTree	0.87	0.997	0.028	0.973
XGBoost	0.75	0.998	0.028	0.986

Table 5.1: Comparison of the predictive success of different ML algorithms. Trained and tested on the latent space projections of the training and testing subsets of the dataset, respectively.

5.4.3 Latent Space Parameter Extraction

We use the trained and structured latent space to extract the parameters of the surface via transfer learning. Several regression approaches, such as nearest neighbours, support vector machines, decision trees and ensembles, were benchmarked, and the most successful algorithms are presented in Table 5.1. Their accuracy was measured by the average MAE on the latent representations of a test set of simulated CBLEED patterns, and the robustness of the methods is measured through the Coefficient of Determination (R^2) metric. The R^2 metric is a measure of how well unseen examples are likely to be predicted by the model by relating variances in the predictions to variations in the initial inputs. In particular, it is an indication of how predictive the latent representation placements of the CBLEED patterns are for the regression model, and as a consequence - how well new points in the latent space can be quantified.

The methods show a sensitivity of less than 1 eV in predicting the beam energy and less than 0.1 Å with high robustness. The K-nearest Neighbours (KNN) algorithm showed the best robustness and a mean error of 0.043 eV in predicting the Beam Energy in the test examples. The Nu Support Vector Machine (NuSVM) Regression had the best dimer displacement prediction accuracy with a mean error of just 0.01 Å, going well into the sub-angstrom levels of sensitivity.

5.4.4 Performance

Training the AE network takes around 1.5h on an RTX-3080 Laptop GPU and an i9-11900H CPU machine. Inference from the full pipeline includes a pass of the encoder network to project the image into latent space, and a pass on the regression network to quantify the point. It takes 0.1 sec, giving a performance of 10 fps. This performance suggests a quick enough execution time for continuous local inference on a standard lab computer for a real-time structure estimation feed, and alternatively enables instant inference on-demand during an experiment. The performance points towards the suitability of such an algorithm to be trained in advance for an experiment, and be used both in real-time during the experimental run, and after it, to point towards the appropriate structures and enable their confirmation with a single simulations run, rather than a full lengthy exploration of all possibilities in the simulation parameters.

5.5 Conclusion

A DCAE network was developed and trained on simulated CBLEED patterns, generated with sub-angstrom dimer displacements. The network was shown to be able to generalise the data well with only an 8-dimensional latent space. The well-defined and explainable structure of the latent space is able to learn and identify key physical surface properties and parameters based on the observed CBLEED pattern. The latent space projection of a CBLEED pattern is used to estimate both the beam energy and dimer displacements with high accuracy through a secondary ML algorithm, showcasing the ability of the approach to capture multiple parameters at once. With that, the approach is able to provide means of quick and efficient interpretation of a CBLEED pattern, providing a basis for experimental tools for real-time surface structure determination through the CBLEED technique.

5.6 Future Work

This work demonstrates the idea of analysing CBLEED patterns on a *Proof of Concept* level, and further steps can be taken to bring the concept to reality.

- **Covering all training strategies.** Since we utilise an ensemble of algorithms working together, a further optimisation of the models lies in exploring different training strategies, such as fine-tuning, joint learning and two-stage training.
- **Including other materials.** Expanding the dataset with a variety of materials will bring further generalisation of the CBLEED patterns in the AE models.
- **Including more structural parameters.** A wider range of variables in the dataset generalisation will explore the limits of the technique and expand it to more complex structures.
- **Testing on experimental data.** Even though the initial concept has been shown to be effective, a real measure of how useful such a model is can be done by testing its performance on experimental data.

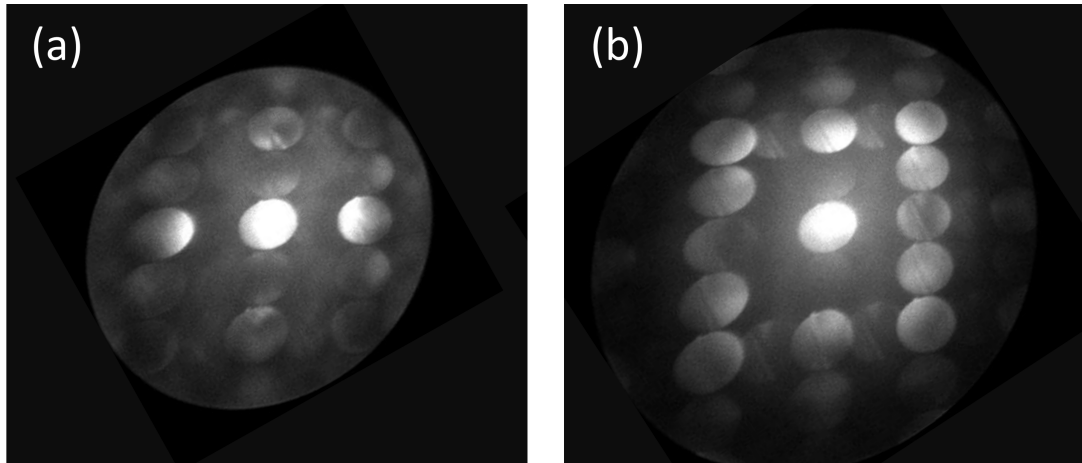


Figure 5.8: Experimental CBLEED patterns. Taken on Si(001) on a $(2 \times 1) / (1 \times 2)$ reconstructed surface, with a beam energies of (a) 30 eV and (b) 50 eV. Taken by adjusting the *CL3* lens of the LEEM microscope until beam is convergent. Images taken by Y.R.Niu.

Chapter 6

Conclusion

With this thesis, we covered fundamental questions of phase interactions during a stable coexistence and growth in the context of the Ga-rich (6×6) and $c(8 \times 2)$ at high temperatures. We demonstrated the ability of the presented models to explain the observed phenomena and extract surface parameters. To achieve this, we developed Computer Vision (CV) pipelines to process the data automatically and with high precision. With that, we extracted the values of the relevant surface parameters behind the models, governing the observed processes. Furthermore, we showed the application of Deep Learning (DL) to extract information from abstract diffraction pattern data in real time.

In the first study we presented, the stable (6×6) and $c(8 \times 2)$ phase coexistence was described. We combined the two approaches of observing phase coexistence variations and measuring boundary fluctuations to establish an end-to-end method of extracting the entropy difference and stress difference between the two phases with a single experiment. We developed a complex CV and computational pipeline to facilitate the data analysis and estimate the two fundamental parameters.

In the second work presented, we observe the metastable phase coexistence between the (6×6) and $c(8 \times 2)$ phases during growth. By using the chemical potential gradient provided by a Ga droplet, we create an experimental setup where we gather data for the metastability in a spectrum of conditions. We develop a model to describe the surface behaviour at this range of chemical potential variations. We set up a CV pipeline to extract the rich metastability data from the experimental images automatically and accurately. The metastability data showed that the developed

model describes the surface behaviour accordingly.

In the final work of the thesis, we showcased the ability of a DL approach to analyse Convergent Beam Low-Energy Electron Diffraction (CBLEED) patterns and connect them with the surface structure they result from. We construct an unsupervised convolutional autoencoder to learn a compressed representation of the data and capture its essential features. The compressed space of the trained algorithm was then shown to be well-structured and interpretable by traditional Machine Learning (ML) algorithms, which are used to extract the surface structure parameters that produced the CBLEED pattern with sub-angstrom accuracy. The inference on this ensemble of algorithms was shown to be quick enough to be comfortably used in real time.

The author's studentship was funded by EPSRC research Grant No. EP/R513003/1.

Bibliography

- Abadi, M., Barham, P., Chen, J., Chen, Z., Davis, A., Dean, J., Devin, M., Ghemawat, S. G. I., Isard, M., Kudlur, M., Levenberg, J., Monga, R., Moore, S., Murray, D. G., Steiner, B., Tucker, P., Vasudevan, V., Pete Warden, M. W., Yu, Y., & Zheng, X. (2016). TensorFlow: A System for Large-Scale Machine Learning. *12th USENIX Symposium on Operating Systems Design and Implementation OSDI16*, 265–283. <https://doi.org/10.48550/arXiv.1605.08695> (cit. on p. 47)
- Aguiar, J. A., Gong, M. L., Unocic, R. R., Tasdizen, T., & Miller, B. D. (2019). Decoding crystallography from high-resolution electron imaging and diffraction datasets with deep learning. *Science Advances*, 5(10), 1–10. <https://doi.org/10.1126/sciadv.aaw1949> (cit. on p. 44)
- Akers, S., Kautz, E., Trevino-Gavito, A., Olszta, M., Matthews, B. E., Wang, L., Du, Y., & Spurgeon, S. R. (2021). Rapid and flexible segmentation of electron microscopy data using few-shot machine learning. *npj Computational Materials*, 7(1). <https://doi.org/10.1038/s41524-021-00652-z> (cit. on p. 44)
- Alerhand, O. L., Vanderbilt, D., Meade, R. D., & Joannopoulos, J. D. (1988). Spontaneous formation of stress domains on crystal surfaces. *Physical Review Letters*, 61(17), 1973–1976. <https://doi.org/10.1103/PhysRevLett.61.1973> (cit. on p. 19)
- Alex, K., Sutskever, I., & Hinton, G. E. (2012). ImageNet Classification with Deep Convolutional Neural Networks. *NIPS’12: Proceedings of the 25th International Conference on Neural Information Processing Systems*, 1, 1097–1105. <https://doi.org/10.5555/2999134.2999257> (cit. on p. 50)

- Alfonso, C., Bermond, J., Heyraud, J., & Métois, J. (1992). The meandering of steps and the terrace width distribution on clean Si(111). *Surface Science*, 262(3), 371–381. [https://doi.org/10.1016/0039-6028\(92\)90133-q](https://doi.org/10.1016/0039-6028(92)90133-q) (cit. on pp. 55, 71)
- Altman, M. S. (2010). Trends in low energy electron microscopy. *Journal of Physics Condensed Matter*, 22(8). <https://doi.org/10.1088/0953-8984/22/8/084017> (cit. on pp. 34, 35, 97)
- Altman, M. S., Chung, W. F., & Liu, C. H. (1998). LEEM phase contrast. *Surface Review and Letters*, 5(6), 1129–1141. <https://doi.org/10.1142/S0218625X98001468> (cit. on p. 29)
- Anscombe, F. J. (1948). The Transformation of Poisson, Binomial and Negative-Binomial Data. *Biometrika*, 35(3/4), 246. <https://doi.org/10.2307/2332343> (cit. on p. 73)
- Apicella, A., Donnarumma, F., Isgrò, F., & Prevete, R. (2021). A survey on modern trainable activation functions. *Neural Networks*, 138, 14–32. <https://doi.org/10.1016/j.neunet.2021.01.026> (cit. on p. 48)
- Bartelt, N., Theis, W., & Tromp, R. (1996). Ostwald ripening of two-dimensional islands on Si(001). *Physical Review B - Condensed Matter and Materials Physics*, 54(16), 11741–11751. <https://doi.org/10.1103/PhysRevB.54.11741> (cit. on pp. 65, 69, 71)
- Bartelt, N. C., Einstein, T. L., & Williams, E. D. (1990). The influence of step-step interactions on step wandering. *Surface Science*, 240(1-3). [https://doi.org/10.1016/0039-6028\(90\)90722-K](https://doi.org/10.1016/0039-6028(90)90722-K) (cit. on p. 23)
- Bartelt, N. C., Goldberg, J. L., Einstein, T. L., & Williams, E. D. (1992). The equilibration of terrace width distributions on stepped surfaces. *Surface Science*, 273(1-2), 252–260. [https://doi.org/10.1016/0039-6028\(92\)90290-M](https://doi.org/10.1016/0039-6028(92)90290-M) (cit. on pp. 22, 23, 55)
- Bartelt, N. C., Goldberg, J. L., Einstein, T. L., Williams, E. D., Heyraud, J. C., & Métois, J. J. (1993). Brownian motion of steps on Si(111). *Physical Review B*, 48(20), 15453–15457. <https://doi.org/10.1103/PhysRevB.48.15453> (cit. on pp. 71, 73)

- Bauer, E. (2014). *Surface microscopy with low energy electrons*. Springer-Verlag New York. <https://doi.org/10.1007/978-1-4939-0935-3>. (Cit. on pp. 26, 29, 34, 57)
- Bird, D. M., & Saunders, M. (1992). Sensitivity and accuracy of CBED pattern matching. *Ultramicroscopy*, 45(2), 241–251. [https://doi.org/10.1016/0304-3991\(92\)90512-I](https://doi.org/10.1016/0304-3991(92)90512-I) (cit. on p. 97)
- Bradski, G., & Kaehler, A. (2008). *Learning OpenCV*. <http://shop.oreilly.com/product/0636920022497.do>. (Cit. on p. 37)
- Briechele, K., & Hanebeck, U. D. (2001). Template matching using fast normalized cross correlation. *Optical Pattern Recognition XII*, 4387(March 2001), 95–102. <https://doi.org/10.1117/12.421129> (cit. on p. 38)
- Buxton, B. F., Eades, J. A., Steeds, J. W., & Rackham, G. M. (1976). The symmetry of electron diffraction zone axis patterns. *Philosophical Transactions of the Royal Society of London. Series A, Mathematical and Physical Sciences*, 281(1301), 171–194. <https://doi.org/https://doi.org/10.1098/rsta.1976.0024> (cit. on p. 97)
- Campbell, B. D., Hu, X., & Higgins, S. R. (2009). A computer program for automated step edge motion analysis from scanning probe microscopy images. *Surface Science*, 603(7), 1034–1040. <https://doi.org/10.1016/j.susc.2009.02.020> (cit. on p. 71)
- Canny, J. (1986). A Computational Approach to Edge Detection. *IEEE Transactions on Pattern Analysis and Machine Intelligence*, PAMI-8(6), 679–698. <https://doi.org/10.1109/TPAMI.1986.4767851> (cit. on pp. 43, 60)
- Clément, L., Pantel, R., Kwakman, L. F., & Rouvière, J. L. (2004). Strain measurements by convergent-beam electron diffraction: The importance of stress relaxation in lamella preparations. *Applied Physics Letters*, 85(4), 651–653. <https://doi.org/10.1063/1.1774275> (cit. on p. 97)
- Cohen, S. D., Schroll, R. D., Einstein, T. L., Métois, J. J., Gebremariam, H., Richards, H. L., & Williams, E. D. (2002). Si(111) step fluctuations at high temperature: Anomalous step-step repulsion. *Physical Review B - Condensed Matter and Materials Physics*, 66(11), 1153101–1153106. <https://doi.org/10.1103/PhysRevB.66.115310> (cit. on p. 71)

- Constantinou, P. C., & Jesson, D. E. (2019). On the sensitivity of convergent beam low energy electron diffraction patterns to small atomic displacements. *Applied Surface Science*, 489(January), 504–509. <https://doi.org/10.1016/j.apsusc.2019.05.274> (cit. on pp. 98–100)
- de Jong, T. A., Kok, D. N., van der Torren, A. J., Schopmans, H., Tromp, R. M., van der Molen, S. J., & Jobst, J. (2020). Quantitative analysis of spectroscopic low energy electron microscopy data: High-dynamic range imaging, drift correction and cluster analysis. *Ultramicroscopy*, 213. <https://doi.org/10.1016/j.ultramic.2019.112913> (cit. on pp. 37, 73)
- Devernay, F. (1995). A Non-Maxima Suppression Method for Edge Detection with Sub-Pixel Accuracy. *INRIA Research Report*, 2724 (cit. on pp. 60, 74).
- Donoho, D. L., & Grimes, C. (2003). Hessian eigenmaps: Locally linear embedding techniques for high-dimensional data. *Proceedings of the National Academy of Sciences of the United States of America*, 100(10), 5591–5596. <https://doi.org/10.1073/pnas.1031596100> (cit. on p. 105)
- Ede, J. M. (2021a). Advances in Electron Microscopy with Deep Learning. (February). <https://doi.org/10.5281/zenodo.4399748> (cit. on p. 43)
- Ede, J. M. (2021b). Deep learning in electron microscopy. *Machine Learning: Science and Technology*, 2(1). <https://doi.org/10.1088/2632-2153/abd614> (cit. on pp. 46, 99)
- Flege, J. I., & Krasovskii, E. E. (2014). Intensity-voltage low-energy electron microscopy for functional materials characterization. *Physica Status Solidi - Rapid Research Letters*, 8(6), 463–477. <https://doi.org/10.1002/pssr.201409102> (cit. on p. 29)
- Flege, J. I., Tang, W.-X., & Altman, M. S. (2012). Low-energy electron microscopy. *In Characterization of Materials*, E.N. Kaufmann (Ed.), 1808–1826. <https://doi.org/10.1002/0471266965.com157> (cit. on pp. 29, 34)
- Freitas, R., Frolov, T., & Asta, M. (2017). Capillary fluctuations of surface steps: An atomistic simulation study for the model Cu(111) system. *Physical Review E*, 96(4), 1–10. <https://doi.org/10.1103/PhysRevE.96.043308> (cit. on p. 71)
- Galitsyn, Y. G., Dmitriev, D. V., Mansurov, V. G., Moshchenko, S. P., & Toropov, A. I. (2007). Asymmetric $c(4\times 4) \rightarrow \gamma(2\times 4)$ reconstruction phase transition

- on the (001)GaAs surface. *JETP Letters*, 84(9), 505–508. <https://doi.org/10.1134/S0021364006210089> (cit. on p. 18)
- Goodfellow, I., Pouget-Abadie, J., Mirza, M., Xu, B., Warde-Farley, D., Ozair, S., Courville, A., & Bengio, Y. (2014). Generative adversarial networks. *Communications of the ACM*. <https://doi.org/10.1145/3422622> (cit. on p. 52)
- Goodman, P. (1975). A practical method of three-dimensional space-group analysis using convergent-beam electron diffraction. *Acta Crystallographica Section A*, 31(6), 804–810. <https://doi.org/10.1107/S0567739475001738> (cit. on p. 97)
- Goyal, B., Dogra, A., Agrawal, S., Sohi, B. S., & Sharma, A. (2020). Image denoising review: From classical to state-of-the-art approaches. *Information Fusion*, 55(September 2019), 220–244. <https://doi.org/10.1016/j.inffus.2019.09.003> (cit. on p. 73)
- Grompone Von Gioi, R., & Randall, G. (2017). A sub-pixel edge detector: An implementation of the canny/devernay algorithm. *Image Processing On Line*, 7, 347–372. <https://doi.org/10.5201/ipol.2017.216> (cit. on p. 76)
- Hannikainen, K., Gomez, D., Pereiro, J., Niu, Y. R., & Jesson, D. E. (2019). Surface Phase Metastability during Langmuir Evaporation. *Physical Review Letters*, 123(18), 186102. <https://doi.org/10.1103/PhysRevLett.123.186102> (cit. on pp. 12, 17, 24, 56, 58)
- Hannon, J. B., Meyer zu Heringdorf, F. J., Tersoff, J., & Tromp, R. M. (2001). Phase coexistence during surface phase transitions. *Physical Review Letters*, 86(21), 4871–4874. <https://doi.org/10.1103/PhysRevLett.86.4871> (cit. on pp. 21, 55, 63, 64, 68)
- Hannon, J. B., Tersoff, J., & Tromp, R. M. (2002). Surface stress and thermodynamic nanoscale size selection. *Science*, 295(5553), 299–301. <https://doi.org/10.1126/science.1066420> (cit. on p. 18)
- Hannon, J. B., & Tromp, R. M. (2001). Phase boundary fluctuations on Si(111). *Journal of Vacuum Science & Technology A: Vacuum, Surfaces, and Films*, 19(5), 2596–2600. <https://doi.org/10.1116/1.1397464> (cit. on pp. 22, 65, 69, 71, 73)

- Hannon, J. B., & Tromp, R. M. (2003). Low-Energy Electron Microscopy of Surface Phase Transitions. *Annual Review of Materials Research*, 33(1), 263–288. <https://doi.org/10.1146/annurev.matsci.33.121901.111743> (cit. on pp. 12, 22, 54, 62, 64, 84)
- He, K., Zhang, X., Ren, S., & Sun, J. (2015). Deep Residual Learning for Image Recognition. *arXiv*. <https://doi.org/arXiv:1512.03385v1> (cit. on p. 51)
- Held, G., Wander, A., & King, D. A. (1995). Variations of LEED intensities with angle of incidence and the influence on spot profiles. *Physical Review B*, 51(24), 17856–17866. <https://doi.org/10.1103/PhysRevB.51.17856> (cit. on p. 97)
- Hibino, H., Homma, Y., Hu, C.-W., Uwaha, M., Ogino, T., & Tsong, I. (2004). Structural and morphological changes on surfaces with multiple phases studied by low-energy electron microscopy. *Applied Surface Science*, 237(1-4), 51–57. <https://doi.org/10.1016/j.apsusc.2004.06.047> (cit. on p. 18)
- Hove, M. V., & Moritz, W. (2022). LEED Theory. *Surface structure determination by leed and x-rays* (pp. 110–187). <https://doi.org/10.1017/9781108284578.007>. (Cit. on p. 29)
- Ibach, H. (1997). The role of surface stress in reconstruction, epitaxial growth and stabilization of mesoscopic structures. *Surface Science Reports*, 29(5-6), 195–263. [https://doi.org/10.1016/s0167-5729\(97\)00010-1](https://doi.org/10.1016/s0167-5729(97)00010-1) (cit. on p. 54)
- Ioffe, S., & Szegedy, C. (2015). Batch normalization: Accelerating deep network training by reducing internal covariate shift. *32nd International Conference on Machine Learning, ICML 2015*, 1, 448–456. <https://doi.org/10.48550/arXiv.1502.03167> (cit. on p. 49)
- Ivanov, T., Kumar, A., Sharoukhov, D., Ortega, F. A., & Putman, M. (2020). Deep-Focus: A deep learning model for focusing microscope systems. *1151103*(August 2020), 2. <https://doi.org/10.1117/12.2568990> (cit. on p. 44)
- J. P. Lewis. (1995). Fast normalized cross-correlation for template matching. *Industrial Light & Magic*, 120–123 (cit. on p. 38).
- J.A.Eades. (1986). Convergent-beam techniques in transmission electron microscopy. *Applied Surface Science*, 26(3), 280–293. [https://doi.org/https://doi.org/10.1016/0169-4332\(86\)90069-3](https://doi.org/https://doi.org/10.1016/0169-4332(86)90069-3) (cit. on p. 97)

- Jain, P., & Tyagi, V. (2016). A survey of edge-preserving image denoising methods. *Information Systems Frontiers*, 18(1), 159–170. <https://doi.org/10.1007/s10796-014-9527-0> (cit. on pp. 60, 73)
- Janett, G., Steiner, O., Alsina Ballester, E., Belluzzi, L., & Mishra, S. (2019). A novel fourth-order WENO interpolation technique. *Astronomy & Astrophysics*, 624, A104. <https://doi.org/10.1051/0004-6361/201834761> (cit. on pp. 61, 79)
- Jeong, H.-C., & Williams, E. D. (1999). Steps on surfaces: experiment and theory. 57(6-7), 544–556. <https://doi.org/10.1515/zna-2002-6-747> (cit. on p. 22)
- J.M. Zuo. (1998). Quantitative convergent beam electron diffraction. *Materials transactions, JIM*, 39(9), 938–946. <https://doi.org/https://doi.org/10.2320/matertrans1989.39.938> (cit. on p. 97)
- Joyce, B. A., & Vvedensky, D. D. (2004). Self-organized growth on GaAs surfaces. *Materials Science and Engineering R: Reports*, 46(6), 127–176. <https://doi.org/10.1016/j.mser.2004.10.001> (cit. on pp. 54, 81)
- Kato, H., Miyamoto, K., Sano, M., & Yao, T. (2004). Polarity control of ZnO on sapphire by varying the MgO buffer layer thickness. *Applied Physics Letters*, 84(22), 4562–4564. <https://doi.org/10.1063/1.1759377> (cit. on p. 97)
- Kaufmann, K., Zhu, C., Rosengarten, A. S., Maryanovsky, D., Harrington, T. J., Marin, E., & Vecchio, K. S. (2020). Crystal symmetry determination in electron diffraction using machine learning. *Science*, 367(6477), 564–568. <https://doi.org/10.1126/science.aay3062> (cit. on p. 99)
- Kern, K., Niehus, H., Schatz, A., Zeppenfeld, P., Goerge, J., & Comsa, G. (1991). Long-Range Spatial Self-Organization in the Adsorbate-Induced Restructuring of Surfaces: Cu{110}-(2 x 1)0. *Physical Review Letters*, 67(7), 855–858. <https://doi.org/10.1103/PhysRevLett.67.855> (cit. on p. 18)
- Kingma, D. P., & Ba, J. L. (2015). Adam: A method for stochastic optimization. *3rd International Conference on Learning Representations, ICLR 2015 - Conference Track Proceedings*, 1–15. <https://doi.org/10.48550/arXiv.1412.6980> (cit. on p. 47)
- Kocán, P., Ohtake, A., & Koguchi, N. (2004). Structural features of Ga-rich GaAs(001) surfaces: Scanning tunneling microscopy study. *Physical Review B - Con-*

- Condensed Matter and Materials Physics*, 70(20), 4–7. <https://doi.org/10.1103/PhysRevB.70.201303> (cit. on p. 56)
- Koho, S., Fazeli, E., Eriksson, J. E., & Hänninen, P. E. (2016). Image Quality Ranking Method for Microscopy. *Scientific Reports*, 6, 1–15. <https://doi.org/10.1038/srep28962> (cit. on p. 44)
- Krasovskii, E. E. (2004). Augmented-plane-wave approach to scattering of Bloch electrons by an interface. *Physical Review B - Condensed Matter and Materials Physics*, 70(24), 1–11. <https://doi.org/10.1103/PhysRevB.70.245322> (cit. on p. 29)
- Krull, A., Hirsch, P., Rother, C., Schiffrin, A., & Krull, C. (2020). Artificial-intelligence-driven scanning probe microscopy. *Communications Physics*, 3(1), 1–8. <https://doi.org/10.1038/s42005-020-0317-3> (cit. on p. 44)
- Krzyzewski, T. J., & Jones, T. S. (2008). Nanostructure formation in InAs/InP(001) heteroepitaxy: Importance of surface reconstruction. *Physical Review B - Condensed Matter and Materials Physics*, 78(15), 1–8. <https://doi.org/10.1103/PhysRevB.78.155307> (cit. on pp. 10, 54)
- Kuball, M., Wang, D. T., Esser, N., Cardona, M., Zegenhagen, J., & Fimland, B. (1995). Microscopic structure of the GaAs(001)-(6x6) surface derived from scanning tunneling microscopy. *Physical Review B*, 51(19), 13880–13882. <https://doi.org/10.1103/PhysRevB.51.13880> (cit. on p. 56)
- Kwoen, J., & Arakawa, Y. (2020). Classification of Reflection High-Energy Electron Diffraction Pattern Using Machine Learning. *Crystal Growth and Design*, 20(8), 5289–5293. <https://doi.org/10.1021/acs.cgd.0c00506> (cit. on p. 99)
- Kwoen, J., & Arakawa, Y. (2022). Multiclass classification of reflection high-energy electron diffraction patterns using deep learning. *Journal of Crystal Growth*, 593(December 2021), 126780. <https://doi.org/10.1016/j.jcrysgro.2022.126780> (cit. on p. 99)
- LaBella, V. P., Krause, M. R., Ding, Z., & Thibado, P. M. (2005). Arsenic-rich GaAs(0 0 1) surface structure. *Surface Science Reports*, 60(1-4), 1–53. <https://doi.org/10.1016/j.surfrep.2005.10.001> (cit. on p. 55)

- Lazić, I., Bosch, E. G., & Lazar, S. (2016). Phase contrast STEM for thin samples: Integrated differential phase contrast. *Ultramicroscopy*, 160, 265–280. <https://doi.org/10.1016/j.ultramic.2015.10.011> (cit. on p. 97)
- LeBeau, J. M., Findlay, S. D., Allen, L. J., & Stemmer, S. (2010). Position averaged convergent beam electron diffraction: Theory and applications. *Ultramicroscopy*, 110(2), 118–125. <https://doi.org/10.1016/j.ultramic.2009.10.001> (cit. on p. 97)
- Lee, B. D., Lee, J.-W., Park, W. B., Park, J., Cho, M.-Y., Pal Singh, S., Pyo, M., & Sohn, K.-S. (2022). Powder X-Ray Diffraction Pattern Is All You Need for Machine-Learning-Based Symmetry Identification and Property Prediction. *Advanced Intelligent Systems*, 4(7), 2200042. <https://doi.org/10.1002/aisy.202200042> (cit. on p. 100)
- Lee, J. W., Park, W. B., Lee, J. H., Singh, S. P., & Sohn, K. S. (2020). A deep-learning technique for phase identification in multiphase inorganic compounds using synthetic XRD powder patterns. *Nature Communications*, 11(1), 1–11. <https://doi.org/10.1038/s41467-019-13749-3> (cit. on p. 99)
- Lv, J., Zhang, H., Zhang, D., Liu, L., & Han, Y. (2022). Low-Dose Electron Microscopy Imaging of Electron Beam-Sensitive Crystalline Materials. *Accounts of Materials Research*, 3(5), 552–564. <https://doi.org/10.1021/accountsmr.2c00008> (cit. on p. 97)
- Mäkitalo, M., & Foi, A. (2013). Optimal inversion of the generalized anscombe transformation for Poisson-Gaussian noise. *IEEE Transactions on Image Processing*, 22(1), 91–103. <https://doi.org/10.1109/TIP.2012.2202675> (cit. on p. 73)
- Marchenko, V. (1981). Possible structures and phase transitions on the surface of crystals. *JETP Letters*, 33, 381. <https://ui.adsabs.harvard.edu/abs/1981JETPL..33..381M> (cit. on p. 17)
- Martineau, B. H., Johnstone, D. N., van Helvoort, A. T., Midgley, P. A., & Eggeman, A. S. (2019). Unsupervised machine learning applied to scanning precession electron diffraction data. *Advanced Structural and Chemical Imaging*, 5(1). <https://doi.org/10.1186/s40679-019-0063-3> (cit. on p. 99)

- Masia, F., Langbein, W., Fischer, S., Krisponeit, J.-O., & Falta, J. (2022). Low-energy electron microscopy intensity-voltage data – factorization, sparse sampling, and classification, 1–13. <http://arxiv.org/abs/2203.12353> (cit. on p. 34)
- McLean, J. G., Kruse, P., & Kummel, A. C. (1999). Atomic structure determination for GaAs(001)-(6x6) by STM. *Surface Science*, 424(2), 206–218. [https://doi.org/10.1016/S0039-6028\(98\)00939-X](https://doi.org/10.1016/S0039-6028(98)00939-X) (cit. on p. 56)
- Men, F., Packard, W., & Webb, M. (1988). Si(100) Surface under an Externally Applied Stress. *Physical Review Letters*, 61(21), 2469–2471. <https://doi.org/https://doi.org/10.1103/PhysRevLett.61.2469> (cit. on p. 18)
- Meng, Y., Zhang, Z., Yin, H., & Ma, T. (2018). Automatic detection of particle size distribution by image analysis based on local adaptive canny edge detection and modified circular Hough transform. *Micron*, 106(December 2017), 34–41. <https://doi.org/10.1016/j.micron.2017.12.002> (cit. on p. 71)
- Mueller, T., Kusne, A., & Ramprasad, R. (2016). Machine Learning In Materials Science: Recent Progress And Emerging Applications. *Reviews in Computational Chemistry*, 29(1) (cit. on p. 44).
- Müller, P., & Saúl, A. (2004). Elastic effects on surface physics. *Surface Science Reports*, 54(5-8), 157–258. <https://doi.org/10.1016/j.surfrep.2004.05.001> (cit. on p. 20)
- Neave, J. H., Joyce, B. A., & Dobson, P. J. (1984). Dynamic RHEED observations of the MBE growth of GaAs - Substrate temperature and beam azimuth effects. *Applied Physics A Solids and Surfaces*, 34(3), 179–184. <https://doi.org/10.1007/BF00616915> (cit. on p. 81)
- Ng, K.-O., & Vanderbilt, D. (1995). Stability of periodic domain structures in a two-dimensional dipolar model. *Physical Review B*, 52(3), 2177–2183. <https://doi.org/https://doi.org/10.1103/PhysRevB.52.2177> (cit. on p. 25)
- Niu, Y. R., Pereiro, J., Gomez, D., & Jesson, D. E. (2019). Selected energy dark-field imaging using low energy electrons for optimal surface phase discrimination. *Ultramicroscopy*, 200, 79–83. <https://doi.org/10.1016/j.ultramic.2019.02.017> (cit. on pp. 16, 33, 56, 57)

- Ohtake, A. (2007). Structure and composition of Ga-rich (6x6) reconstructions on GaAs(001). *Physical Review B - Condensed Matter and Materials Physics*, 75(15), 4–7. <https://doi.org/10.1103/PhysRevB.75.153302> (cit. on pp. 11, 16, 55, 56)
- Ohtake, A. (2008). Surface reconstructions on GaAs(001). *Surface Science Reports*, 63(7), 295–327. <https://doi.org/10.1016/j.surfrep.2008.03.001> (cit. on pp. 11, 15–17, 55)
- Ohtake, A., Hagiwara, A., & Nakamura, J. (2013). Controlled incorporation of Mn in GaAs: Role of surface reconstructions. *Physical Review B - Condensed Matter and Materials Physics*, 87(16), 1–5. <https://doi.org/10.1103/PhysRevB.87.165301> (cit. on pp. 11, 54, 82)
- Ohtake, A., Mano, T., Hagiwara, A., & Nakamura, J. (2014). Self-assembled growth of Ga droplets on GaAs(001): Role of surface reconstructions. *Crystal Growth and Design*, 14(6), 3110–3115. <https://doi.org/10.1021/cg500355f> (cit. on pp. 11, 54, 82)
- Ondrejcek, M., Swiech, W., Durfee, C. S., & Flynn, C. P. (2003). Step fluctuations and step interactions on Mo(0 1 1). *Surface Science*, 541(1-3), 31–45. [https://doi.org/10.1016/S0039-6028\(03\)00745-3](https://doi.org/10.1016/S0039-6028(03)00745-3) (cit. on pp. 22, 71)
- Ondrejcek, M., Swiech, W., Rajappan, M., & Flynn, C. P. (2005). Fluctuation spectroscopy of step edges on Pt(111) and Pd(111). *Physical Review B - Condensed Matter and Materials Physics*, 72(8), 1–12. <https://doi.org/10.1103/PhysRevB.72.085422> (cit. on pp. 22, 71)
- Ondrejcek, M., Swiech, W., Yang, G., & Flynn, C. P. (2002). Low energy electron microscopy studies of steps on single crystal thin films of refractory metals. *Journal of Vacuum Science and Technology B: Microelectronics and Nanometer Structures*, 20(6), 2473–2477. <https://doi.org/10.1116/1.1521958> (cit. on p. 22)
- Ondrejcek, M., Swiech, W., Yang, G., & Flynn, C. P. (2004). Crossover from bulk to surface diffusion in the fluctuations of step edges on Pt(111). *Philosophical Magazine Letters*, 84(2), 69–77. <https://doi.org/10.1080/09500830310001646671> (cit. on pp. 22, 71)

- Orton, J., & Foxon, T. (2015). *Molecular Beam Epitaxy: A Short History*. Oxford university Press. (Cit. on pp. 55, 81).
- Otsu, N. (1979). A Threshold Selection Method from Gray-Level Histograms. *IEEE Transactions on Systems, Man, and Cybernetics*, 9(1), 62–66. <https://doi.org/10.1109/TSMC.1979.4310076> (cit. on p. 42)
- Oviedo, F., Ren, Z., Sun, S., Settens, C., Liu, Z., Hartono, N. T. P., Ramasamy, S., DeCost, B. L., Tian, S. I., Romano, G., Gilad Kusne, A., & Buonassisi, T. (2019). Fast and interpretable classification of small X-ray diffraction datasets using data augmentation and deep neural networks. *npj Computational Materials*, 5(1), 1–9. <https://doi.org/10.1038/s41524-019-0196-x> (cit. on p. 99)
- Pang, A. B., Man, K. L., Altman, M. S., Stasevich, T. J., Szalma, F., & Einstein, T. L. (2008). Step line tension and step morphological evolution on the Si(111) (1x1) surface. *Physical Review B - Condensed Matter and Materials Physics*, 77(11), 1–12. <https://doi.org/10.1103/PhysRevB.77.115424> (cit. on p. 71)
- Pang, A. B., Müller, T., Altman, M. S., & Bauer, E. (2009). Fourier optics of image formation in LEEM. *Journal of Physics Condensed Matter*, 21(31). <https://doi.org/10.1088/0953-8984/21/31/314006> (cit. on p. 34)
- Paszke, A., Gross, S., Massa, F., Lerer, A., Bradbury Google, J., Chanan, G., Killeen, T., Lin, Z., Gimelshein, N., Antiga, L., Desmaison, A., Xamla, A. K., Yang, E., Devito, Z., Raison Nabla, M., Tejani, A., Chilamkurthy, S., Ai, Q., Steiner, B., ... Chintala, S. (2019). PyTorch: An Imperative Style, High-Performance Deep Learning Library. *Advances in Neural Information Processing Systems* 32, 8024–8035 (cit. on p. 45).
- Pinkard, H. (2019). Deep learning for single-shot autofocus microscopy (cit. on p. 44).
- Pizer, S. M., Amburn, E. P., Austin, J. D., Cromartie, R., Geselowitz, A., Greer, T., ter Haar Romeny, B., Zimmerman, J. B., & Zuiderveld, K. (1987). Adaptive Histogram Equalization and Its Variations. *Computer vision, graphics, and image processing*, 39(3), 355–368. [https://doi.org/10.1016/S0734-189X\(87\)80186-X](https://doi.org/10.1016/S0734-189X(87)80186-X) (cit. on pp. 39, 60)

- Plass, R., Last, J. A., Bartelt, N. C., & Kellogg, G. L. (2001). Self-assembled domain patterns. *Nature*, 412(6850), 875–875. <https://doi.org/10.1038/35091143> (cit. on p. 24)
- Ponce, F. A., Bour, D. P., Young, W. T., Saunders, M., & Steeds, J. W. (1996). Determination of lattice polarity for growth of GaN bulk single crystals and epitaxial layers. *Applied Physics Letters*, 69(3), 337–339. <https://doi.org/10.1063/1.118052> (cit. on p. 97)
- Ponce, F. A., Cherns, D., Young, W. T., & Steeds, J. W. (1996). Characterization of dislocations in GaN by transmission electron diffraction and microscopy techniques. *Applied Physics Letters*, 69(6), 770–772. <https://doi.org/10.1063/1.117886> (cit. on p. 97)
- Pristovsek, M., Tsukamoto, S., Ohtake, A., Koguchi, N., Orr, B. G., Schmidt, W. G., & Bernholc, J. (2003). Gallium-rich reconstructions on GaAs(001). *Physica Status Solidi (B) Basic Research*, 240(1), 91–98. <https://doi.org/10.1002/pssb.200301885> (cit. on pp. 16, 55, 68)
- Ramprasad, R., Batra, R., Pilania, G., Mannodi-Kanakkithodi, A., & Kim, C. (2017). Machine learning in materials informatics: Recent applications and prospects. *npj Computational Materials*, 3(1). <https://doi.org/10.1038/s41524-017-0056-5> (cit. on p. 44)
- Ronneberger, O., Fischer, P., & Brox, T. (2015). U-Net: Convolutional Networks for Biomedical Image Segmentation. *arXiv*. <https://doi.org/arXiv:1505.04597> (cit. on p. 52)
- Ruben, G., Jesson, D. E., Paganin, D. M., & Smith, A. E. (2009). Kinematic simulation of convergent beam low-energy electron diffraction patterns. *Optik*, 120(9), 401–408. <https://doi.org/10.1016/j.ijleo.2007.10.006> (cit. on p. 98)
- Seino, K., Schmidt, W. G., & Ohtake, A. (2006). Ga-rich GaAs(001) surface from ab initio calculations: Atomic structure of the (4x6) and (6x6) reconstructions. *Physical Review B - Condensed Matter and Materials Physics*, 73(3), 4–9. <https://doi.org/10.1103/PhysRevB.73.035317> (cit. on pp. 55, 56, 68)
- Shorten, C., & Khoshgoftaar, T. M. (2019). A survey on Image Data Augmentation for Deep Learning. *Journal of Big Data*, 6(1). <https://doi.org/10.1186/s40537-019-0197-0> (cit. on p. 46)

- Sohl-Dickstein, J., Weiss, E. A., Maheswaranathan, N., & Ganguli, S. (2015). Deep Unsupervised Learning using Nonequilibrium Thermodynamics. *Proceedings of the 32nd International Conference on Machine Learning*. PMLR, 37, 2256–2265. <https://doi.org/arXiv:1503.03585> (cit. on p. 52)
- Spence, J. C., Poon, H. C., & Saldin, D. K. (2004). Convergent-Beam Low Energy Electron Diffraction (CBLEED) and the Measurement of Surface Dipole Layers. *Microscopy and Microanalysis*, 10(1), 128–133. <https://doi.org/10.1017/S1431927604040346> (cit. on pp. 97, 98)
- Stephens, L. I., Payne, N. A., Skaavvik, S. A., Polcari, D., Geissler, M., & Mauzeroll, J. (2019). Evaluating the use of edge detection in extracting feature size from scanning electrochemical microscopy images. *Analytical Chemistry*, 91(6), 3944–3950. <https://doi.org/10.1021/acs.analchem.8b05011> (cit. on p. 71)
- Suzuki, Y., Hino, H., Hawai, T., Saito, K., Kotsugi, M., & Ono, K. (2020). Symmetry prediction and knowledge discovery from X-ray diffraction patterns using an interpretable machine learning approach. *Scientific Reports*, 10(1), 1–11. <https://doi.org/10.1038/s41598-020-77474-4> (cit. on p. 99)
- Swiech, W., Schwarz-Selinger, T., & Cahill, D. G. (2002). Phase coexistence and morphology at the Si(110) surface phase transition. *Surface Science*, 519(1–2). [https://doi.org/10.1016/S0039-6028\(02\)02216-1](https://doi.org/10.1016/S0039-6028(02)02216-1) (cit. on p. 18)
- Takagaki, Y., Jenichen, B., Herrmann, C., Wiebicke, E., Däweritz, L., & Ploog, K. H. (2006). First-order phase transition in MnAs disks on GaAs(001). *Physical Review B*, 73(12). <https://doi.org/10.1103/PhysRevB.73.125324> (cit. on p. 18)
- Tanaka, M., Saito, R., Ueno, K., & Harada, Y. (1980). Large-Angle Convergent-Beam Electron Diffraction. *Journal of Electron Microscopy*, 29(4), 408–412. <https://doi.org/https://doi.org/10.1093/oxfordjournals.jmicro.a050262> (cit. on p. 97)
- Telieps, W., & Bauer, E. (1985). The (7x7) \leftrightarrow (1x1) phase transition on Si(111). *Surface Science*, 162(1–3), 163–168. [https://doi.org/10.1016/0039-6028\(85\)90890-8](https://doi.org/10.1016/0039-6028(85)90890-8) (cit. on p. 54)

- Telieps, W., & Bauer, E. (1986). Kinetics of the $(7\times 7) \leftrightarrow (1\times 1)$ Transition on Si(111). *Berichte der Bunsengesellschaft für physikalische Chemie*, 90, 197–200. <https://doi.org/https://doi.org/10.1002/bbpc.19860900306> (cit. on p. 54)
- Tersoff, J., Jesson, D. E., & Tang, W. X. (2009). Running Droplets of Gallium from Evaporation of Gallium Arsenide. *Science*, 324(5924), 236–238. <https://doi.org/10.1126/science.1169546> (cit. on pp. 57, 82)
- Titterton, D. J., & Kinniburgh, C. G. (1980). Calculation of leed diffracted intensities. *Computer Physics Communications*, 20(2), 237–266. [https://doi.org/https://doi.org/10.1016/0010-4655\(80\)90005-3](https://doi.org/https://doi.org/10.1016/0010-4655(80)90005-3) (cit. on p. 100)
- Tomasi, C., & Manduchi, R. (1998). Bilateral filtering for gray and color images. *Proceedings of the IEEE International Conference on Computer Vision*, 839–846. <https://doi.org/10.1109/iccv.1998.710815> (cit. on p. 60)
- Tromp, R. M. (2000). Low-energy electron microscopy. *IBM Journal of Research and Development*, 44(4), 503–516. <https://doi.org/https://doi.org/10.1147/rd.444.0503> (cit. on p. 31)
- Tromp, R. M. (2019). Measuring chromatic aberration in LEEM/PEEM. *Ultramicroscopy*, 199(December 2018), 46–49. <https://doi.org/10.1016/j.ultramic.2019.01.009> (cit. on p. 34)
- Tromp, R. M., Hannon, J. B., Wan, W., Berghaus, A., & Schaff, O. (2013). A new aberration-corrected, energy-filtered LEEM/PEEM instrument II. Operation and results. *Ultramicroscopy*, 127, 25–39. <https://doi.org/10.1016/j.ultramic.2012.07.016> (cit. on p. 34)
- Tromp, R. M., Mankos, M., Reuter, M. C., Ellis, A. W., & Copel, M. (1998). A new low energy electron microscope. *Surface Review and Letters*, 5(6), 1189–1197. <https://doi.org/10.1142/S0218625X98001523> (cit. on p. 34)
- Tsuda, K., & Tanaka, M. (1999). Refinement of crystal structural parameters using two-dimensional energy-filtered CBED patterns. *Acta Crystallographica Section A: Foundations of Crystallography*, 55(5), 939–954. <https://doi.org/10.1107/S0108767399005401> (cit. on p. 97)
- Tsuno, K., Munro, E., & Rouse, J. (1995). A beam separator of a close packed prism array for low energy electron microscopy. *Nuclear Inst. and Methods*

- in *Physics Research, A*, 363(1-2), 276–283. [https://doi.org/10.1016/0168-9002\(95\)00157-3](https://doi.org/10.1016/0168-9002(95)00157-3) (cit. on p. 31)
- Utimula, K., Yano, M., Kimoto, H., Hongo, K., Nakano, K., & Maezono, R. (2022). Feature Space of XRD Patterns Constructed by an Autoencoder. *Advanced Theory and Simulations*, 2200613. <https://doi.org/10.1002/adts.202200613> (cit. on p. 100)
- van der Walt, S., Schönberger, J. L., Nunez-Iglesias, J., Boulogne, F., Warner, J. D., Yager, N., Gouillart, E., & Yu, T. (2014). scikit-image: image processing in Python. *PeerJ*, 2, e453. <https://doi.org/10.7717/peerj.453> (cit. on pp. 37, 69, 72)
- Van Gastel, R., Bartelt, N. C., Feibelman, P. J., Léonard, F., & Kellogg, G. L. (2004). Relationship between domain-boundary free energy and the temperature dependence of stress-domain patterns of Pb on Cu(111). *Physical Review B - Condensed Matter and Materials Physics*, 70(24), 1–6. <https://doi.org/10.1103/PhysRevB.70.245413> (cit. on p. 71)
- Vanderbilt, D. (1992). Phase segregation and work-function variations on metal surfaces: spontaneous formation of periodic domain structures. *Surface Science*, 268(1-3). [https://doi.org/10.1016/0039-6028\(92\)90939-4](https://doi.org/10.1016/0039-6028(92)90939-4) (cit. on pp. 20, 65)
- Vecsei, P. M., Choo, K., Chang, J., & Neupert, T. (2019). Neural network based classification of crystal symmetries from x-ray diffraction patterns. *Physical Review B*, 99(24), 1–9. <https://doi.org/10.1103/PhysRevB.99.245120> (cit. on p. 99)
- Vincent, R., & Midgley, P. A. (1994). Double conical beam-rocking system for measurement of integrated electron diffraction intensities. *Ultramicroscopy*, 53(3), 271–282. [https://doi.org/10.1016/0304-3991\(94\)90039-6](https://doi.org/10.1016/0304-3991(94)90039-6) (cit. on p. 97)
- Völkl, R., Glatzel, U., & Feller-Kniepmeier, M. (1998). Measurement of the lattice misfit in the single crystal nickel based superalloys CMSX-4, SRR99 and SC16 by convergent beam electron diffraction. *Acta Materialia*, 46(12), 4395–4404. [https://doi.org/10.1016/S1359-6454\(98\)00085-8](https://doi.org/10.1016/S1359-6454(98)00085-8) (cit. on p. 97)
- von Chamier, L., Laine, R. F., Jukkala, J., Spahn, C., Krentzel, D., Nehme, E., Lerche, M., Hernández-Pérez, S., Mattila, P. K., Karinou, E., Holden, S., So-

- lak, A. C., Krull, A., Buchholz, T. O., Jones, M. L., Royer, L. A., Leterrier, C., Shechtman, Y., Jug, F., ... Henriques, R. (2021). Democratising deep learning for microscopy with ZeroCostDL4Mic. *Nature Communications*, 12(1), 1–18. <https://doi.org/10.1038/s41467-021-22518-0> (cit. on p. 44)
- Wang, H., Xie, Y., Li, D., Deng, H., Zhao, Y., Ming, X., & Lin, J. (2018). Rapid Identification of X-ray Diffraction Spectra Based on Very Limited Data by Interpretable Convolutional Neural Networks. *Journal of Materials Processing Technology*, 1(1), 1–8. <https://doi.org/https://doi.org/10.1021/acs.jcim.0c00020> (cit. on p. 99)
- Wu, J., & Jin, P. (2015). *Self-assembly of InAs quantum dots on GaAs(001) by molecular beam epitaxy* (Vol. 10). <https://doi.org/10.1007/s11467-014-0422-4>. (Cit. on p. 81)
- Xing, F., Xie, Y., Su, H., Liu, F., & Yang, L. (2018). Deep Learning in Microscopy Image Analysis: A Survey. *IEEE Transactions on Neural Networks and Learning Systems*, 29(10), 4550–4568. <https://doi.org/10.1109/TNNLS.2017.2766168> (cit. on p. 44)
- Xu, H., Li, Y. G., Wee, A. T., Huan, C. H., & Tok, E. S. (2002). On STM imaging of GaAs(0 0 1)-(nx6) surface reconstructions: Does the (6x6) structure exist. *Surface Science*, 513(2), 249–255. [https://doi.org/10.1016/S0039-6028\(02\)01820-4](https://doi.org/10.1016/S0039-6028(02)01820-4) (cit. on pp. 16, 56)
- Xu, W., & LeBeau, J. M. (2018). A deep convolutional neural network to analyze position averaged convergent beam electron diffraction patterns. *Ultramicroscopy*, 188, 59–69. <https://doi.org/10.1016/j.ultramic.2018.03.004> (cit. on p. 100)
- Yang, S. J., Berndt, M., Ando, D. M., Barch, M., Narayanaswamy, A., Christiansen, E., Hoyer, S., Chris Roat, J. H., Rueden, C. T., Shankar, A., Finkbeiner, S., & Nelson, P. (2018). Assessing microscope image focus quality with deep learning. *BMC Bioinformatics*, 19(4), 77. <https://doi.org/https://doi.org/10.1186/s12859-018-2087-4> (cit. on p. 44)
- Yao, L., Ou, Z., Luo, B., Xu, C., & Chen, Q. (2020). Machine Learning to Reveal Nanoparticle Dynamics from Liquid-Phase TEM Videos. *ACS Central Sci-*

- ence, 6(8), 1421–1430. <https://doi.org/10.1021/acscentsci.0c00430> (cit. on p. 44)
- Yasuda, T., Miyata, N., & Ohtake, A. (2008). Influence of initial surface reconstruction on the interface structure of HfO_2/GaAs . *Applied Surface Science*, 254(23), 7565–7568. <https://doi.org/10.1016/j.apsusc.2008.01.032> (cit. on p. 55)
- Yim, C. M., Man, K. L., Xiao, X., & Altman, M. S. (2008). Low-energy electron microscopy of $\text{CO}/\text{Pt}(111)$ surface diffusion by nonequilibrium coverage profile evolution. *Physical Review B - Condensed Matter and Materials Physics*, 78(15), 1–9. <https://doi.org/10.1103/PhysRevB.78.155439> (cit. on p. 61)
- Yu, K. M., Lau, K. L., & Altman, M. S. (2019). Fourier optics of image formation in aberration-corrected LEEM. *Ultramicroscopy*, 200(December 2018), 160–168. <https://doi.org/10.1016/j.ultramic.2019.01.015> (cit. on p. 34)
- Zandvliet, H. J., Van Gastel, R., Gurlu, O., & Poelsema, B. (2004). Coexistence of (2×1) and $c(4\times 2)$ phases on $\text{Ge}(001)$. *Physical Review B*, 326(5-6), 457–461. <https://doi.org/10.1016/j.physleta.2004.04.056> (cit. on p. 18)
- Zhang, C., Feng, J., DaCosta, L. R., & Voyles, P. M. (2020). Atomic resolution convergent beam electron diffraction analysis using convolutional neural networks. *Ultramicroscopy*, 210(December 2019), 112921. <https://doi.org/10.1016/j.ultramic.2019.112921> (cit. on p. 100)
- Zheng, C. X., Hannikainen, K., Niu, Y. R., Tersoff, J., Gomez, D., Pereiro, J., & Jesson, D. E. (2019). Mapping the surface phase diagram of $\text{GaAs}(001)$ using droplet epitaxy. *Physical Review Materials*, 3(12), 124603. <https://doi.org/10.1103/PhysRevMaterials.3.124603> (cit. on pp. 11, 56, 68, 86, 87)
- Zheng, C. X., Tang, W.-X., & Jesson, D. E. (2016). Planar regions of $\text{GaAs}(001)$ prepared by Ga droplet motion. *Journal of Vacuum Science & Technology A: Vacuum, Surfaces, and Films*, 34(4), 043201. <https://doi.org/10.1116/1.4948530> (cit. on pp. 57, 82)
- Zheng, C. X., Tersoff, J., Tang, W. X., Morreau, A., & Jesson, D. E. (2016). Novel GaAs surface phases via direct control of chemical potential. *Physical Review B*, 93(19), 1–6. <https://doi.org/10.1103/PhysRevB.93.195314> (cit. on pp. 16, 56, 57, 82)

Zuo, J. M., Kim, M., O’Keefe, M., & Spence, J. C. H. (1999). Direct observation of d-orbital holes and Cu-Cu bonding in Cu₂O. *Nature*, *401*, 49–52. <https://doi.org/https://doi.org/10.1038/43403> (cit. on p. 97)